

THE UNIVERSITY OF HULL

Design and synthesis of iron oxide nanomaterials for biomedical applications

Being a Thesis submitted for the Degree of Doctor of Philosophy in the
University of Hull

by

Neazar Eassam Baghdadi

June 2016

Abstract

Nanotechnology products have huge potential to be a part of the developments in various fields, including functional materials, electronics and medicine. Using nanomaterials in medical applications has been successful for disease diagnosis and drug delivery systems. One of the safest and most versatile nanomaterials utilized for medical purposes are iron oxide nanomaterials. This thesis presents the synthesis, coating and targeting vector modification of iron oxide materials for several biomedical applications including multimodal imaging and cancer cell targeting.

Iron oxide nanorods (NRDs) were produced and coated with silica shells as well as other surface modifying molecules including azamacrocycles (DO3A) and polyethylene glycol chains (PEG) which were attached in a one pot reaction. The presence of PEG on the NRDs surface gave improved suspension stability over a wide range of salt concentrations and pH values. Radiolabelling of the NRDs was demonstrated with the positron emitting radioisotope ^{68}Ga . The use of nanorods as magnetic resonance imaging (MRI) contrast agents gave a two-fold increase in T_2 relaxivity (180 s^{-1}) compared to previous work using spherical nanoparticles.

The ^{68}Ga labelled NRD constructs show high radiochemical stability against transferrin challenge over a 3 h incubation period. An *in vivo* bio-distribution study was carried out by intravenously injecting a CD1 nude female mice with 2 mg of (NRDs-PEG), then multimodal imaging analysis was performed using MRI and positron emission tomography (PET) imaging. The NRDs with sizes between 100 to 200 nm showed rapid accumulation in the liver after 5 min due to uptake by macrophages and Kupffer cells as part of reticuloendothelial system, and a small quantity accumulated in the lung and spleen. It was also observed that in the MRI T_2 weighted image, the liver is significantly darker than the T_1 weighted imaging which confirms the sample accumulation. The multimodal images proved that the radiolabelled NRDs were stable *in vivo* on the timescale of the imaging study.

Iron oxide nanoparticles (IONPs) were functionalised for targeting cancer cells. The IONPs were conjugated to a chemokine receptor targeting vector and the targeting properties were tested *in vitro* using Jurkat cancer cells with flow cytometry in an antibody competition assay. The NPs showed 100% inhibition of the anti-CXCR4 antibody binding in this assay.

Risk Assessment and ethical issues

All experiments were carried out in accordance with the University of Hull Health and Safety guidelines. A full COSHH and risk assessment was carried out for each new experiment, signed by the undertaking student, supervisor (Prof S.J. Archibald) and the departmental safety officer (Dr T. McCreedy) before any practical work started. Radiochemistry experiments were assessed using the PET Research Facility Risk Assessment Form, signed by the undertaking student, supervisor (Prof S.J. Archibald) and the radiation protection supervisor (Prof S.J. Archibald) before radiochemical experiments were carried out.

All *in-vivo* procedures were carried out in accordance with the Animals in Scientific Procedures Act 1986 and UKCCCR Guideline 2010[56] by approved protocols following institutional guidelines (Home Office Project License number 60/4549 held by Dr. Cawthorne).

Acknowledgements

First of all, I would like to extend big thanks to both Professor Steve Archibald and Dr Ben Burke for their support and ideas throughout my studies. Without their help, my work would have been much less productive. They helped me in every stage of my PhD work, and also helped me in every difficulty I faced away from the lab work.

To all past and present members of the Archibald group with whom I share the spirit of the team: I have shared the lab emotionally in every working day, experiencing joy, frustration, humour, excitement, anger and delight. I have had a great time, and I consider the time I spent in the Archibald Lab the best time of my life. In no particular order, I thank Mustafa, Ben, Ali, Seraj, Bassim, Juozas, Shubhanchi, Alicia, Hayley, Rachel and Peter. I also would like to thank all those who helped me in the analysis of my samples throughout my PhD stage, namely Carol Kennedy, Kevin Welham, Bob Knight, Ann Lowry, Ben Burke and Shubhanchi Nigam.

Finally, I would like to extend thanks to my parents, who supported me emotionally and personally throughout my PhD study. They have sacrificed their lives for me. Without them, I definitely would not have been able to achieve what I have.

Abbreviations and symbols

3D	Three dimensions
2D	Two dimensions
β^+	Positron (beta plus)
β^-	Electron (beta minus)
β_0	Magnetic field direction
BFC	Bifunctional Chelator
BP	Bisphosphonate
CB	Cross Bridge
CHN	Carbon, Hydrogen, Nitrogen
CT	Computed Tomography
cyclam	1,4,8,11-Tetraazacyclotetradodecane
cyclen	1,4,7,10-Tetraazacyclododecane
DCM	Dichloromethane
DMSA	2, 3-Dimercaptosuccinic Acid
dtc	Dithiocarbamate
DOTA	1,4,7,10-Tetraazacyclododecane 1,4,7,10-tetraacetic acid
DOTP	1,4,7,10-Tetraazacyclododecane 1,4,7,10-tetra(methylenephosphonic acid)
DO3A	1,4,7,10-Tetraazacyclododecane 1,4,7-triacetic acid
DTPA	Diethylenetriaminepentaacetic acid
ELISA	Enzyme-linked immunosorbent assay
DLS	Dynamic Light Scattering
EC	Electron capture
EDTA	Ethylenediaminetetraacetic acid
EDX	Energy-dispersive X-ray spectroscopy
EGFR	Epidermal Growth Factor Receptor
ESI	Electrospray ionization
FDA	Food and Drug Administration
FDG	2-Fluoro-2-deoxy-D-glucose
FT-IR	Fourier transformation infrared
GPCR	G protein-coupled receptor

GPTES	3-glycidyloxypropyl- triethoxysilane
HCC	Hepatocellular Carcinoma Cancer cells
HPLC	High Performance Liquid Chromatography
HRMS	High Resolution Mass Spectrometry
ICP	Inductively Coupled Plasma
ICP-OES	Inductively Coupled Plasma Optical Emission Spectroscopy
IONPs	Iron Oxide Nanoparticles
IONRDs	Iron oxide nanorods
JCPDS	Joint Committee on Powder Diffraction Swarthmore
kBT	Thermal Energy
keV	Kilo electron volt
LOR	Line of response
mAb	Monoclonal antibodies
MFI	Mean fluorescence intensity
MNPs	Magnetic Nanoparticles
MIONPs	Magnetic iron oxide nanoparticles
M_{eq}	Moment recovery to equilibrium state
M_z	Moment decay constant τ_m ,
MRI	Magnetic Resonance Imaging
MS	Mass Spectrometry
NIFR	Near Infrared Fluorescence
NMR	Nuclear Magnetic Resonance
NMV	Net Magnetisation Vector
NOC	Nal3-octreotide
NOTA	1,4,7-Triazacyclononane-1,4,7-triacetic Acid
NPs	Nanoparticles
MNPs	magnetic nanoparticles
NRDs	Nanorods
NTA	Nanoparticle Tracking Analysis
OA	Oleic Acid
PBS	Phosphate Buffered Saline

PEG	Poly Ethylene Glycol
PEI	Polyethylenimine
PET	Positron Emission Tomography
PSPIONs	Poly-dispersed Superparamagnetic Iron Oxide Nanoparticles
PVA	Polyvinyl Alcohol
PVLA	Polyvinylbenzyl-o-beta-D-galactopyranosyl-D-gluconamide
QDs	Quantum Dots
R ₁	Weighted relaxivity T ₁
R ₂	Weighted relaxivity T ₂
RCY	Radiochemical Yield
RES	Reticuloendothelial System
rf	Radio Frequency
RT	Room Temperature
SB	Side Bridge
scFv	Single Chain antibody fragment variable region
SD	Size Distribution
SB-cyclam	Side bridged Cyclam
SM	Saturation magnetization
SPDP	Succinimidyl 3-(2-pyridyldithio) Propionate
SPECT	Single-photon Emission Computerised Tomography
SPIONs	Super Paramagnetic Iron Oxide Nanoparticles
SPM	Superparamagnet
TACN	1,4,7-triazacyclononane
tBu-DO3A	1,4,7-Tris(tert-butoxycarbonylmethyl) 1,4,7,10-tetraazacyclododecane
TE	Echo time
TEA	Triethylamine
TEM	Transmission Electron Microscopy
TEOS	Tetraethylorthosilicate
TFA	Trifluoroacetic Acid
TfR	Transferrin Receptor
THF	Tetrahydrofuran

TLC	Thin Layer Chromatography
TOC	Tyr3-octreotide
TR	Repetition time
TRAP	triazacyclononane phosphinate macrocycle
$T_{1/2}$	Half-life
T_1	Longitudinal or Spin-lattice Relaxation
T_2	Transverse or Spin-spin Relaxation
u-MUC-1	Underglycosylated MUC-1 Tumour Antigen
U_E	Electrophoretic mobility
UV-VIS	Ultra-violet-visible spectroscopy
US	Ultrasound
V	Volt
XRD	X-ray Diffraction
ZP	Zeta-potential
η	Dielectric constant
ω	Larmors frequency

Table of Figures

Figure 1: Magnetic NPs designed for multifunctional purposes.....	5
Figure 2: Spin relaxation, precession and excitation processes.....	7
Figure 3: Single MNP when an external magnetic field applied, showing it acting as a bar magnet.....	9
Figure 4: Showing the decay process of radionuclide to yield positron travel through the body tissues until annihilates to generate two photons with 511keV that are detected by array of scintillation crystal.....	11
Figure 5: Some common cyclen derivatives used for ⁶⁸ Ga complexation for achieving in vivo radiolabelling PET imaging applications.....	14
Figure 6: Some common TACN derivatives used for ⁶⁸ Ga complexation for achieving in vivo radiolabelling PET imaging applications.....	14
Figure 7: Some common acyclic derivatives used for ⁶⁸ Ga complexation for achieving in vivo radiolabelling PET imaging applications.....	15
Figure 8: Enhanced permeability and retention of nanoparticles in tumours.....	16
Figure 9: Solid state structure of Magnetite.....	20
Figure 10: La Mer plot describing synthesis stages for creating of iron oxide nanoparticles from liquid phase into solid phase.....	21
Figure11: NP structures and coating.....	23
Figure 12: TEM image of Fe ₃ O ₄ nanoparticles spherical shape.....	27
Figure13: X-ray diffraction result of iron oxide nanoparticles produced using co-precipitation approach. The peaks are indicating that the sample is inverse spinel magnetite.....	27
Figure14: TEM of NPs synthesised with co-precipitation method with various base addition timing.....	29
Figure15: TEM of NPs synthesised with thermal decomposition method.....	31

Figure16: XRD peaks of iron oxide nanoparticles formed by thermal decomposition method..	31
Figure17: TEM results of synthesised NRDs via co-precipitation method under applying an external magnetic field during base addition step.....	33
Figure18: TEM of co-precipitation synthesised NPs coated with silica layer via direct attachment method.....	36
Figure19: TEM result of NPs coated with silica layer using ligand exchange method....	37
Figure20: Four approaches for radiolabelling NPs.....	41
Figure 21: Various ⁶⁸ Ga chelators used for in vivo applications.....	43
Figure 22 a: Bare NRDs after 24 hours standing.	49
Figure 23 a: Iron concentration test.....	50
Figure24: Elemental analysis of the coated NRDs using ICP-EOS and CHN to determine the percentage of C, H, N, Fe and Si.....	51
Figure 25: FTIR results of coated NRDs with tBuDO3a, NRDs-BuDO3a and PEG 1:1 ratio and NRDs-PEG.....	52
Figure26: TEM images of coated NRDs.....	53
Figure 27: Nanosight (NTA) of coated NRDs to give NRDs size and hydrodynamic size distributions of coated NRDs.....	54
Figure 28 : NRDs surface charges measurements using Zeta potential analysis technique. ...	55
Figure 29: pH (1-11) and salt concentration (1-200 mOsm/L).....	56
Figure 30 A: T1 analysis of 1-3.....	60
Figure 30 B: T2 analysis of 1-3.....	60
Figure 31: Measurement of MRI R2/R1 ratio relaxation for the coated NRDs 1-3.....	61
Figure 32: Testing the ⁶⁸ Ga attachment strength over the coated NRDs against a competitive chelators EDTA for three samples.....	63

Figure 33: Testing the ^{68}Ga attachment strength over the coated NRDs against a competitive transferrin serum solution for three samples.....	64
Figure 34: Bio-distribution study of NRDs coated with Si-PEG using PET imaging technique and the control of gallium-68 transferrin.....	66
Figure 35: Bio-distribution study of NRDs coated with Si-PEG using MRI T ₁ and T ₂ weighted systems imaging technique.....	66
Figure 36: Protonation of nitrogen atom during siloxane of side bridged cyclams.....	78
Figure 37: Positive and negative controls showing CXCR4 expression on the surface of Jurkat cells.....	82
Figure 38: Flow cytometry histogram of negative, positive and NPs based samples for detecting the NPS attachment on cancer cells surface.....	83

Table of schemes

Scheme 1: Organic synthesis of reacting BuDO3a and GPTES by refluxing for 3 days.....	46
Scheme 2: Different ratios of Si-BuDO3a and PEG coating of iron oxide nanorods (NRDs)...	47
Scheme 3: Mechanism of silica shell layer coating iron oxide nanorods using direct attachment method (hydrolysis and condensation reaction mechanisms).....	48
Scheme 4: Reaction of de-protection for BuDO3a over the NRDs surface using TFA.....	49
Scheme 5: Cold radiolabelling reaction using ⁶⁸ Ga in cold status to complex with the DOTA over the surface of NRDs.....	58
Scheme 6: Synthesis steps of siloxane cyclam and metal complexation	75
Scheme 7: Attempted synthesis of siloxane methyl side bridged cyclam (SB) with metals complexation	76
Scheme 8: Synthesis attempted steps of siloxane benzene side bridged cyclam (SB) with metals complexation	77
Scheme 9: Synthesis steps of siloxane cross bridged cyclam (CB) with metals complexation (Cu, Ni and Zn).....	78

Table of tables

Table 1: Summary of common imaging techniques used for medical and research applications..	3
Table 2: Common biomedical applications of nanoparticles.....	3
Table 3: Common non-metallic radionuclides that can be used for PET imaging.....	11
Table 4: Common radionuclides generator systems that provide radionuclides used for PET imaging applications.....	12
Table 5: Common metallic radionuclides generated by cyclotron to be routinely used for PET imaging applications.....	12
Table 6: Brief overview of selected methods for synthesis IONPs.....	21
Table 7: Common materials used for coating of iron oxide nanoparticles for biomedical applications.....	22
Table 8: NTA results with various basic solution addition times.....	29
Table 9: Nanosight (NTA) results of NPs coated and metal complexed with Si-macrocycles..	80
Table 10: Elemental analysis of NPs coated Si-cyclam and Si-CB cyclam.....	80
Table 11: Elemental analysis of metals complexed of coated NPs.....	81

Table of content

1. Introduction.....	1
1.1 Molecular Imaging.....	2
1.2 Nanoparticles materials and biomedical application.....	3
1.3 Magnetic Properties.....	5
1.3.1 Magnetic properties: background.....	5
1.4 Iron in the human body.....	5
1.5 Magnetic resonance imaging (MRI).....	6
1.5.1 MRI principles.....	6
1.5.2 Relaxation Parameters.....	7
1.5.3 MRI contrast agents.....	8
1.5.4 Fundamentals of T ₂ Relaxation in Magnetic Nanoparticles.....	9
1.6 Molecular Imaging using the Nuclear Imaging Modality PET.....	10
1.6.1 Decay, Annihilation, and Coincidence Detection.....	10
1.6.2 PET Radionuclides.....	11
1.6.2.1 ⁶⁴ Cu.....	12
1.6.2.2 ⁶⁸ Ga.....	13
1.6.3 Recent advances in ⁶⁸ Ga chelator design and radiolabelling.....	13
1.6.3.1 Cyclen based chelators.....	13
1.6.3.2 TACN based chelators.....	14
1.6.3.3 Acyclic chelators.....	15
1.7 MRI/PET Multimodal Imaging	15
1.8 SPIONs Targeting and Biodistribution.....	16

1.8.1	Passive Targeting.....	16
1.8.2	Active Targeting.....	17
1.9	Summary of the approach taken in this work.....	17
Chapter 2	Iron Oxide Nanoparticle Synthesis and Coating.....	18
2.1	Background and Aims.....	19
2.2	Introduction.....	20
2.2.1	Solid state structures of iron oxide.....	20
2.2.2	Methods for synthesis of iron oxide nanoparticles.....	21
2.2.3	Materials for coating iron oxide nanoparticles.....	22
2.2.3.1	Methods for coating iron oxide nanoparticles.....	22
2.2.4	Techniques used for characterization of nanoparticles.....	23
2.2.4.1	Transmission electron microscopy.....	23
2.2.4.2	Inductively coupled plasma – optical emission spectroscopy...23	
2.2.4.3	X-Ray Diffraction (XRD).....	24
2.2.4.4	Nanoparticles tracking analysis Nanosight (NTA).....	25
2.3	Synthesis of superparamagnetic iron oxide nanoparticles (SPIONs).....	25
2.3.1	Synthesis of SPIONs via the co-precipitation method.....	25
2.3.1.1	Varying experimental parameters to influence SPION morphology and size distribution.....	27
2.3.2	Synthesis of SPIONs using thermal decomposition method.....	29
2.3.3	Comparison of co-precipitation and thermal decomposition method....	32
2.3.4	Synthesis of iron oxide nanorods (NRDs) using the co-precipitation method.	32
2.4	Silica coating of SPIONs.....	34

2.4.1	SPIONs coated with silica using a direct attachment strategy.....	34
2.4.2	SPIONs coated with silica using a ligand exchange strategy.....	36
2.5.	Conclusion.....	37
Chapter 3: Ga-68 Radiolabelled Iron Oxide nanoparticles for <i>in vivo</i> multimodal imaging.....		
		38
3.1	Aims and background.....	39
3.2	Introduction.....	40
3.2.1	Positron Emission Tomography imaging using radiolabeled iron oxide nanomaterials.....	40
3.2.2	Nanoparticles radiolabelling methodologies.....	40
3.2.3	Nanoparticles and Radiolabelled materials used for Multi-modal (MRI/PET) Imaging.....	41
3.2.4	Gallium-68 isotope for PET imaging.....	42
3.2.5	Gallium chelators.....	42
3.2.6	Radiolabelled NRDs for <i>in vivo</i> bio-distribution studies.....	44
3.2.7	Techniques used for characterization of nanoparticles.....	45
3.2.7.1	Zeta-potential analysis.....	45
3.2.7.2	Other analytical techniques.....	45
3.3	Aims.....	45
3.4	Synthetic Methodology to Form Functionalized DO3A Derivatives.....	46
3.4.1	Chemical synthesis of Si-DO3a.....	46
3.5	NRDs coating and characterizations.....	47
3.5.1	Coating iron oxide nanorods (NRDs) with siloxy functionalized DO3A and PEG derivatives using the direct attachment strategy.....	47

3.5.2	Coated NRDs characterisation.....	49
3.5.2.1	NRDs iron concentration study.....	49
3.5.2.2	NRDs coating efficiency characterizations.....	51
3.5.2.3	NRDs size and size distribution characterization.....	53
3.5.2.4	NRDs stability in suspension.....	55
3.5.2.5	Gallium Complexation for the DO3A coated NRDs.....	57
3.5.2.6	Measuring coated NRDs Magnetic Resonance Imaging (MRI) magnetic properties.....	59
3.6	Coated NRDs constructs suitability for radiolabelling and in vivo tracing multimodality (MRI/PET)	63
3.7	Radiochemistry Reactions and Radiolabelling Stability Studies for Coated NRDs with Gallium-68	63
3.7.1	⁶⁸ Ga radiolabelling procedure for coated NRDs.....	63
3.7.2	Radiolabelling stability tests for coated NRDs	63
3.7.3	<i>In-vivo</i> PET/MRI Biodistribution Study.....	66
3.8	Conclusion.....	68
Chapter 4: Targeting cancer cells using iron oxide nanoparticles attached to CXCR4 antagonists.....		
4.1	Aims and background.....	70
4.2	Introduction.....	70
4.2.1	Vectors for identifying and targeting cancers.....	71
4.2.2	Nanoparticles targeting cancer cells.....	71
4.2.3	Chemokines & Chemokine Receptors.....	72
4.2.3.1	Chemokines.....	72

4.2.3.2	Chemokines receptors.....	72
4.2.3.3	CXCR4/CXCL12.....	73
4.2.3.4	CXCR4 Antagonists.....	73
4.2.4	Technique used for characterizing NPs cancer cell targeting propertie.....	74
4.2.4.1	Flow cytometry.....	73
4.3.	Synthesis of siloxane functionalized macrocyclic (CXCR4 Antagonists).....	74
4.3.1	Synthesis of the siloxane derivative of cyclam and metal complex formation..	75
4.3.2.	Siloxane derivative of side bridged cyclam and metal ion complex formation....	76
4.3.3.	Siloxane derivative of the benzyl side bridged cyclam and attempted metal ion complex (copper(II), nickel(II) and zinc(II)).....	78
4.3.4	Siloxane derivative of cross bridged cyclam and metals complex formation....	79
4.4	IONPs Coating with Siloxane Macrocycles using Ligand Exchange Method.....	80
4.5	Biological Studies of Chemokine Receptor Binding in vitro.....	82
4.6	Conclusion.....	85
Chapter 5:	Conclusion.....	86
5.1	Overall approach and key achievements.....	87
5.2	Synthetic methods to produce and coat iron oxide nanoparticles.....	87
5.3	Radiolabelling of nanoparticles with gallium-68.....	88
5.4	Conjugation of targeting materials.....	89
5.2	Future Directions.....	90
Chapter 6:	Experimental.....	91
6.1	Materials.....	92
6.2	Instrumentations.....	92
6.2.1	Optical Emission ICPMS.....	92

6.2.2	TEM.....	92
6.2.3	XRD.....	92
6.2.4	Ultrasonicator.....	92
6.2.5	Nanosight Nanoparticle Tracking Analysis (NTA).....	93
6.2.6	FTIR.....	93
6.2.7	CHN.....	93
6.2.8	Zeta Potential.....	93
6.2.9	NMR.....	93
6.2.10	Mass Spectrometry.....	93
6.2.11	Flow Cytometry.....	93
6.2.12	MRI.....	93
6.2.13	UV-vis Spectra.....	94
6.2.14	Fluorescence Spectroscopy.....	94
6.3	Synthesis and Coating of Iron Oxide Nanoparticles.....	95
6.3.1	Synthesis of iron oxide nanoparticles using co-Precipitation, compound 1	95
6.3.2	A general method for synthesis of NPs with various sizes using drop-wise addition timing approach.....	96
6.3.2.1	Controlling the NPs size via timing the drop-wise base addition using Co-precipitation method, compounds 2.....	96
6.3.2.2	Controlling the NPs size via timing the drop-wise base addition using Co-precipitation method: Compounds 3.....	96
6.3.2.3	Controlling the NPs size via timing the drop-wise base addition using Co-precipitation method: Compounds 4.....	96
6.3.3	Synthesis of iron oxide nanoparticles using thermal decomposition method: Compound 5.....	97

6.3.4 Synthesis of iron oxide nanorods (NRDs) via co-precipitation method, compound 6.....	98
6.3.5 Iron oxide nanoparticles coated with silica layer by direct silica attachment, compound 7.....	99
6.3.6 Iron oxide nanoparticles coated with silica layer via ligand exchange method, compound 8.....	100
6.3.7 Synthesis of tri-tert-butyl 2, 2, 2-(10-(2-hydroxy-3-(3-(triethoxysilyl) propoxy) propyl)-1, 4, 7, 10-tetraazacyclododecane-1, 4, 7, triyl)triacetate, compound 10.....	101
6.3.8 Synthesis of tri-tert-butyl 2, 2', 2''-(10-(2-hydroxy-3-(3- (triethoxysilyl)propoxy) propyl)-1-, 4-, 7-, 10-tetraazacyclododecane-1-, 4-, 7-triyl)triacetate Functionalised Magnetite Nanorods, compound 11.....	102
6.3.9 Synthesis of 2, 2', 2''-(10-(3-(3-(dihydroxysilyl)propoxy)-2-hydroxypropyl)-1-, 4-, 7-, 10- Tetraazacyclododecane-1-, 4-, 7-triyl)triacetic acid functionalised magnetite nanorods, compound 12.....	103
6.3.10 NPs coated with mixture of Si-BuDO3A and Si-PEG 1:1 ratio via direct attachment method, compound 13.....	104
6.3.11 De-protection of NRDs coated with mixture of Si-BuDO3A and Si-PEG 1:1 ratio, compound 14.....	105
6.3.12 NPs coated with of Si-PEG via direct attachment method, compound 15...106	
6.3.13 Synthesis of ⁶⁹ Ga complex of 2, 2, 2-(10-(3-(3-(dihydroxysilyl)propoxy)-2-hydroxypropyl)-1, 4, 7, 10-tetraazacyclododecane-1, 4, 7-triyl) triacetic acid coating NRDs, compound 16.....	107
6.3.14 Synthesis of (3-glycidyloxypropyl)triethoxysilane functionalised magnetite nanoparticles, compound 17.....	108

6.3.15	Iron concentration stability test of 2-, 2'-, 2''-(10-(3-(3-(dihydroxysilyl)propoxy)-2-hydroxypropyl)-1-, 4-, 7-, 10-Tetraazacyclododecane-1-, 4-, 7-triyl) triacetic acid functionalised magnetite nanorods (NRDs).....	109
6.3.16	Studying the effects of PEG addition on NRDs stability with range of pHs.	110
6.3.17	Studying the effect of PEG addition on NRDs stability with range of salt concentrations.....	111
6.3.18	Synthesis of ⁶⁸ Ga complexes NRDs coated BuDO3A, compound 18.....	112
6.3.19.	Synthesis of ⁶⁸ Ga complex of NRDs coated with Si-BuDO3A and Si-PEG 1:1 ratio, compound 19.....	112
6.3.20	Complexation of gallium(III) with NRDs coated with Si-PEG 1:1 ratio, compound 20.....	113
6.3.21	EDTA stability of Ga complex of 2-, 2'-, 2''-(10-(3-(3-(dihydroxysilyl)propoxy)-2- hydroxypropyl)- 1-, 4-, 7-, 10-tetraazacyclododecane-1-, 4-, 7-triyl)triacetic acid functionalised magnetite nanorods (NRDs).....	113
6.3.22	EDTA stability of ⁶⁸ Ga complexed NRDs coated with Si- BuDO3A and Si-PEG 1:1 ratio	114
6.3.23	EDTA stability of ⁶⁸ Ga complexed NRDs coated with Si-PEG	114
6.3.24	Synthesis of macrocyclic ligands, synthesis of cyclam, compound 21.....	115
6.3.25	Synthesis of sailoxane ligand on cyclam, compound 22.....	116
6.3.26	Synthesis of Cis-3a, 5a, 8a, 10a-tetraazaperhydropyrene (Bridged Cyclam), compound 26	117
6.3.27	Synthesis of 3a-[methyl]-decahydro-3a,5a,8a,10a-tetraaza-pyrenium iodide, compound 27.....	117
6.3.28	Synthesis of 5-(methyl)-1-, 5,8,12-tetraaza-bicyclo[10.2.2] hexadecane, compound 28.....	118

6.3.29	Attempted synthesis of siloxane ligand on methyl side bridged cyclam, compound 29	119
6.3.30	Synthesis of 3a-benzyl-decahydro-3a,5a,8a,10a-tetraazapyrenium Bromide, compound 33.....	119
6.3.31	Synthesis of 4-benzyl-1-, 4-, 8-, 11-tetraazabicyclo[10.2.2]hexadecane, compound 34	120
6.3.32	Attempted synthesis of siloxane ligand on benzyl side bridged cyclam, compound 35.....	120
6.3.33	Synthesis of (10ba,10ca)-Decahydro-3a,8a-bis(phenylmethyl)-1H,6H-3a,5a,-8a,10a-tetraazapyrenium Dibromide Monohydrate(3a.h2o), compound 39.....	121
6.3.34	Synthesis of 4,11-Dibenzyl-1-, 4-, 8-, 11-tetraazabicyclo[6.6.2]hexadecane, compound 40a.....	121
6.3.35	Synthesis of 1-, 4-, 8-, 11-tetraazabicyclo[6.6.2]hexadecane, compound 40b.....	122
6.3.36	Synthesis of siloxane ligand on cross-bridged cyclam, compound 41.....	122
6.3.37	Synthesis of Transition Metal Complexes	123
6.3.37.1	Synthesis of $[\text{CH}_3\text{CO}_2]_2\text{Zn}$ siloxane cyclam, compound 23.....	123
6.3.37.2	Synthesis of $(\text{Cu}_2 (\text{OAc})_2)$ for siloxane cyclam, compound 25.....	124
6.3.37.3	Synthesis of $(\text{Ni}(\text{CH}_3\text{COO})_2)$ for Siloxane Cyclam compound 24...	124
6.3.37.4	Synthesis of $(\text{Cu}_2 (\text{OAc})_2)$ for cross-bridged siloxane cyclam, compound 44.....	125
6.3.37.5	Synthesis of $(\text{CH}_3\text{CO}_2)_2\text{Zn}$ cross-bridged siloxane cyclam, compound 42.....	125
6.3.37.6	Synthesis of $(\text{Ni}(\text{CH}_3\text{COO})_2)$ for cross-bridged siloxane cyclam, compound 43.....	126
6.3.38.	Reacting NPs with siloxane macrocycles	126
6.3.38.1.	NPs siloxane cyclam: compound 45.....	126

6.3.38.2. NPs cross-bridged siloxane cyclam compound 46.....	127
6.3.39. Metals Complexation NPs	128
6.3.39.1 Complexing nickel acetate to NPs-siloxane cyclam, compound 48....	128
6.3.39.2 Complexing copper acetate to NPs-cross-bridged cyclam-siloxane, compound 50.....	129
6.3.39.3. Complexing copper acetate to NPs-siloxane cyclam, compound 47.....	129
6.3.39.4 Complexing zinc acetate to NPs-cross-bridged cyclam-siloxane, compound 52.....	129
6.3.39.5 Complexing nickel acetate to NPs-cross-bridged cyclam-siloxane, compound 51.....	130
6.3.39.6 Complexing zinc acetate to NPs-cyclam-siloxane, compound 49.....	131
6.3.39.7 Bare nanoparticles complexed with copper acetate, compound 53.....	131
6.3.39.8 Bare nanoparticles complexed with nickel acetate, compound 54.....	132
6.3.39.9 Bare nanoparticles complexed with zinc acetate, compound 55.....	132
Appendix.....	133
Figure A1 TEM for compound 1.....	133
Figures A2 TEM for compounds 2, 3 and 4.....	133
Figure A3 TEM for compound 5.....	133
Figure A4 TEM for compound 6.....	134
Figure A5 TEM for compound 7.....	134
Figure A6 TEM for compound 8.....	134

Figure A7 TEM for compound 12.....	135
Figure A8 TEM for compound 14.....	135
Figure A9 TEM for compound 15.....	135
Figure A10 TEM for compound 16.....	136
Figure B1 NTA for compound 1.....	136
Figure B2 NTA for compound 2.....	136
Figure B3 NTA for compound 3.....	137
Figure B4 NTA for compound 4.....	137
Figure B5 NTA for compound 5.....	137
Figure B6 NTA for compound 6.....	138
Figure B7 NTA for compound 7.....	138
Figure B8 NTA for compound 8.....	138
Figure B9 NTA for compound 12.....	139
Figure B10 NTA for compound 14.....	139
Figure B11 NTA for compound 15.....	139
Figure B12 NTA for compound 16.....	140
Figure B13 NTA for compound 17.....	140
Figure B14 NTA for compound 45.....	140
Figure B15 NTA for compound 46.....	141
Figure B16 NTA for compound 48.....	141
Figure B17 NTA for compound 50.....	141
Figure B18 NTA for compound 47.....	142
Figure B19 NTA for compound 52.....	142

Figure B20 NTA for compound 51.....	143
Figure B21 NTA for compound 49.....	143
References.....	144

Chapter 1

Introduction

1.1 Molecular Imaging

The last decade has shown major advances in our knowledge and understanding of disease at a molecular level. These developments offer important information for determining the progression and the cause of common diseases such as cancer.

At present, with newly developed *in vitro* techniques, biologists are able to evaluate the action of unbalanced gene expression that can cause specific disease pathology states. The field of molecular imaging has emerged with the aim to move towards *in vivo* imaging of molecular interactions. Cancer cells could not only be detected but their development evaluated and disease progression determined at a molecular level without performing a surgically invasive process.¹

The majority of currently available *in vivo* diagnostic techniques are limited to the assessment of the structure and function of human organs. Accordingly, an important disease such as cancer is generally only detected at a relatively advanced stage. However, the advances in understanding of cellular processes in the last decade provide us with valuable knowledge about cancer biology, which in turn increases the potential for producing a new generation of diagnostic imaging agents for detecting cancer cells based on specific molecular processes *in vivo* making early stage detection possible and also selection of the most appropriate treatment. In this regard, chemistry plays a crucial role in such revolutionary systems. By exploiting chemical knowledge and the tools of conjugation chemistry, materials chemistry, coordination chemistry and synthetic organic chemistry, it is possible to overcome many of the barriers to molecular imaging.²

Generally, an imaging probe is designed for a particular purpose which is partly dictated by the physical aspect of the imaging modality (MRI, PET, SPECT, CTetc) which relies on the localisation and concentration of the contrast agent or radiopharmaceutical at the disease site. For example, MRI imaging depends on the magnetic properties of the protons in the body, using a probe with specific magnetic properties that localises at the site of interest can improve the contrast at that site.

For efficient imaging, high affinity compounds which have been produced by conjugation to a targeting vector have been studied. A number of proteins and biochemical mechanisms could be targeted and detection on the surface of cancer cells offers an easier method of targeting as it is not dependent on internalization, see Table 1.³

Some targets that have been of interest include:

1. Markers associated with variations in the extracellular matrix.
2. Membrane receptors involved in cellular signaling processes.
3. Markers of apoptosis.

Chemical and biological factors that should be optimised in order to improve targeting efficiency and image quality include; bio-distribution, toxicity, excretion path ways, utilising multivalent binding, intravascular half-life, the capability for incorporation of diverse imaging probes and the capacity for high contrast.³

Imaging technology	Portion of EM radiation spectrum used in image generation	Advantages	Disadvantages
Positron emission tomography (PET)	High energy γ ray	High sensitivity, quantitative	Cyclotron or generator needed, low spatial resolution, patient radiation exposure.
Single photon emission computed tomography (SPECT)	Low energy γ ray	Many molecular probes available	Low spatial resolution, patient radiation exposure, collimator required.
Optical Bioluminescence imaging	Visible light	Highest sensitivity, quick, easy, low cost,	Low spatial resolution, 2D images only, only useful in cell or tissue samples
Optical fluorescence imaging	Visible light or near infrared	Highest sensitivity, fluorochrome detectors for living cells	Low spatial resolution, surface weighted, poor tissue penetration
Magnetic resonance imaging (MRI)	Radio waves	Highest spatial resolution, combines morphology and functional imaging	Low sensitivity, long scan time, high mass quantity of probe required.
Computed tomography (CT)	X-rays	Bone and tumour imaging, anatomical imaging	Limited soft tissue resolution, radiation.
Ultrasound	High frequency sounds	Real-time, low cost.	Mostly morphological, limited spatial resolution.

Table 1: Summary of common imaging techniques used for medical and research applications. Some data is taken from a published article.³

1.2 Nanoparticles materials and biomedical application

Nanotechnology is an emerging field contributing to many areas in science and technology such as manufacturing, medicine, materials, electronics, mechanics, chemistry, physics and many others. In medicine, nanotechnology exploits the nanoparticle's size and shape which offer unique properties and can be applied to molecular imaging especially in cancer imaging applications.

There are many other biomedical applications that the NPs can be involved with future translation possible to the clinic play a significant role to change the future clinic phase. A summary of some applications under extensive research is presented in Table 2.

Applications	Selected references
MRI contrast agent enhancement	4
Targeted drug delivery	5
Magnetic hyperthermia	6
Cell labelling/ cell tracking	7

Table 2: Common biomedical applications of nanoparticles.⁸

There are many forms of nanoparticles used for biomedical applications, for example, liposomes have proven to function well as drug delivery systems.⁹ NPs that possess the ability to have tightly controlled size can be very important, for example in tuning the optical properties of quantum dots (QDs) and also influencing the biodistribution.¹⁰ NPs composed of magnetic materials can be used to provide excellent MRI relaxivity as contrast agents.⁴ All nanoparticle forms have the feature of a high surface area. For instance, 1 gram of iron oxide with a particle size of 0.75 μm diameter and a spherical shape has a surface area of around 1.77 cm^2 whereas with the same amount of material, if the particles size is reduced to 20 nm diameter, then the surface area becomes around 60 m^2 . In addition, there is the possibility of modifying the NPs surface with various chemical functional groups allowing the NPs to be conjugated with imaging agents, drug molecules, targeting ligands and nucleic acids. The engineered NPs could offer multivalent targeting by the conjugation of several ligands onto the surface in close proximity in order to increase ligand binding affinity (which in turns leads to an increase in imaging signal output). Also, the high surface area provided by NPs allowing multifunctional applications, for example, single NPs carrying drug molecules, targeting ligands and imaging agents simultaneously, see Figure 1.

Magnetic iron oxide nanoparticle (MIONP) contrast agents have been used for clinical medical imaging purposes for many years. MIONPs have been also been used widely in research studies for investigating a range of biological mechanisms such as monitoring atherosclerosis, cancer detection and stem cell tracking.^{11, 12}

There is great potential for magnetic nanoparticles (MNPs) to become the most effective nanomaterial in biomedical applications since their size is very close or comparable to those of proteins (5-60 nm) and genetic material (10-100 nm) which offers the opportunity to interact efficiently with these biological targets. Secondly, MNPs have the ability to respond to an external magnetic field which provides the potential for transfer of the MNPs energy to an excited state which could then be used to heat up and deliver toxic thermal energy to tumours (hyperthermia), alternatively, they can be modified for use as chemotherapy or radiotherapy agents. Thirdly, the MNPs obey Coulomb's law which means that MNPs can be manipulated externally by applying a magnetic field inside the body. This could allow direction of attached radionuclide atoms or anticancer drugs to a specific area in the body, see Figure 1.

In order to design MNPs for the above biomedical applications, the synthesised MNPs must have a size less than 100nm, have high magnetisation values and have a very narrow size distribution. Also the MNPs must be coated with a biocompatible, non-toxic material, have high stability in different biological conditions and be functionalised with appropriate terminal groups for further applications.¹³

Using iron oxide nanoparticles as a contrast agent offers good potential for the development of diagnostic and therapeutic methodology in future biomedical applications, especially in cancer diagnosis and treatment. Other magnetic materials such as cobalt and nickel solid state materials have toxicity limiting their usage in medical applications, and iron oxide compounds have a good safety record as they are already approved by FDA to be used for biomedical applications with products such as Ferumoxsil and NanoTherm.

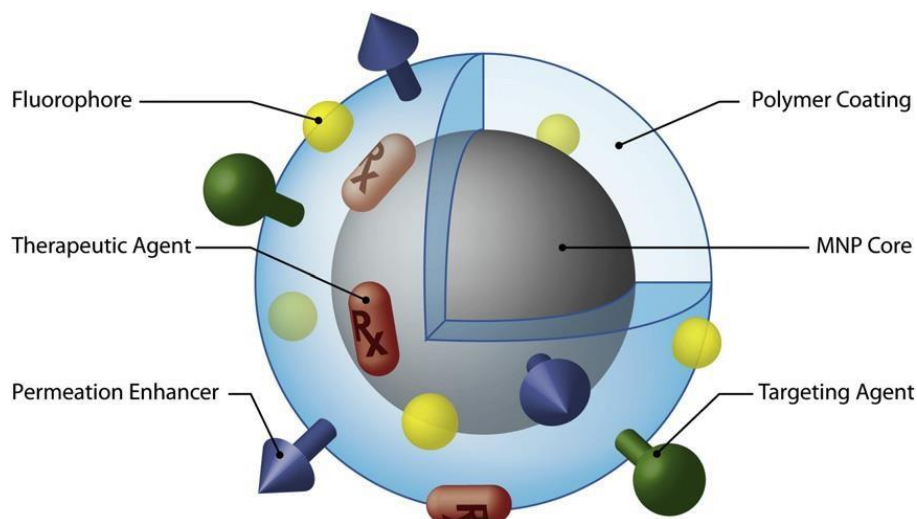


Figure 1: Magnetic NPs designed for multifunctional purposes. This Figure is reproduced from Sun et al.¹³

1.3 Magnetic Properties

The magnetic properties of iron oxide nanoparticles are dictated by number of factors including microstructure, chemical phases, composition, shape and size.

1.3.1 Magnetic properties: background

The type of magnetism is dependent on the material's atomic composition and solid state structural arrangement. Paramagnetic ions such as iron(II)/(III) possess unpaired electrons in their electronic configuration,¹⁴ and under an external magnetic field, they are free to align in parallel or antiparallel to the magnetic field direction. If the applied magnetic field is removed, the electrons spin align randomly under the effect of thermal motion, the net magnetic dipole moment becomes zero.¹⁴

Superparamagnetic behaviour can arise in ferromagnetic materials such as magnetite (Fe_3O_4) and maghemite (Fe_2O_3) when the particle size is reduced to a point where thermal energy has a significant effect, causing randomized dipole moments with no magnetisation stored in the material's sub-lattice. When the iron oxide compounds are exposed to an external magnetic field, the magnetic domains align in parallel to the field and the compounds become magnetised. Hence, when the particle size is reduced to the nano range, the iron oxide may become superparamagnetic. The traditional synthesis methods to produce iron oxide nanoparticles provide particles with a roughly spherical shape and polydisperse size distribution. However, there are synthesis methods for generating monodisperse spherical IONPs, nanorods, nanocubes and octahedral IONPs.¹⁴

1.4 Iron in the human body

The iron in the human body is regulated by complex mechanisms. In the body, 20 mg of iron is needed daily for proteins such as hemoglobin. The iron (ferrous ions) absorption mechanism happens in two steps; the ferrous ions are absorbed by intestinal lumen into the mucosal cells which carry the iron to the plasma where the iron is bound to the protein

transferrin and can be transferred for storage in the liver. The ferrous ions can be oxidized by oxygen in the presence of ferroxidase I. The total amount of iron in the human body is around 3 to 5 g and most of it is bound to haemoglobin with around 10% bound to myoglobin and the rest bound to the iron storage proteins hemosiderin and ferritin. When the iron is needed, it is released by a reduction process utilizing reducing agents such as glutathione, ascorbic acid and cysteine and the excess ingested iron is usually excreted with a total iron excretion of around 0.5 mg/day. Further iron exposure or overload leads to an increase in ferritin synthesis in the hepatic parenchymal cells. There can be a switch in the ratio of ferritin to haemosiderin synthesis under iron overload conditions.¹⁵

1.5 Magnetic resonance imaging (MRI)

Among different imaging techniques, MRI can provide three dimensional images of the internal tissues and organs non-invasively, without radioactive materials, to provide high resolution anatomical information.¹⁶

1.5.1 MRI principles

The interaction between a nucleus that has an unpaired electron and the externally applied magnetic field, causes the nuclear spin to align with the magnetic field direction. The ^1H isotope has a single proton with spin $I=1/2$ for the 100% abundant isotope. This nucleus strongly responds to the applied magnetic field. The human body is mainly constructed from water and fat which have hydrogen content. This property is the foundation of clinical MRI.¹⁷

When no external magnetic field is applied, the protons are randomly organised with equal magnetisation in all directions. Once an external magnetic field is applied, the protons are aligned either in parallel or anti-parallel to the magnetic field direction dependent on the proton energy. When the protons align, a slight excess of nuclei align parallel to the external magnetic field leading to positive net magnetisation. Therefore, a higher applied magnetic field leads to improved imaging signals.

With the applied magnetic field, the protons start to rotate and precess along with the magnetic field, and the precession starts to deviate away from the main magnetic field axis (Z direction). The precession frequency is proportional to the applied magnetic field strength, see Figure 2. A radio frequency (rf) pulse is applied to resonate the protons in order to move the net magnetisation vector (NMV) away from the applied magnetic field direction at a 90° angle causing the protons alignment to move from the longitudinal plane towards the transverse plane. Once the (rf) pulse is switched off, the protons start to align back randomly to the equilibrium orientation producing energy with a specific frequency which can be detected via a coil receiver. During this process, the energy is lost via relaxation and there are two relaxation times for MRI images; T_1 and T_2 .¹⁸

Under an external magnetic field B applied along the Z axis, the magnetisation of nuclear spin vector M recovers to its equilibrium state M_{eq} and the decay constant time M_z (the time consumed to align the spin parallel of M) is defined as T_1 and expressed as the energy for the relocation from the proton to the surrounding lattice and is known as the spin-

lattice or longitudinal relaxation time. T_2 is the decay constant of M_{xy} and is expressed as the time taken for the spin to dephase due to magnetic field inhomogeneities (which can be influenced by iron oxide nanoparticles). T_2 relaxation is known as spin-spin or transverse relaxation time. T_1 is defined as the length of time for the signal to recover around 63% from the maximum point whereas T_2 is the time taken for the signal to recover to around 37% from the initial point.

MRI provides good soft tissue contrast and up to sub-millimetre spatial resolution in some cases, while avoiding patient exposure to ionizing radiation. Its anatomical imaging applications include cardiac imaging, neuroimaging and musculoskeletal imaging. There are also a myriad of cancer imaging applications with about 40% of MR clinical images using contrast agents.¹⁸

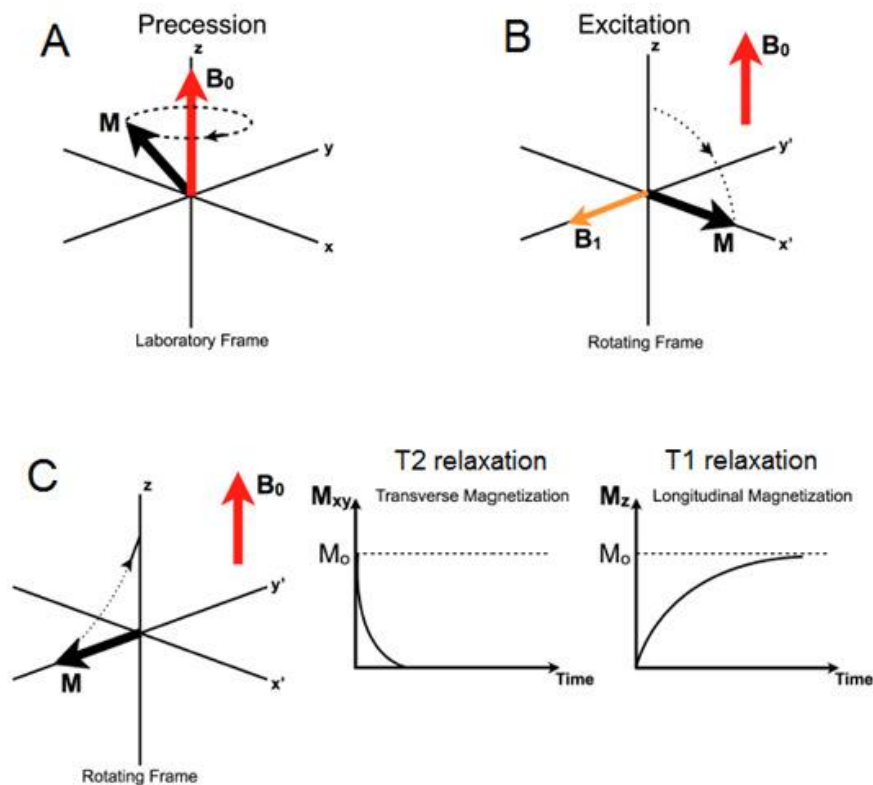


Figure 2: Spin relaxation, precession and excitation processes. (A): describes the process of protons aligning toward z-axis at the Larmor frequency (B): RF pulse is applied in order to excite the tissues slice in the traverse plane. Two relaxation parameters are produced, T_1 and T_2 . (This Figure is reproduced from a PhD thesis from Stanford University, PJ Beatty, Reconstruction Methods for Fast Magnetic Resonance Imaging.)

1.5.2 Relaxation Parameters

The relationship between the MRI sequence parameters, echo time (TE), repetition time (TR) and relaxation parameters (T_1 and T_2) influence the magnitude of the signal produced by the proton nuclei under the MRI magnetic field. Echo time (TE) is a measurement of the time between excitation and the start of signal acquisition. Repetition time (TR) is a measurement of the interval between excitations.

If T_2 weighted imaging is used, TR is far longer than T_1 and TE is set as long as T_2 in order to reduce the effect of T_1 and also to express the differences in T_2 decay. If T_1 weighted imaging is used, TR is set to be much shorter than T_1 and TE is also short in order to prevent

longitudinal magnetization recovery before the following repetition sequence and to prevent T₂ contrast. Proton density weighted imaging is produced by setting long TR and short TE sequences.

1.5.3 MRI contrast agents

The contrast agents for MRI are used to provide a clear contrast to structures of tissues that are otherwise difficult to visualize. There are two classifications of contrast agents for MRI, one designed for T₁ weighted imaging and the other designed for T₂ weighted imaging. Both of these types of agents change the MR signal but they have different physical mechanisms of action. For T₁ contrast agents, the most common are gadolinium based contrast agents. The contrast performance is based on a property of gadolinium(III), which possesses seven unpaired electrons that lead to a strong paramagnetic effect in the site of location. The mechanism by which gadolinium induced contrast works is to provide small magnetic field inhomogeneities that cause a reduction effect in the T₁ and T₂ relaxation times of the protons (generally water protons) around the gadolinium. The typical clinically used gadolinium ion concentration is around 0.1 mM which can cause a significant decrease in T₁ relaxation and a bright image is revealed at the site of gadolinium uptake. If the gadolinium concentration is further increased, the T₂ relaxation may become dominant and interferes with the T₁ relaxation which is not desirable. Gadolinium ions are toxic in their free aqueous bound form, therefore they must be chelated to a ligand to form a stable complex. Chelate ligands such as diethylenetriaminepentaacetic acid (DTPA) can be used to complex the gadolinium in order to decrease the biological toxicity.¹⁹

The other contrast agent group based on T₂ relaxation generally uses iron oxide nanoparticles. IONPs mainly cause a reduction in T₂ relaxation time, therefore, they are considered as negative contrast agents. Superparamagnetic iron oxide nanoparticles (SPION) contrast agents have been used in clinical imaging for more than two decades. They are distinguished from the gadolinium agents by their superparamagnetic properties (containing areas of unpaired spins whilst acting as single domain particles). If an external magnetic field is applied, the magnetic domains align parallel to the B₀ which has a significant effect on T₂ relaxation.

The SPION contrast agents can be designed to provide a variety of different physico-chemical properties, dependent on the surface of the particles, which can be influenced using a number of techniques such as the coating material, surface charges, particle size and size distribution. These factors will also effect the SPIONs *in vivo* pharmacokinetics. SPION contrast agent relaxivity values, R₁ and R₂, are calculated from the slope of 1/T₁ and 1/T₂ versus iron concentrations. Many factors have an effect on the relaxivity of the SPIONs such as the synthesis route, crystallinity and solid state structure, average particle size and the SPIONs surface coating type and thickness. The coating material, structure and thickness generally have a direct effect on how the surrounding water molecules can interact with the magnetic field formed by the SPION core.²⁰

1.5.4 Fundamentals of T₂ Relaxation in Magnetic Nanoparticles

Concentration of superparamagnetic iron oxide nanoparticles in the area of interest should result in a significant increase in image contrast. T₂ weighted imaging pulse sequences are used to detect the magnetic nanoparticle accumulation. Since the nanoparticles have superparamagnetic behaviour, a local magnetic field is created around them when an external magnetic field is applied. This local field (gradient) means that each nanoparticle is acting as an individual bar magnet (see Figure 3). Therefore, the resultant spin oscillation of the water protons will be changed due to two participating factors; the effect of the applied magnetic field on the water proton, and the local field that is generated by aggregation of the nanoparticles. This reduces the decay time by generating two different spins and frequencies around each nanoparticle, one from spins near the particles (r₁), and the other generated from spins far away from the particle r₂, corresponding to ω_1 and ω_2 , respectively.²¹

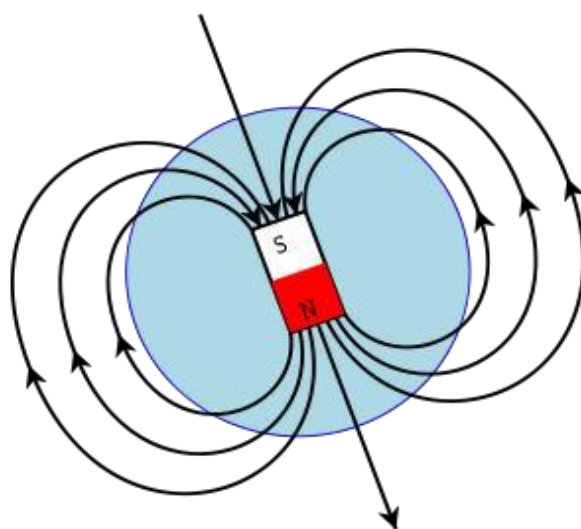


Figure 3: Single MNP when an external magnetic field applied, showing it acting as a bar magnet. This Figure is reproduced from Truffault et al.²¹

As the water molecules diffuse onto the nanoparticle surface, the spin and frequency at r₁ and ω_1 can shift to r₂ and ω_2 during signal acquisition. This type of shifting in frequency causes a loss in spin coherence. Because the spins are diffusing quickly all the time, the loss of spin coherence is significantly increased, which is called spin dephasing.²¹

For MRI contrast agent, SPIONs have several features that differ in comparison to the molecular gadolinium agents. For example, SPIONs can circulate in the body for a longer time due to the nano-size, as the immune system does not generally target small size particles less than 100 nm in diameter and they are not renally excreted. SPIONs provide high sensitivity and low toxicity. SPIONs offer a high surface area which allows various components to be incorporated on the surface to allow radiolabelling, improve sensitivity, target the nanoparticles and introduce potential therapeutic components. Radiolabelling of iron oxide nanoparticles has only recently been exploited to form compounds for multimodal imaging and further research is ongoing in this area. Exciting results are hypothesized for future biomedical applications especially in oncology for diagnosis and therapy.^{22, 23}

1.6 Molecular Imaging using the nuclear imaging modality PET

In molecular imaging, positron or gamma emitting radionuclides are used as components of radiopharmaceuticals. Radiopharmaceuticals can be used *in vivo* to show biodistribution or to characterise disease. Radiopharmaceuticals for targeting specific physiological and biochemical processes are of high interest. Positron emission tomography (PET) is a nuclear imaging technique providing highly quantitative and sensitive imaging data that can be used to measure the localisation and biodistribution of the radionuclide *in vivo* against time.²⁴

PET radionuclides have useful properties for investigating heart and brain functions and most notably for cancer detection by determining the cancer location and distribution. The mechanisms that the radiolabeled compounds exploit are based on targeting specific conditions or physiological processes that appear as a result of malignancy such as receptor expression, cell proliferation, glucose metabolism and bone deposition.²⁴ PET has higher sensitivity but lower resolution than MRI, however it only detects the agent rather than the background physiology. It is a ‘true’ molecular imaging technique and is highly complementary to MRI. Hence, a new generation of PET/MRI scanners have been designed and are moving into clinical use.

1.6.1 Decay, Annihilation, and Coincidence Detection

Once the radionuclide has been injected inside the body, radioactive decay occurs to give a signal. Positrons are emitted which have a kinetic energy determined by the radionuclide administered. The positrons travel a short distance away from the radionuclide location losing kinetic energy until most of the energy is lost and then they annihilate with an electron producing two 511 keV gamma rays emitted at 180° apart from each other, see Figure 4. The distance that the positron travels from the decay location to annihilation is a disadvantage as it affects the spatial resolution. During the photon detection process, the PET scanner is all around the patient to accurately pinpoint the positions of the emitted gamma rays and to pair them up. The detected information is used to form a 3-D tomographic image. The biggest advantage of PET is ability to provide highly sensitive deep tissue images and it is the best technique to produce quantitative data. In addition, the required radionuclide concentration for effective PET images is as low as 10^{-12} M, therefore, the low concentration will not induce any physiological response from the human body.²⁵

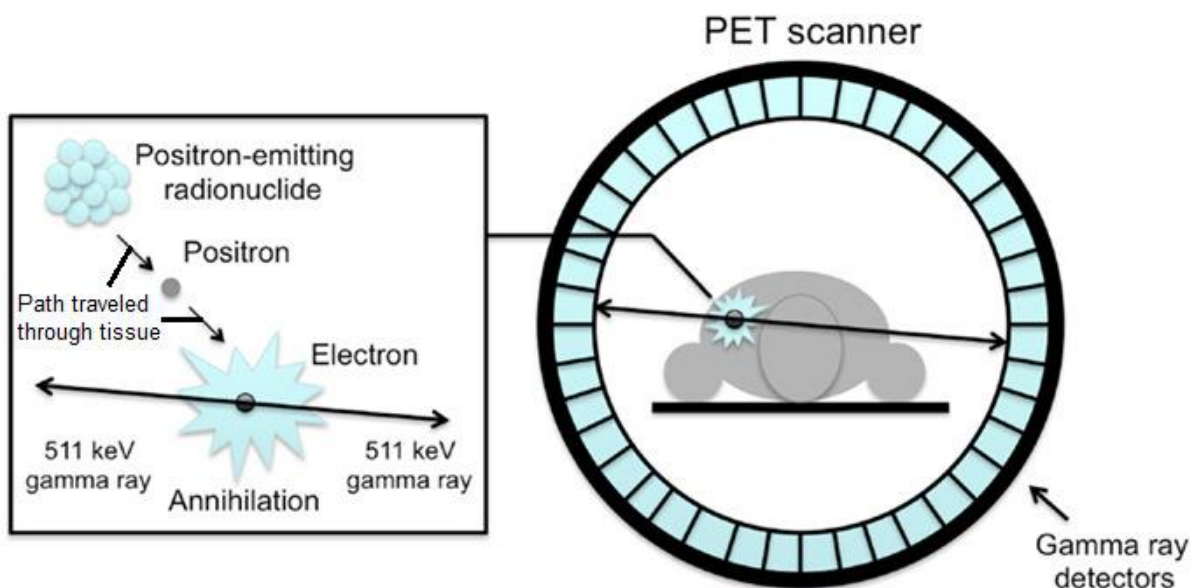


Figure 4: Showing the decay process of radionuclide emitting a positron which travels through the body tissues until it annihilates to generate two photons with energies of 511keV that are detected by array of scintillation crystal.¹⁸³

The annihilation gamma photons are detected by a circular array of scintillation crystals around the patient, see Figure 4. The only photons accepted to form the images are identified when the gamma ray interactions are paired with the opposite side of the detector at the correct energy within a short time interval, which is called the coincidence window.

1.6.2. PET Radionuclides

There are numerous radionuclides suitable for PET imaging. The non-metallic radionuclides that are used for PET imaging have low atomic mass and the capability to substitute stable analogues of organic molecules without affecting the molecule's activity.²⁶ Also, those elements tend to have short half-lives (2-100 min). However, the radiolabelling conditions generally require high temperatures and the short half-life requires onsite cyclotron production, which means that they are not generally appropriate for labelling biomolecules (antibodies/proteins), see Table 3 that shows the characteristics of a range of non-metallic PET radionuclides.

Nuclide	Half life	Maximum positron energy (MeV) and yield (%)	Production
¹¹ C	20.4 min	0.961 (99.8%)	¹⁴ N(p,α) ¹¹ C
¹³ N	9.96 min	1.2(99.8%)	¹⁶ O(p,α) ¹³ N
¹⁵ O	2.04 min	1.73 (99.9%)	¹⁵ N(p,n) ¹⁵ O ¹⁴ N(d,n) ¹⁵ O
¹⁸ F	109.8 min	0.634 (96.7%)	¹⁸ O(p,n) ¹⁸ F ²⁰ Ne(d,α) ¹⁸ F

Table 3: Several common non-metallic radionuclides that can be used for PET imaging.²⁷

The other radionuclide group is metal ion radionuclides. Some of which (although not all) have a longer half life which is more appropriate for labelling biomolecules than the non-metallic radionuclides.²⁸ However, this may cause increased radiation exposure to the patient. On the other hand, the production, complex radiochemistry and transportation processes are more achievable. Some of the metal radionuclides are produced by generator systems, see Table 4 (these generally have shorter half-lives) and the others are produced by cyclotrons and are shown in Table 5.

Nuclide	Half life	Maximum positron energy (MeV) and yield (%)	Production
⁶² Zn/ ⁶² Cu	9.19 hrs / 9.74 min	2.93 (97.4%)	⁶³ Cu(p,2n) ⁶² Zn
⁶⁸ Ge/ ⁶⁸ Ga	288 days/68 min	1.899 (87.7%), 0.821 (1.2%)	⁶⁸ Ga(p,2n) ⁶⁸ Ge
⁸² Sr/ ⁸² Rb	25.6 days/1.27 min	3.38 (95.5%)	⁸⁵ Rd(p,4n) ⁸² Sr

Table 4: Common radionuclides generator systems that provide radionuclides used for PET imaging applications.²⁹

For some metallic radionuclides, higher positron energy leads the positron to travel a longer distance and gives losses in spatial resolution (e.g. gallium-68).

Nuclide	Half life	Maximum positron energy (MeV) and yield (%)	Production
⁵² Mn	5.6 days	0.57 (29.6%)	⁵² Cr(p,η) ⁵² Mn
⁵² Fe	8.27 h	0.80 (55.5%)	⁵² Cr(³ He,2n) ⁵² Fe ⁵⁵ Mn(p,4n) ⁵² Fe
⁵⁵ Co	17.54 h	1.95 (45.7%) 1.311(43.7%)	⁵⁶ Fe(p,2n) ⁵⁵ Co
⁶⁴ Cu	12.7 h	0.65 (17%)	⁶⁴ Ni(p,η) ⁶⁴ Cu
⁸⁶ Y	14.74 h	3.14 (31.9%)	⁸⁶ Sr(p,η) ⁸⁶ Y
⁸⁹ Zr	78.4 h	0.897 (22.3%)	⁸⁹ Y(p,η) ⁸⁹ Zr

Table 5: Common metallic radionuclides generated by cyclotron to be used for PET imaging applications.³⁰

1.6.2.1 ⁶⁴Cu

⁶⁴Cu has a half-life of 12.7 h. This time is sufficient for achieving production and transportation prior to administration to the patient. This metal radionuclide is applicable for a wide range of biomolecule radiolabelling processes.³¹ Using ⁶⁴Cu for PET imaging has the limitation of low image resolution and a higher radiation dose to the patient. ⁶⁴Cu decays by only 17% β⁺ (positron) but with 40% β⁻, which means a higher amount is needed to collect image data but it could also be used for treatment purposes. Cu(I) is very labile in ligand exchange processes as it has a 3d¹⁰ electronic arrangement hence copper(II) is the preferred oxidation state for complex formation.³²

1.6.2.2 ^{68}Ga

^{68}Ga has ideal characteristics for generator production with a parent isotope that has a half life of 271 days. The production of ^{68}Ga is based on ^{68}Ge decay to produce the isotope in a generator.²⁸ It is rapidly becoming a key isotope for clinical use. Recently, ^{68}Ga generators have been made available commercially for clinical trials use and FDA approval has been awarded for one of the generators.³³ The half-life of ^{68}Ga is sufficient for successful imaging with low radiation exposure to patient as ^{68}Ga decays by 89% positron emission. Most applications are focused on labelling of small biomolecules and peptides.¹⁶

^{68}Ga is generally in the oxidation state (III) in aqueous solution and ^{68}Ga is eluted from $^{68}\text{Ge}/^{68}\text{Ga}$ generator using an aqueous acidic solution (e.g. 0.1M HCl). The majority of ^{68}Ga syntheses are achieved in the presence of weak coordinating ligands to exchange and coordinate to a bifunctional chelator (BFC). A BFC is a molecule that provides stable attachment of the radioisotope under *in vivo* conditions and has reactive terminal groups in order to perform bioconjugation with a specific biomarker for targeting. The complex formation between the radiometal and the BFC should occur rapidly under mild conditions in order to prevent any potential degradation of the connected biomolecule and to minimise radioactive decay.

Gallium(III) generally gives 6 coordinate complexes and is considered as a hard Lewis acid and consequently it complexes with hard Lewis base donors such as oxygen and nitrogen atoms. In a comparison between macrocyclic and acyclic BFCs for ^{68}Ga complex formation, acyclic molecules are thermodynamically stable and have a faster metal ion binding but are less kinetically inert than the macrocyclic counterpart BFCs. Currently, ^{68}Ga is receiving a large amount of attention due to the imaging applications of chelator conjugates DOTA-NOC, DOTA-TATE, DOTA-TOC and other DOTA-peptide derivatives which are cancer targeting agents. This research area was initially led by Maecke and co-workers^{34, 35} then more recently significantly advanced by Wester and Baum and co-workers.^{36, 37}

1.6.3 Recent advances in ^{68}Ga chelator design and radiolabelling

The recent research on ^{68}Ga chelator design focuses on R.T complexation of macrocyclic and acyclic chelators in order to improve the ^{68}Ga tracer formation process for clinical PET imaging applications. Radiochemical yield (RCY) is a key parameter, indicating the percentage of complexed isotope radioactivity after complex formation with a chelator (under various reaction conditions and times).

1.6.3.1 Cyclen based chelators

Using the cyclen macrocyclic chelator (1,4,7,10-tetraazacyclododecane) as a base for ^{68}Ga chelator design is a common choice due to the extensive use of DOTA (1,4,7,10-tetraazacyclododecane-1,4,7,10-tetraacetic acid), see Figure 5, in validated imaging and targeting applications.

The bioconjugation of DOTA derivatives with numerous biomolecules has already been achieved by many research groups. However, a general property is slow complexation which requires elevated temperature, limiting their use to biomolecules that are not heat

sensitive.³⁸ Complex formation between ^{68}Ga and p-NO₂-Bn-DOTA occurs either over a long time period at mild temperature or a short time at high temperature (RCY ca. 90%). However, there are other macrocycles with improved properties for ^{68}Ga complex formation namely, p-NO₂-Bn-PCTA and p-NO₂-Bn-Oxo-cyclen which provide higher RCY than p-NO₂-Bn-DOTA of ca. 100% at R.T within 5 min. However these derivatives do not offer the same stability.³⁹ DOTA derivatives and p-NO₂-Bn-PCTA derivatives have similar properties when conjugated to small peptide for *in vivo* applications.

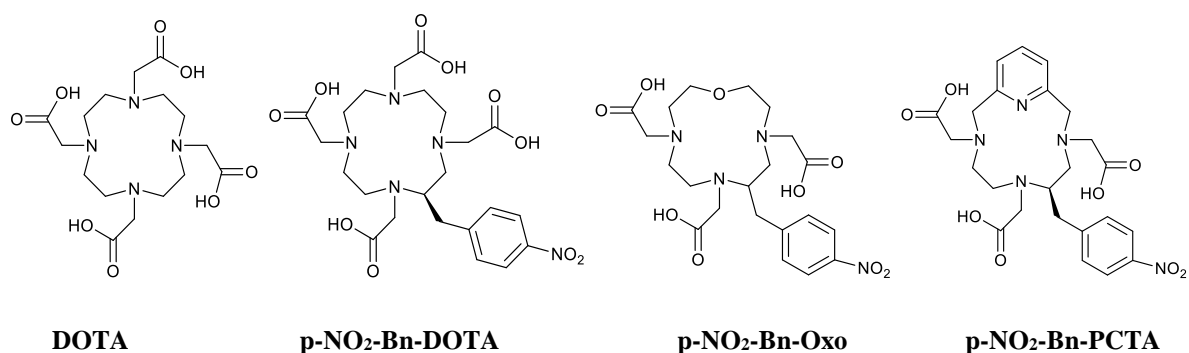


Figure 5: Some common cyclen derivatives used for ^{68}Ga complexation for achieving *in vivo* radiolabelling PET imaging applications.³⁹

1.6.3.2 TACN based chelators

TACN (1,4,7-triazacyclononane) chelators, for example NOTA (1,4,7-triazacyclononane-1,4,7-triacetic acid) provide improved ^{68}Ga radiolabelling characteristics by demonstrating high ^{68}Ga selectivity, high *in vivo* stability and rapid reaction kinetics.^{40, 41}

Currently, the research focused on the design of ligands with improved binding profiles by varying the three pendant arms to include positions for conjugation and/or improved coordination properties, see Figure 6.^{42, 43} TRAP(RGD)₃ was compared to NODAGA-RGD and showed an increased specific activity (10 fold higher) when radiolabelled and *in vivo* results also showed improved target affinity. Another developed system is based on triglutaric acid (NOTAGA), see Figure 6. A conjugate of this compound showed increased tumor uptake at compared to the other ligands.

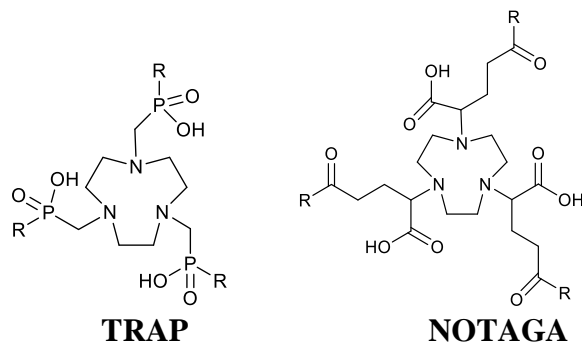


Figure 6: Some common TACN derivatives used for ^{68}Ga complexation for PET imaging applications *in vivo*.⁴²

1.6.3.3. Acyclic chelators

Using acyclic chelators for gallium-68 complex formation offers fast binding kinetics. There are novel designs for acyclic chelators that possess this feature, and high stability, see Figure 7.

A chelator based on the ATSM thiosemicarbazone has been produced.⁴⁴ This chelator was initially investigated using ⁶⁴Cu,⁴⁵ but the group changed the backbone of the ligand by adding an aromatic group allowing the ligand to be labelled with ⁶⁸Ga for multimodal imaging (PET/optical) applications and also the potential of adding a further functional group for modification to allow targeting and optimization of aqueous solubility. The zinc(II) complex was used for labeling through transmetallation which required high temperature in order to give high RCYs. More recently Blower and co-workers produced a novel chelator (CP256)⁴⁶ which radiolabels rapidly (5 min) and gives excellent RCYs (ca.100%) at R.T. Stability tests showed no transchelation under chelator or serum challenge demonstrating high stability for an acyclic chelator.

Another study by Orvig and co-workers synthesized three ligands based on DEDPA derivatives⁴⁷. All three ligands showed fast radiolabelling (10 min) at R.T with high RCYs (98%) and serum stability tests (transferrin) for all the ligands showed no transchelation.

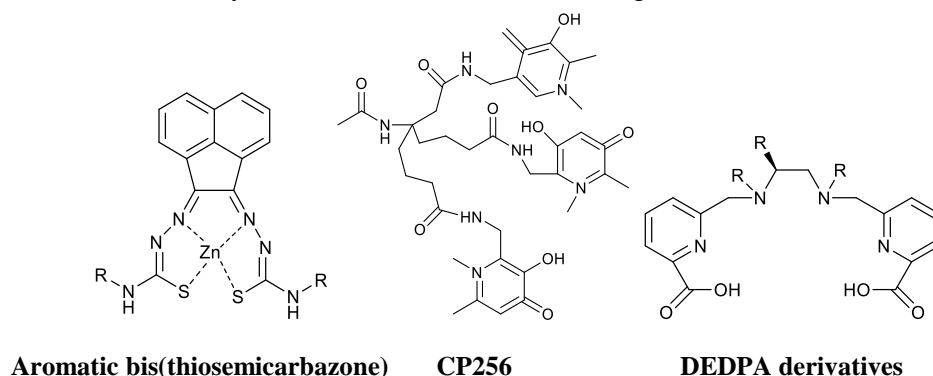


Figure 7: Some acyclic derivatives used for ⁶⁸Ga complex formation in PET imaging applications.⁴⁶

1.7 MRI/PET Multimodal Imaging

Every imaging modality has specific strengths and weaknesses; such as the spatial resolution, sensitivity and temporal dimensions at which they operate efficiently.

Historically, PET was used from the mid-1970s and became the leading technique for cancer diagnosis by the mid-1990s. A fusion of PET and computed tomography CT was established to perform highly sensitive, optimised tumour staging, restaging and anatomic orientation that was much improved over using either PET or CT alone.⁴⁸ Currently, PET/CT is the most important imaging modality for cancer diagnosis and therapy.⁴⁹ However, MRI is very powerful for longitudinal imaging and able to support good images of soft tissue contrast (much better than the CT).

MRI is the best imaging option for imaging muscles, brain, heart and tumours compared with other imaging techniques. MRI has the ability to provide excellent contrast

between different soft tissues, excellent temporal, spatial resolution and a long imaging window. However, for monitoring of small biomolecules such as in cellular processes and small tissue lesions, MRI imaging provides low sensitivity. On the other hand, PET has much higher sensitivities for monitoring such biomolecules.

Research is concentrating on developing the area of fusing MRI/PET^{50, 51} with the first commercial clinical PET/MRI scanners available in 2014 and it is expected that the combination of MRI and PET could potentially surpass the current PET/CT standard.^{52, 53} If MRI can be used with the assistance of targeted magnetic nanoparticles, high resolution images of cancers could be provided and this could be combined with PET imaging to improve sensitivity.

If the SPIONs are labeled with a radioisotope for multimodal imaging (MRI/PET); PET will support highly sensitive recognition of the cancer location over the whole region of interest in the MRI field of view. Using SPIONs as a contrast agent for MRI/PET imaging is a very active area of research. A range of positron emitters have been used for radiolabelling the surface of NPs involving ¹²⁴I, ⁶⁸Ga and ⁶⁴Cu for investigating the targeting efficiency and the *in vivo* bio-distribution of the radiolabelled SPIONs.⁵⁴

1.8.SPIONs targeting and bio-distribution

1.8.1. Passive Targeting

Generally speaking, the biodistribution and localization of SPIONs are dictated by several factors such as the NPs charge, hydrodynamic diameter, thickness of the surface coating and the NPs composition.⁵⁵ There are two main mechanisms for targeting biological site of interest; passive targeting and active targeting.

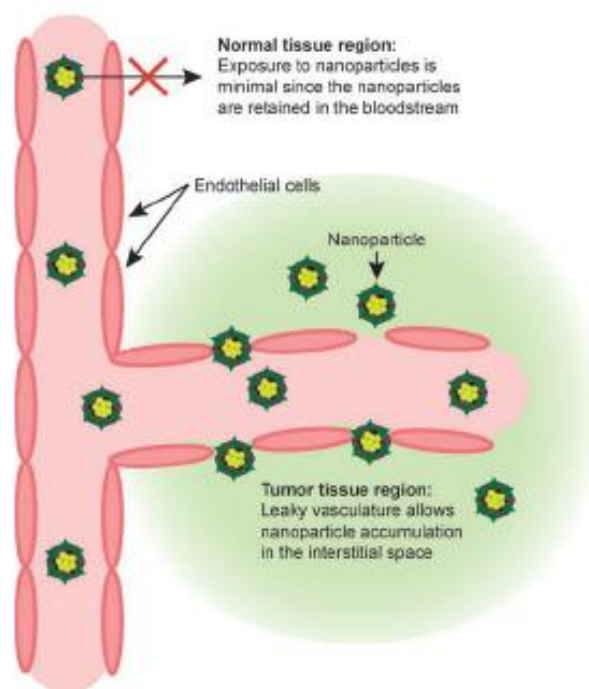


Figure 8: Enhanced permeability and retention of nanoparticles in tumours. Normal tissue vasculatures are tightly lined with cells that preventing nanoparticle drugs from getting out of the vessels, whereas tumour tissue vasculatures are leaky and so nanoparticles can get into the tumour (this is passive nanoparticle tumour targeting). This Figure is reproduced from a literature review published by Nie et al.⁵⁶

Cancer is characterised by rapid vascularisation which means formation of abnormal number of blood vessels and capillaries in the part of the organ that is affected with cancer. This inflammation leads to defective architecture, leaky and impaired lymphatic drainage. The small holes formed on the surface of tumour allow any object with size less than 100 nm to easily enter inside the tumour. Nanoparticles with a size in the range 2-60 nm, and with a biocompatible surface coating may accumulate at the tumour site (Figure 8).⁵⁶

1.8.2. Active Targeting

SPIONs can be functionalized with an appropriate targeting ligand on the surface to selectively bind to particular biomarkers on the site of interest. The active targeting mechanism may allow physicians to accurately diagnose the disease and establish suitable therapeutic treatments personalized to patients. There are a number of biomarkers on cancer being used as a target for SPIONs.

1.9 Summary of the approach taken in this work

In this thesis, the modalities of PET and MRI were chosen due to the clinical relevance. The toxicity of the agent was considered when selecting the multimodality systems and iron oxide nanoparticles are the best candidate as they have a relatively low cost and non-toxic core material which can be combined with a silica shell that is biocompatible. The PET isotope selected is gallium-68 due to the convenient generator production. Validation of targeting potential was attempted using CXCR4 chemokine receptor targeting antagonists that could be displayed on the surface of the nanoparticles. This approach provides and validates many of the steps towards a multimodal PET/MRI imaging construct.

Chapter 2

Iron Oxide Nanoparticle Synthesis and Coating

2.1. Background and Aims

Among numerous materials used for biomedical applications, such as quantum dots, silica, silver, gold and carbon nanotubes (CNTs), the iron oxide materials are promising because of their magnetic properties.^{14, 57, 58}

Over the past decade, superparamagnetic iron oxide nanoparticles (SPIONs) have received major attention due to their potential biomedical applications. They show unique properties such as superparamagnetism which are dictated by the structure and particle size. Therefore, in this work, an exploration of well-established mechanisms for controlling particle size and shape is a critical point for successful formation of SPIONs to be subsequently coated, radiolabelled and targeted.

Many approaches have been investigated for creating SPIONs such as chemical vapour deposition, milling, colloidal chemistry, sol-gel methods and thermal decomposition.⁵⁹⁻⁶¹ Despite the intensive investigations of SPION synthesis methods, there is still further work to be done to determine methods that reliably produces precisely predictable particle shape, size, crystallinity and morphology. However, among numerous synthesis approaches, co-precipitation and thermal decomposition methods are the most commonly utilised methods for generating SPIONs.

This chapter is generally focused on establishing experimental procedures to synthesise SPIONs with controlled size and shape by varying chemical and physical synthesis parameters in order to affect the mechanism of nucleation and crystal growth. The produced SPIONs were further applied to a coating study for investigation of coating efficiency. The most significant innovation in this chapter is the method for synthesis of iron oxide nanorods (IONRs) with a simple modification to the protocol, using an external rare earth magnet, which was remarkably successful.

This chapter provides a brief overview of magnetic properties that are required for biomedical applications, a description of the solid state structure of iron oxide, followed by a review of SPION synthesis and coating methods, (see sections 2.2.2 and 2.2.3). Discussion follows to evaluate methods to determine the SPIONs properties with a number of characterization methodologies.

Experimentally, the co-precipitation method was carried out to synthesise SPIONs, see section 2.3.1. This was followed by an attempt to tune the particle size by adjusting addition speed rates, see section 2.3.1.1. Further study of SPION formation using the thermal decomposition method was also carried out see section 2.3.2. The SPION morphology, size, crystallinity and final yield of both synthesis methods are compared to allow selection of a standard approach for future research, see section 2.3.3. The capability to tune the SPIONs shape and morphology using external magnetic fields was attempted, see section 2.3.4.

The fabricated SPIONs were further subjected to a coating study using two silica coating strategies (direct silica attachment on the SPIONs surface, see section 2.4.1, and ligand exchange silica coating with displacement of oleic acid, see section 2.4.2). The coating material differences were investigated by characterising the NPs shape, size, size distribution, aggregation and surface coverage.

2.2 Introduction

2.2.1 Solid state structures of iron oxide

Over the last decade, nanoscale magnetic materials have been shown to display unique physical and chemical features such as magnetic properties including superparamagnetism.⁶² These properties can be exploited for biomedical applications such as MRI contrast agents, for drug delivery and hyperthermia therapy.^{14, 63} Most of the commonly used magnetic materials include transition metals such as nickel, cobalt and iron. Metals oxides, especially iron oxides, are highly utilised materials for biomedical applications due to the favourable magnetic properties, stability and biocompatibility.

There are around ten different iron oxide compositions including oxido-hydroxides and hydroxides. Among the common types are ferric oxides (hematite α -Fe₂O₃), ferrous oxide (Wüstite FeO), ferrous/ferric iron oxide (magnetite Fe₃O₄), and maghemite (γ -Fe₂O₃). Typically, magnetite and maghemite are ferromagnetic iron oxides which are considered suitable magnetic materials for the production of iron oxide nanoparticles (IONPs). IONPs are generally composed of one or both of magnetite or maghemite which can be crystallised in the cubic close packed form. In a ferromagnetic compound, once an external magnetic field has been applied, the magnetic moments align either along the magnetic field or in the opposite direction of the field. Since the sub-lattices are not equal, hence one is larger than the other, the magnetic properties of the material persist.

Magnetite (Fe₃O₄) consists of trivalent and divalent iron ions arranged in an inverse spinel crystal structure with a cubic close packed array filled with oxygen atoms in a mixture of a tetrahedral sub-lattice containing Fe³⁺ ions only and an octahedral sub-lattice containing a mixture of Fe²⁺ and Fe³⁺, see Figure 9. In Fe₃O₄, an equal number of Fe³⁺ ions are present in each type of lattice site (octahedral and tetrahedral) which leads to the magnetic moments of the Fe³⁺ cations cancelling each other out hence the total net magnetization is decided by Fe²⁺ cations distributed in octahedral sub-lattice sites, such magnetic behaviour is termed antiparallel.⁶⁴

Maghemite (γ -Fe₂O₃) is typically formed by an oxidation of Fe₃O₄. Maghemite is arranged in an inverse spinel crystal structure with vacancies of 2+ cations, in the octahedral sub-lattice due to the oxidation of the Fe²⁺ ions. Therefore, maghemite magnetization is generated from site vacancies of Fe³⁺ cations, accordingly, maghemite is classified as a ferromagnetic material.⁶⁴

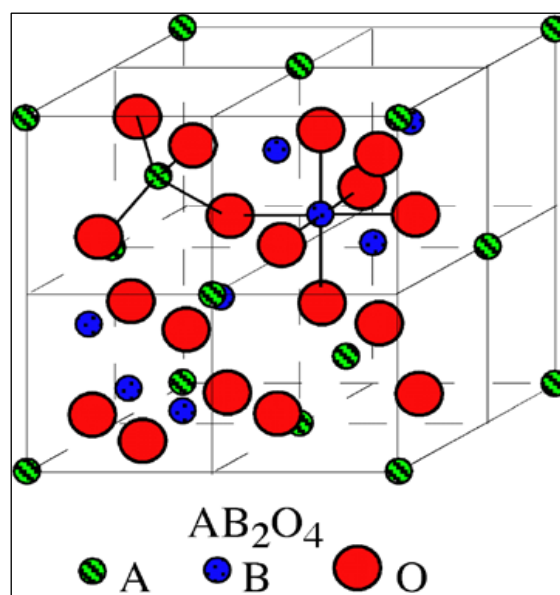


Figure 9: Solid state structure of magnetite. A: represents Fe^{+3} atoms in tetrahedral sub-lattice. B: represent Fe^{+2} atoms in octahedral sub-lattice. O: represent oxygen atoms. Reproduced from Issa et al.⁶⁴

2.2.2 Methods for synthesis of iron oxide nanoparticles

Numerous methods have been used in the preparation of SPIONs including thermal decomposition, polyol, water-in-oil micro-emulsion, sol-gel and co-precipitation methods.⁵⁹⁻⁶¹ Each technique produces variation in the properties of the NPs produced, dependent on the reaction conditions and which procedure is utilised. A brief overview of chemical and physical approaches for synthesis of SPIONs for biomedical applications is given below, see Table 6.

Synthesis type	Description
Chemical approaches	Co-precipitation ⁶⁵
	Thermal decomposition ⁶⁶
	Polyol method ⁶⁷
	Micro emulsions methods ⁶⁸
	Sol-Gel method ⁶⁹
	Electrochemical methods ⁷⁰
Physical approaches	Sonochemical methods ⁷¹
	Flow injection method ⁷²
	Pulsed laser ablation ⁷³
	Aerosol/ Vapor method ⁷⁴

Table 6: Overview of methods for synthesis of IONPs

This chapter focuses mainly on two popular synthetic routes; co-precipitation and thermal decomposition which are commonly known to supply high quality NPs. Regardless of the method used for SPION synthesis, the main mechanism dictating Fe_3O_4 creation is based on nucleation and growth stages expressed by the La Mer plot shown in Figure 10.⁷⁵

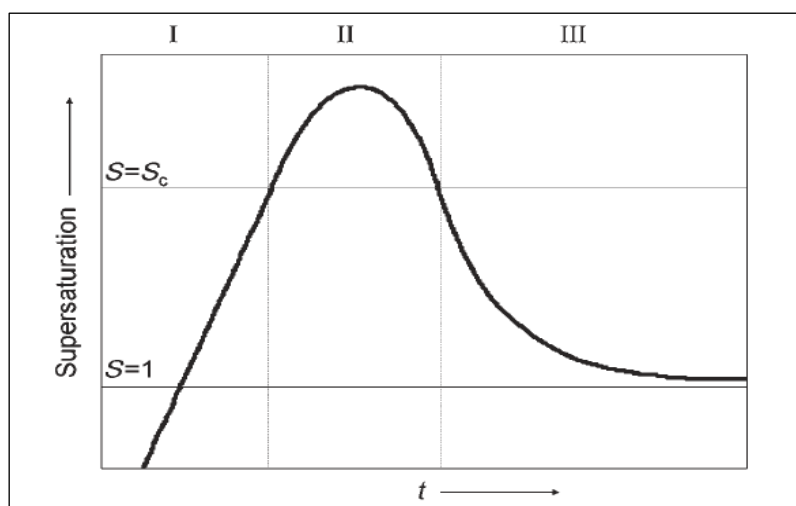


Figure 10: La Mer plot describing synthesis stages for creating of iron oxide nanoparticles from liquid phase into solid phase. The mechanism depends on the iron ion concentration and time. Reproduced from Schladt et al.⁷⁶

As shown in the LaMer plot, there are three stages that the reaction undergoes to give a final product of IONPs.⁷⁵ Initially, decomposition of the iron precursor (either Fe^{3+} or Fe^{2+}) to form iron clusters occurs as stage (I) in the plot. In order to move past the nucleation stage, iron saturation must be attained, which is entirely dependent on iron concentration in solution. The nucleation stage continues to occur until the supersaturating level is less than a critical level ($S=S_c$), stage (II). It has been noted that the nucleation stage is quite rapid and will determine the overall number of NPs formed. Once the highest point of saturation is reached, the growth stage starts which means that the created nuclei keep growing via the diffusion of the iron precursor from the solution to the surface of the nuclei.

2.2.3 Materials for coating iron oxide nanoparticles

Coating of the SPIONs has been given significant attention as there is a wide spectrum of possibilities to improve the SPIONs stability before they are used in biomedical applications. Coating of the SPIONs coated with suitable material is crucial as it increases the SPIONs stability, reduces toxicity and offers the potential for attachment of other molecules such as targeting ligands.

Generally, SPION coating materials can be classified into either inorganic or organic materials. Examples of the inorganic materials include silica⁷⁷ and gold⁷⁸ and organic coating materials include gluconic acid and citric acid.⁷⁹ Inorganic materials form a thin layer around NPs, resulting in electrostatic repulsions for stabilization. An example is the silica coating layer, which has the advantage of stabilizing the NPs via electrostatic repulsions between particles due to the inherent negative charge on the silica surface. Silica is considered as a non-toxic material and highly biocompatible. Recently, silica based contrast agents have been investigated commercially such as Ferumoxsil and NanoTherm.

Organic materials can function as surfactants by creating a bilayer on the NPs surface using long-chain fatty acid monomers. Table 7 shows common materials used clinically and in research experiments for coating iron oxide nanoparticles.

Coating material	Examples	Selected references
In organic	Silica	80
	Gold	81
Organic (monomers)	Citric acid	82
	Gluconic acid	83
Organic (polymers)	Dextran	84
	Polyethylene glycole (PEG)	85
	Polyvinyl alcohol	86
	Polyvinyl pyrrolidone	87

Table 7: Common materials used for coating of iron oxide nanoparticles for biomedical applications.

In this chapter, the produced SPION core materials were then taken forward to a coating study. The coating of SPIONs with silica was achieved, the particles characterized and further work carried out on functionalization

2.2.3.1 Methods for coating iron oxide nanoparticles

Generally, the SPION coating process can be performed through three physical mechanisms: physical adsorption, grafting to and grafting from. Physical adsorption produces interactions between the polymer and SPION surface using weak forces such as hydrogen bonding and van der Waal's. "Grafting to" is a type of approach using stronger interactions such as ionic interactions or covalent bonding by performing a direct attachment between the polymer chains and the SPION surface. In terms of the "grafting from" approach, a polymer coating is built up of monomer units on the SPIONs surface. Figure 11 shows the main coating methodologies using polymer, inorganic and monomeric coatings.¹³

The NP surface coating is a critical process because the NP tend to aggregate once introduced to high ionic strength solutions, such as the human body media. The NP aggregation behaviour is generally a result of magnetic dipole interactions and van der Waal's forces between the particles. Therefore, the coating layer acts to stabilise the NPs by supplying steric or electrostatic forces to optimise the repulsive forces.

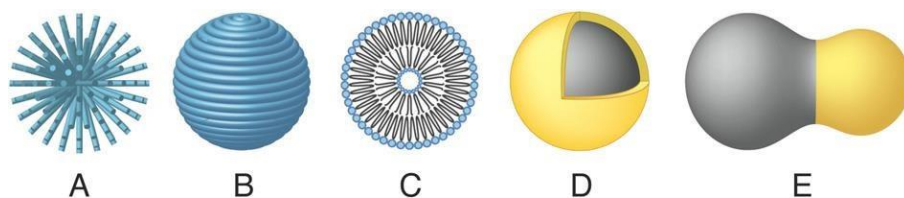


Figure 11: NP structures and coating. (A) End-grafted polymer coated MNP. (B) MNP fully encapsulated in polymer coating. (C) Liposome encapsulated MNP. (D) Core-shell MNP. (E) Heterodimer MNP. Reproduced from Sun et al.¹³

2.2.4 Techniques used for characterisation of nanoparticles

By selection of the most appropriate characterisation techniques, we can determine if the particle properties match the expectations from the coating technique used. Analysis of the different relevant parameters requires different analysis techniques. In this work, the parameters that are of interest are NP size, identity and coating efficiency. Two suitable

characterization techniques that give insight into SPION size and shape parameters are nanoparticle tracking analysis (NTA) and transmission electron microscopy (TEM). To determine the identity and lattice arrangement of the SPIONs, powder X-ray diffraction (XRD) is an ideal technique. Inductively coupled plasma – optical emission spectroscopy (ICP-OES) can be used to analyse the elemental composition of the samples.

2.2.4.1 Transmission electron microscopy

TEM reveals the mean size, morphology and shape of the bare and coated NPs. Images are created by emitting and accelerating electrons from an electron gun to collide with the sample. The interaction between the accelerated electrons and the sample generates two types of interactions: elastic (electrons reflected with no change in energy) and inelastic (post interaction, the energy is reduced for the transmitted electrons). The produced electron beam is passed through an electron lens system to provide focus. The TEM images are constructed based on energy and electron density differences of the transmitted electrons through an ultrathin sample.

2.2.4.2 Inductively coupled plasma – optical emission spectroscopy

ICP-OES technique is an excellent method for identification and quantification of metal concentrations in a sample. The ICP-OES instrument consists of two main parts, an inductively coupled plasma torch and an optical spectrometer. Under elevated temperature at around 7000 K, the inductively coupled argon plasma torch excites the sample elements to give ions. The sample atoms are ionized and excited by the plasma leading to emission of electromagnetic radiation dependent on the sample element types. The radiation intensities generated indicate the concentration.

In general, the nanoparticles were digested in acid prior to analysis but in some cases, using a method developed in the Archibald laboratory, suspensions of the iron oxide nanoparticles were directly injected into the plasma and information was given on the elements on the surface and the thickness of the coating/ exposed iron oxide surface. When fully digesting the samples, a known mass of particles is used (from the solid state) and microwave heating can be used with HCl and HNO₃ for decomposition of inorganic and organic materials. The samples were then diluted in H₂O to give a known final volume. Calibration is carried out by determining elemental content of two standard samples with known concentrations of specific metal ions to allow measurement of samples with unknown concentration. The metals concentration is generated as milligram per litre or ppm.

2.2.4.3 X-Ray Diffraction (XRD)

X-ray diffraction is a powerful technique that gives insight into the atomic arrangement and crystal structures of iron oxides since the distance between the atoms and the wavelength of the X-rays used match sufficiently to cause diffraction. The X-ray is interacting with the sample atom electrons on each crystal lattice point causing X-ray beam diffraction to give peaks at a range of angles and intensities. Therefore, the angle and intensity of each reflection gives information on the atom spaces between crystal planes and the orientation.

This interaction is expressed by Braggs Law:

$$n\lambda = 2d \sin\theta$$

Where, n is an integer, λ is the wavelength of incident X-ray beam and d is variable distance between atomic layers.

Each crystal structure provides unique angles and intensities corresponding to atomic spacing and arrangements. A library of identified material structures is stored in the database to allow matching with previously analysed samples. In this chapter, XRD is used not only to identify sample structures but can also indicate the degree of crystallinity which corresponds to the peak shape (i.e. how consistent is the d -spacing). For example, if the sample is highly crystalline, the diffracted peaks are intense and a narrow range of angles is observed, on the other hand, if the diffracted peaks are less intense and broader this indicates irregular d -spacing which means there is a lower degree of crystallinity. The XRD pattern can also be used to determine the mean particle size using the Scherrer equation to analyse the relationship between the crystallite size and peak broadening, in this case a wider peak indicates a smaller crystallite size. This information can be supported by other characterisation techniques including TEM, NTA and DLS.

For iron oxide crystal structure analysis, IONPs are composed of one or both of magnetite and maghemite which both crystallize in a cubic structure. Therefore, it is difficult to distinguish between them using XRD analysis. A further technique that may be able to differentiate between those types of iron oxide is Mössbauer spectroscopy which exploits the fact that magnetite consists of both of ferric and ferrous ions whereas maghemite only consists of ferric ions. In contrast, other iron oxide materials, such as hematite which has a hexagonal crystal structure is easily differentiated using powder XRD. Ferrous oxide, Wüstite (FeO), is extremely sensitive to oxidation and is rarely found in IONPs.

2.2.4.4 Nanoparticle tracking analysis (Nanosight, NTA)

The Nanosight technique is an excellent method for analysing particles size and size distribution. The measurements obtained are based on Brownian motion and light scattering properties. The motion of the particles is detected by laser beam scattering when laser light is passed through the sample chamber. The scattered laser light is captured and visualised using a microscope with a camera operating at 30 frames per second. The particles are tracked individually and the Stokes-Einstein equation is used to calculate the mean particle size.

Both NTA and DLS (dynamic light scattering) are techniques that calculate the particle size in relation to their movement. NTA has the ability to track particle movement on a particle by particle basis by visualizing the motion of each particle in real time. In contrast, DLS calculates the particle hydrodynamic size based on a time dependent fluctuation in scattering intensity that is caused by destructive and constructive interference from particle movement.

In the synthesis experiments in this work, it is expected that a range of particle sizes (poly-disperse) are always present in the final products due to unavoidable aggregation and only moderate control of the NPs size distribution. In this case, NTA is the most suitable technique for analysing the samples as particle by particle measurement is provided. Experiments in this work aimed to reduce the nanoparticle size by changing the synthesis

parameters. NTA is an excellent technique for monitoring this parameter as DLS gives an average particle size and any aggregation will bias the measurement towards the larger particles.

2.3. Synthesis of superparamagnetic iron oxide nanoparticles (SPIONs)

2.3.1. Synthesis of SPIONs via the co-precipitation method

Co-precipitation is a method to fabricate particles from a metal salt in aqueous solution leading to synthesis of magnetic particles with an appropriate size for biomedical applications. Co-precipitation is a convenient way to produce a high yield of NPs with no need for purification and reliably produces NPs with a narrow size distribution and homogeneous composition. The main aim of the NP syntheses in this work is to fabricate iron oxide nanoparticles with a homogeneous composition, spherical shape, high yield, size less than 100 nm and a narrow size distribution.

Formation of Fe₃O₄ in aqueous solutions was first reported in 1925 by Welo et al.,⁸⁸ who conducted a study of mixing Fe³⁺/Fe²⁺ in aqueous conditions to produce magnetite. Later, in 1956, Buchi et al.⁸⁹ improved the quality and yield of the produced NPs by incorporation of KNO₃ as a partial oxidizing agent at high temperature. Then, Massart et al.⁶⁵ achieved one of the most effective approaches for generating stable “naked” SPIONs in the absence of an organic surfactant, avoiding the formation of undesired iron impurities by making a magnetic colloidal suspension through mixing Fe³⁺/Fe²⁺ under alkaline conditions.

To achieve the aim in this work of isolating a high yield of SPIONs with a small size and a low percentage of aggregation, a few methods were attempted. Initially, a literature method that was reported by Young Soo Kang et al.⁹⁰ was followed which is based on aging a stoichiometric mixture of ferric and ferrous ions following the reaction:



The reaction contains a mixture of Fe²⁺ and Fe³⁺ in a molar ratio of 1:2 at alkaline pH (pH 9) and mixed under Ar flow. This is the nucleation stage and occurs in a short time, forming iron oxide nuclei seeds before a slow process of crystal growth takes place by the diffusion of iron precursors from the solution to the surface of nuclei. The formed magnetite particles are highly sensitive to oxidation, therefore, an inert gas was flowed over during the reaction to prevent the magnetite transformation to maghemite (**compound 1**). After fabrication and purification of these SPIONs, a degree of aggregation was observed as the NPs tend to aggregate in order to reduce the surface tension.

A combination of XRD, TEM and NTA characterization techniques were used to analyse the composition, shape, size and size distribution of the produced SPIONs. XRD confirmed the identity of Fe₃O₄ and was used to determine which iron oxide compounds were present in the sample. TEM and NTA were also used to characterise the NPs.

The TEM images see Figure 12; show that the SPIONs are an irregular roughly spherical shape with uniform sizes. Although, the suspension shows some degree of aggregation, as observed by eye, a sonicator instrument was used to restore the NPs to suspension. The NTA results show that there is actually a broad size distribution in suspension that ranges from 17 nm to 150 nm. The mode size of 28 nm and the average size

of 93 nm for **compound 1** indicate that aggregation occurs even in the presence of HCl. The main advantage of using such a method is that there is no surfactant added to stabilise the NPs, therefore, they can be used directly in future experiments without additional purification steps to remove the surfactants. However, after one week, the NPs agglomerated, consequently, a stabiliser is needed in the experiments unless the synthesised NPs are stored under oxygen free conditions and used within a short period of time after fabrication.

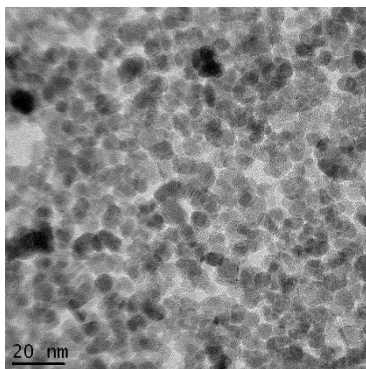


Figure 12: TEM image of Fe_3O_4 nanoparticles showing the spherical shape. NTA: Mode: 28nm, Mean: 93nm, SD: $\pm 100\text{nm}$.

XRD diffraction peaks reflecting crystal lattice arrangement were observed, see Figure 13. The X-ray powder diffraction pattern of SPIONs has peaks at 2θ angles of 30° , 35.4° , 43.2° , 54.3° , 58.2° and 63.1° corresponding to the Miller indices of inverse cubic spinel lattice of magnetite at (2 2 0), (3 1 1), (4 0 0), (4 2 2), (5 1 1) and (4 4 0) respectively.

The patterns were shown to coincide with the JCPDS database for magnetite (JCPDS file 19629; Joint Committee on Powder Diffraction: Swarthmore, PA). The shape of peaks in the diffraction pattern can be an indication of the degree of crystallinity in a sample. In this case the peaks of the diffraction pattern seem to be of a reasonable intensity and relatively narrow indicating that the crystalline d-spacings are fairly regular.

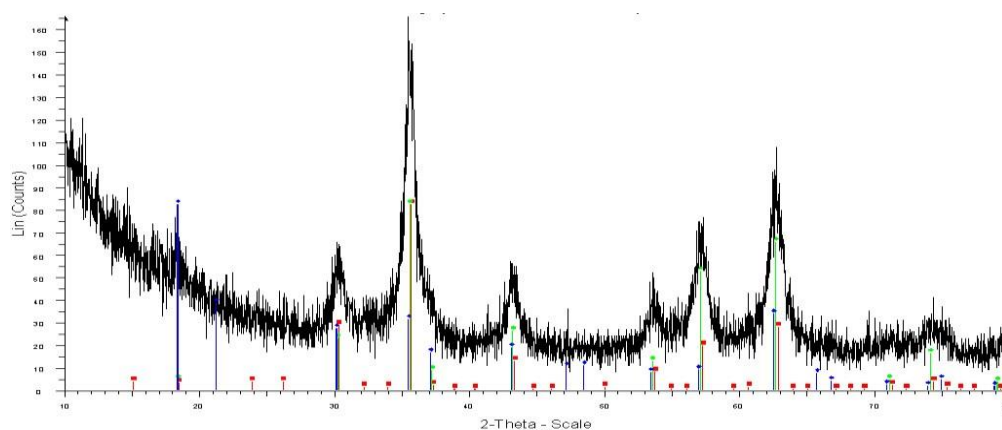


Figure 13: XRD peaks of iron oxide nanoparticles formed by co-precipitation method. The peaks match the expected pattern for magnetite.

2.3.1.1. Varying experimental parameters to influence SPION morphology and size distribution.

Generally, the co-precipitation method provides moderate control over NPs size and size distribution because only kinetic factors are controlling the nucleation and growth stages.

The reagents and conditions have been varied to study the effect of different factors on the produced NPs sizes. Pedro Tartaj *et al*⁹¹, studied the effect of iron concentration on SPIONs size and size distribution. They concluded that using high concentrations of the iron precursor to give a saturated solution, overcomes the energy barrier and the nucleation stage can occur quickly, leading to improved monodispersity and narrow size distribution. If the iron concentration was saturated, some particles that nucleated later combined with existing particles to grow non-uniformly, hence a long nucleation time gives a wider range of particle sizes.

A number of studies focused on probing the influence of other parameters on the properties of the produced NPs, aiming to control the NPs sizes by varying chemical components such as the base used (NaOH, NH₄OH), pH value, cations present (NH₄⁺, Na⁺, K⁺, Li⁺), iron concentration and ratio, temperature and ionic strength.⁶⁵ It has been concluded that those parameters have the ability to control NPs average size to between 4 to 150nm and influence the potential for aggregation.⁸² Each component is able to provide a limited range of control on NPs sizes. Pedro Tartaj *et al.*⁹¹ produced data to show how iron concentration and the timing of addition can affect the nucleation and growth stages of the produced NPs sizes using the co-precipitation method. Pedro Tartaj *et al.*⁹¹ also investigated the effect of base addition time on the produced NPs size. The assumption was that, as it is favourable to perform the nucleation stage in a short time and for it to be separated from the growth stage, the speed of base addition may be able to influence this. The success of this process is reflected in the small NP size and narrow size distribution of the isolated material. In the work in this thesis, it was assumed that faster base addition leads to shorter nucleation time therefore and more monodisperse NPs due to shortening the nucleation time allowing the growth stage to take place earlier which leads to smaller nanoparticle seeds and lower capacity for iron to grow on the NPs surface to provide smaller NPs sizes.

Hence the only variable in the reaction carried out is the base solution addition time and all other chemical factors were fixed across all of the reactions with the conditions as follows: a ratio of ferric and ferrous ions of 1:2, NaOH (1.5 M, 20 ml) and HCl (0.01 M, 500 ml). The basic solution addition speed was monitored. Three different reaction periods were tested to determine the role of rate of addition of the base on the final SPIONs sizes (5, 10 and 30 min), to give **compounds 2, 3 and 4** respectively.

In this experiment the size variation was the main objective, therefore, TEM and NTA analysis techniques are sufficient to confirm average size of SPIONs and would detect any aggregation within the suspension. The hypothesis is based on the fact that, when the critical iron concentration is attained, nuclei are created and a homogenous growth stage is initiated by diffusion of iron precursors from the solution over the nuclei surface creating the NPs. As already mentioned, for creation of uniform and monodisperse NPs, the nucleation and growth stages must be separated. If the reaction is allowed to continue for

too long a time, the particle size will continue to increase until a maximum size is reached. The hypothesis can be summarised by describing the effect of base addition on both of nucleation and growth stages. Nucleation occurs when a highly basic solution such as NaOH is added drop wise to solution containing FeCl₂/FeCl₃. If the NaOH is added in a short time, the nucleation seeds are obtained homogenously, therefore, most of created nuclei grow simultaneously in the growth stage to give a monodisperse and narrow size distribution. Slow NaOH solution addition results in longer nucleation time, therefore a longer growth time occurs and the produced SPIONs are expected to be larger with a broader size distribution.

For the SPIONs, fabricated with various basic addition times (5, 10 and 30 min, **compounds 2, 3 and 4** respectively) the NTA results showed inconsistent NPs size distributions were observed that were not reproducible on repetition with the same parameters. TEM image analysis see Figure 14, confirms that the SPIONs have a spherical shape and appear to have homogenous sizes but although trends appear to be observed it should be noted that differences between sizes determined by TEM as a function of basic addition times are not significantly different due to the large standard deviations.

Sample	Base addition timing	Mode	Mean	SD
4	5 min	29nm	94nm	±51nm
3	10 min	32nm	76nm	±29nm
2	30 min	43nm	55nm	±14nm

Table 8: NTA results with various basic solution addition times. Faster base addition appears to show a smaller mode size and more aggregation but there is a large standard deviation due to the polydispersity.

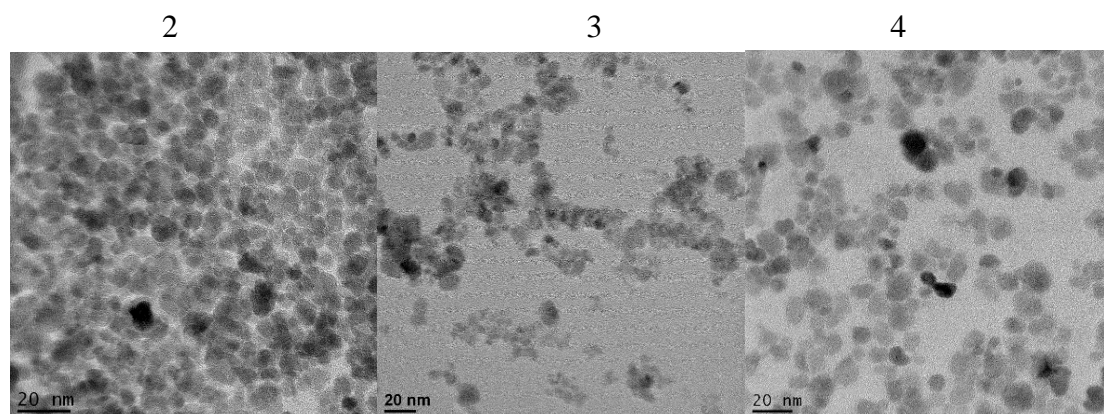


Figure 14: TEM of NPs synthesised with co-precipitation method with various base addition timing. The times 30 min **compound 2**, 10 min **compound 3** and 5 min **compound 4**.

This demonstrates that although a smaller mode size can be achieved with rapid addition of base, the NPs aggregation is increased to also give some very large particles, inconsistent with expectations. Unfortunately, these results were shown not to be very reproducible hence other methods were investigated.

2.3.2. Synthesis of SPIONs using thermal decomposition method.

Using elevated temperature to synthesise SPIONs from a mixture of metal complexes in the presence of surfactants has been shown to be one of the most effective ways to tailor the SPIONs size and shape with minimum aggregation.

In this section, the aim is to synthesise SPIONs using the thermal decomposition method. The results can be compared with the previously prepared co-precipitated NPs to determine which will be the optimum method for this work. As already mentioned, the SPION properties that are desired include small size (5 to 50 nm), low percentage of aggregation, high yield, monodisperse NPs, simplicity, reproducibility and low cost of the reagents.

Using high temperatures for producing SPIONs was first introduced in 2001, by Alivisatos et al.⁹² who fabricated SPIONs from a solution containing the metal precursor, the cupferron complex, in trioctylamine. The final product was uniform nanocrystals with a size range between 7-12 nm. If the temperature or the iron precursor concentration is reduced then the nanocrystal size is influenced. Later, Hyeon et al.^{93,94}, developed a similar system but used $\text{Fe}(\text{CO})_5$ for creating monodisperse SPIONs. The size distribution that resulted was a very narrow 5%. In 2004, Woo et al.⁹⁵ demonstrated that larger NPs can be obtained by increasing the ratio of oleic acid to $\text{Fe}(\text{CO})_5$. In 2002, Sun et al.⁶⁶ conducted a study using solvent boiling point to precisely control SPION sizes with a general size less than 10 nm and a narrow size distribution using an iron(III) acetylacetonate precursor ($\text{Fe}(\text{acac})_3$). The size and size distribution were controlled by varying the reaction boiling point by switching between phenyl ether (ca. 4 nm particles) and benzyl ether (ca. 6 nm particles).

The method described by Sun et al.⁶⁶ was selected as a starting point for this work because of its simplicity. A mixture of $\text{Fe}(\text{acac})_3$ as iron precursor, 1,2-hexadecanediol, oleic acid and oleylamine as surfactants and capping agents, was used. The $\text{Fe}(\text{acac})_3$ had been shown to react effectively with polyalcohols such as 1,2-hexadecanediol to yield the SPIONs under reflux.⁶⁶ Using a combination of oleic acid and oleylamine had previously resulted in a high yield and monodisperse SPIONs as they stabilise the NPs by the presence of alkylamine surfactants to coordinate with Fe(III) on the surface of the particles.⁹⁶ The role of surfactants is to surround the nuclei to restrict the NPs from growing inconsistently and to stabilise the NPs by applying steric forces on NPs surface to keep NPs from aggregating. Phenyl ether was used as a solvent to give a high temperature for reflux (ca. 260°C) and to give small size NPs.⁶⁶ **Compound 5** was synthesised using this method.

In this experiment, the iron compound $\text{Fe}(\text{acac})_3$ was decomposed at elevated temperature in a non-polar solvent (phenyl ether) with the presence of capping agents (1,2-hexadecanediol, oleic acid, oleylamine). The iron precursor was heated up gradually to reach 230°C before being held at that temperature for a specific period of time (the nucleation stage period). The nucleation stage starts at temperatures from 200 to 230°C whereas the growth stage starts at temperatures from 260 to 290°C, which is the boiling point of phenyl ether solvent.⁶⁶ The presence of capping agents influences the NPs size and acts as a colloidal stabiliser, as previously stated.

In this reaction, the SPIONs are created in four different stages. The first stage is the decomposition of the chelated iron precursor in order to form the free components. The following stages are the ones previously observed; nucleation, growth and the equilibrium stage. It is assumed that the capping agents promote the iron precursor decomposition rate, therefore it is the nucleation rate which dictates the NPs final size. The $\text{Fe}(\text{acac})_3$ starts to decompose at a temperature of 75°C , whereas if there is a mixture of capping ligands, the thermal stability is significantly increased which results in the higher decomposition rate occurring at around 210°C . When the nuclei enter the growth stage, the chelated iron precursor diffuses onto the surface of NPs. As the reaction proceeds, larger NPs are obtained until the equilibrium is reached.

In this work, the prepared NPs were suspended in a non-polar solvent such as hexane due to the hydrophobic nature of the oleic acid coated SPIONs. Therefore, transferring the hydrophobic NPs to aqueous suspension is critical before they can be used in biomedical applications. The NTA results show that the obtained NPs, **compound 5**, have a mode size of 9 nm and mean size of 8 nm. This confirms that the NPs are quite monodisperse with a narrow size distribution. The key factor for synthesising monodisperse SPIONs is the tuning of the temperature by initially increasing the heat gradually to attain 230°C within 30 minutes, then increasing the heat to reflux in a single process. Previous research has shown that increasing the temperature quickly resulted in a wide range of NPs sizes.⁶⁶ The TEM images of **compound 5**, Figure 15, confirm that the formed NPs have a narrow size distribution, a spherical shape and that no aggregation is observed with a range of NPs sizes between 3 to 4.5 nm size.

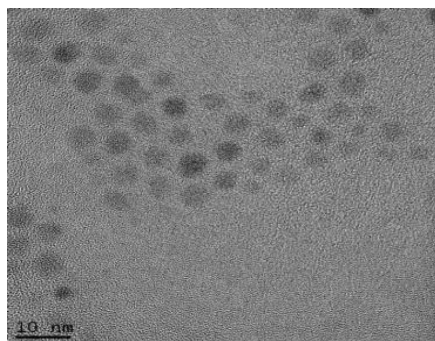


Figure 15: TEM of NPs synthesised with thermal decomposition method

The powder XRD analysis of the compound 5 SPIONs synthesised by thermal decomposition from $\text{Fe}(\text{acac})_3$ is shown in Figure 16. The diffraction pattern of the synthesized SPIONs has reflection peaks at 2θ values of 30° , 35.6° , 43° , 54.5° , 58° and 63° corresponding to the typical Miller indices of inverse spinel magnetite: (2 2 0), (3 1 1), (4 0 0), (4 2 2), (5 1 1) and (4 4 0) respectively. The patterns were found to match with the JCPDS database pattern for magnetite (JCPDS file 19629; Joint Committee on Powder Diffraction: Swarthmore, PA).

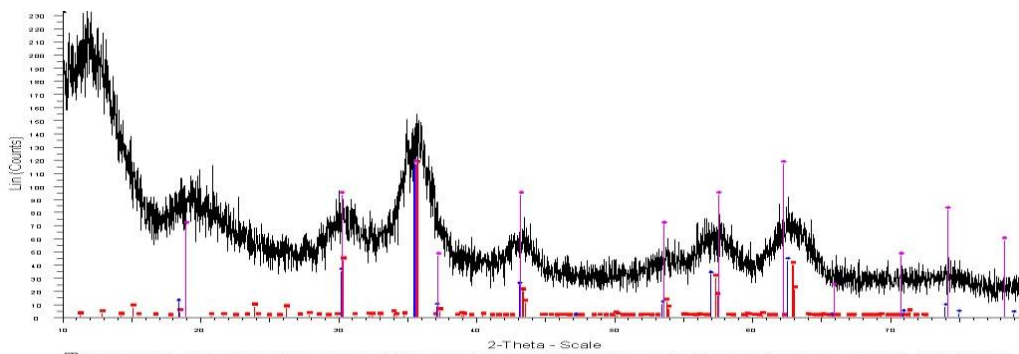


Figure 16: XRD peaks of iron oxide nanoparticles formed by thermal decomposition method. The peaks representing magnetite material crystal atomic identity.

In this case, the peaks of diffraction pattern have low peak intensities and broad or wide peaks which means inconsistent or irregular d-spacing, hence a low degree of crystallinity.

2.3.3 Comparison of co-precipitation and thermal decomposition methods

The co-precipitation method has many advantages such as low cost, high yield, water solubility and simplicity. On the other hand, it only offers moderate control of SPIONs size, size distribution, shape and crystalline structure. Also, in our work, the attempt to control SPIONs sizes by varying the base addition speed was not reproducible. The thermal decomposition method offers improved control of the particle size and size distribution by variation of the rate of heating. However, this method is more complex and has more steps, hence requiring between a few hours to a few days to complete the reaction to synthesise the NPs. Also due to their initial organic soluble nature, a further reaction step is needed to convert them to being water soluble by altering the coating. The thermal decomposition reagents are more expensive and it is a low yielding reaction. Some of the limitations could potentially be avoided by adapting some other known procedures, for example following the experimental protocol reported by Hyeon et al.^{93, 94}

Despite limitations in terms of particle size control and distribution, the co-precipitation method was selected as standard method for future experiments in this work as aggregates can be removed by filtration and as the initial yields are high, this is not problematic. Comparing the powder XRD data from the two methods, the NPs formed using the co-precipitation method show more regular d-spacing and higher crystallinity.

2.3.4. Synthesis of iron oxide nanorods (NRDs) using the co-precipitation method

Commercial products of IONPs such as Feridex, Combidex and Resovist have been used as MRI T₂ contrast agents.²⁰ These contrast agents generally have lower than optimum relaxivity due to their large size and poor crystallinity.⁹⁷ Two key factors that dictate relaxivity are the NPs surface area and saturation magnetization (MS) value.

Several studies have focused on enhancing the NPs magnetic moment by tuning NP size and surface properties.^{98, 99} It was found that there is a linear relationship between R₂ relaxivity and NPs size. However, a significant improvement in R₂ relaxivity can also be obtained by tuning the NPs shape and morphology. This stems from shape anisotropy which

can induce a strong magnetic field.¹⁰⁰ NPs shape and size are key factors for dictating the final product magnetisation properties. For particles with a rod like shape, the length of NRDs has a significant effect on R_2 relaxivity. An increase in the NRDs length leads to increase in R_2 relaxivity.¹⁰⁰

The main aim of this work is the synthesis of NRDs to generate MRI T_2 weighted contrast, the surface area is directly correlated to the field perturbation area and NRDs have a higher surface area than the spherical NPs. An attempt to exploit the resulting particles shape to improve MRI T_2 weighted contrast as part of a multi modal imaging agent (MRI/PET) will be discussed in chapter 3.

A study was performed by Wei-Wei Wang et al¹⁰¹, to prepare Fe_2O_3 nanorods used a silica template under hydrothermal conditions to produce magnetic silica/ Fe_2O_3 nanorods after reduction of the precursor under an inert atmosphere.

In this experimental work, the synthesis of iron oxide nanorods (NRDs) was carried out using the co-precipitation method in the presence of a strong rare earth magnet in close proximity to the reaction flask during the SPIONs synthesis to produce NRDs. The plan is to use the shape effect in enhancing MRI R_2 relaxivity and it will also provide a higher capacity for loading of radioactive species onto the surface for future multimodal imaging (MRI/PET) applications. The magnet is placed in close proximity to the reaction, during the iron NP formation, the formed iron nuclei are attracted toward the magnet, the growth stage occurs by diffusion of the iron precursor over the formed iron nuclei in alignment with the magnetic field and so the particles grow along the magnetic field axis forming a rod-like structure.

The method for creating SPIONs was inspired by the report from Young Soo Kang et al⁹⁰ which utilised a rare earth magnet to influence particle formation. TEM and nanosight (NTA) are the most suitable techniques for analysing the resulting particle shape, size and size distribution of the NPs **compound 6**. The solution containing $FeCl_3 \cdot 6H_2O$ and $FeCl_2 \cdot 4H_2O$ in a 2:1 ratio was added to a solution of diluted HCl (0.1M). The acidic solution was degassed by bubbling N_2 through it prior to the reaction to prevent oxidation. Once the basic solution (concentrated aqueous ammonia) was added drop-wise, the production of NPs was immediately occurred with an increase in black colloidal material observed on addition of the base solution in the presence of the rare earth magnet. After purifying the produced NRDs via successive washing steps, the NRDs were dried under vacuum and stored in an inert atmosphere before being analysed (**compound 6**).

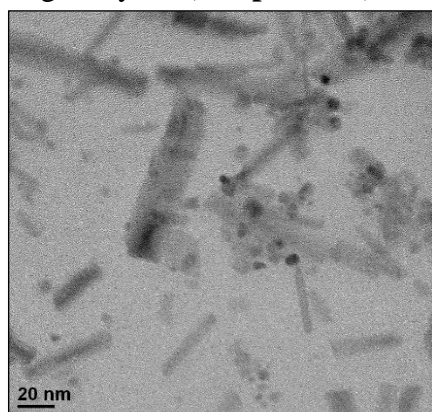


Figure 17: TEM results of synthesised NRDs (**compound 6**) via the co-precipitation method under application of an external magnetic field during the base addition step

Figure 17 shows TEM images of the synthesised NRDs. This clearly shows the effect of the magnetic field on the formed nanomaterial shape by showing a mixture of spherical NPs and rod like particles NRDs. The NRDs presented with various lengths ranging from 20 nm to around 100 nm. NTA results show that the mode size of NRDs of 20 nm and an average size of 38 nm. Generally, for *in vivo* use the particles should be smaller than 100 nm.

2.4 Silica coating of SPIONs

2.4.1 SPIONs coated with silica using a direct attachment strategy

For biomedical applications, using bare SPIONs has several issues such as aggregation at physiological pH and protein interactions. Therefore, using a coating material is a vital step. Numerous coating materials have been used previously such as dextran, PEG, chitosan, gold and silica. Among them, the silica coating has the advantage of improving the NPs chemical stability, preventing aggregation, offering protection against toxicity and most importantly it is simple and offers the potential to perform synthesis, coating and functionalization in a one-step reaction.¹⁰² Commercial silica compounds are available with a wide range of terminal groups allowing the NPs to be surface functionalized. Silica is negatively charged which leads to an improvement in the coulombic repulsion of the NPs to give stabilized NPs in suspension.¹⁰³ For *in vivo* multimodal imaging the SPIONs must be highly stable under a wide range of pH and salt concentrations.

There are various methods used for the silica coating process. A method known as the Stober process in which the silica coating takes place through the formation of a sol-gel precursor has been applied successfully in reported studies.^{104, 105} Another method is to apply the coating based on deposition of silica from silicic acid solution.¹⁰⁶ This method is straightforward and the final NPs size can be controlled by varying the silica/Fe₃O₄ ratio. A further method using emulsion micelles or inverse micelles can also be used in the silica coating process. This method requires a large amount of surfactants and purification from excess surfactants associated with the emulsion system.^{107, 108}

In the experimental protocol applied in this work, the siloxy compound agent was directly attached to the co-precipitated SPIONs surface, forming a silica shell which allows coating and functionalization of the NPs surface in a one pot reaction to give particles with an appropriate size and size distribution. The particles can be further reacted with other siloxane derivatives to attach to the silica surface of the NPs. There are many different siloxane reagents commercially available with a variety of different terminal functional groups. The mechanism by which the silica coats the SPIONs is based on the interacting hydroxyl end groups presenting to the SPIONs surface and the methoxy groups on the siloxane molecules acting as leaving groups to form Si-O-Si bonds, releasing methanol, to give the solid state silica structure on the surface of the NP.

To date, many researchers have reported direct attachment of different molecules on the surface of NPs using siloxane reagents. In 2007, Yu et al.¹⁰⁹ used peptides to modify the surface of silica coated SPIONs. The particle size ranged between 22 nm to 62 nm and it was considered a promising strategy. Later Jana et al.¹¹⁰ developed a similar system but using an antibody attached to the silica coated SPIONs. The main aim of these researchers was targeting cancer cells using the attached peptides or antibodies. In 2011, Barreto et al.¹¹¹

reported a methodology for coating SPIONs with a silica layer using siloxane precursors including the attachment of radionuclide complexes. This experiment was designed for PET nuclear imaging purposes which is also one of main aims in this thesis. The size distribution of the coated NPs ranged between 5 to 35nm which is suitable for the application. Therefore, this experimental methodology was followed with some minor variations such as the use of unfunctionalised siloxane precursors (GPTES) alone rather than the functional derivatives used by these researchers to form a construct for radiolabelling. As will be seen later in this work a novel series of macrocyclic derivatives can also be utilised with this method.

Generally, for good surface coverage of the silica onto the NPs, the siloxane to iron ratio used can be as high as 10 to 35 times in excess.¹⁸³ In this experiment, significantly lower siloxane derivative to iron ratios were used to investigate how effectively the surface could be covered and to reduce wastage of the more complex and higher value functionalised reagents in the subsequent reactions. SPIONs were produced using the co-precipitation method, then the siloxane derivative was reacted by mixing the SPIONs suspension with GPTES (0.5 ml) in ethanol solvent for 48 h at R.T. under oxygen free conditions. The produced SPIONs were washed and dried to be further characterized later (**compound 7**). The compounds were analysed using a combination of TEM, NTA and ICP-OES. TEM was used to confirm that the particles had been synthesised and their shape. NTA was used to detect any aggregation after coating. ICP-OES quantifies the iron and silica content in the sample.

NTA results show that bare NPs mode size was 22 nm and mean size at 31 nm. Once the NPs were coated with a silica layer the mode size became 38 nm and the average size became 54 nm. Those results show an increase in hydrodynamic size which could be due to aggregation occurring between the NPs via the silica polymer coating. This may not be an issue as the particles can be filtered to remove any of the larger aggregates. TEM, see Figure 18, shows that spherical SPIONs were produced with a relatively monodisperse size of ca. 20 nm diameter, although it is unlikely the silica coating will be visible in the TEM.¹³⁸ Bare NRDs give iron percentage at 57.9%. After NRDs silica coating process, ICP-OES shows the presence of the silica on the surface of NRDs. This indicates a relatively low coverage but may be sufficient for the required suspension stability. The silica is still present on the SPIONs surface after successive washing cycles indicating stable attachment. A variety of characterization techniques could be used to investigate the silica thickness layer around the NPs such as EDX, SEM and/or AFM.

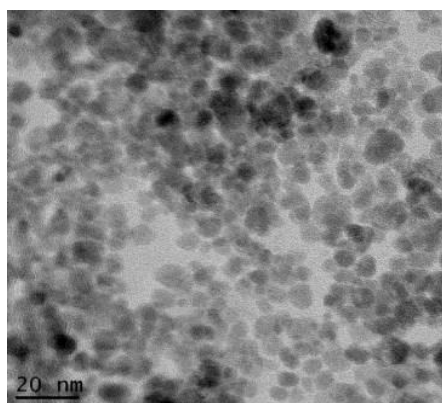


Figure 18: TEM of co-precipitation synthesised NPs coated with a silica layer via the direct attachment method

2.4.2. SPIONs coated with silica using a ligand exchange strategy

Coating SPIONs with organic surfactants, such as a fatty acid (oleic acid), to stabilise the particles during synthesis by giving a bilayer surface around SPIONs is a useful technique. This allows more efficient coating, smaller particle size by restricting particle-particle crosslinking, less oxidation and is highly re-producible. The role of the fatty acid layer is to provide monodisperse SPIONs with a spherical shape. The NPs can subsequently be converted from the organic phase to the aqueous phase by exchanging the oleic acid with a different coating.¹¹²

Yabin et al.¹¹² studied the structure and stability of NPs coated with a fatty acid layer. An observation of a gradual increase in the NPs hydrodynamic size in water was noted after coating. The same study proved that using fatty acid as stabiliser provides biocompatible NPs after ligand exchange. In 2009 Esben et al.¹¹³ used commercially available siloxane-PEG derivatives to introduce a biocompatible silica shell on the surface of co-precipitated NPs by replacing the oleic acid layer with siloxane-PEG molecules using the ligand exchange method. The final product size was separated into two sizes of diameter ca. 20 nm and 40 nm with higher phagocytic uptake of the 40 nm size observed *in vitro*.

In this work, the procedure used by Esben et al.¹¹³ was followed with some minor modifications. Initially, the SPIONs synthesised were coated with a layer of oleic acid as a surfactant. The addition of oleic acid was at elevated temperature condition with dropwise addition to form SPIONs stable in non-polar solvents such as hexane or toluene. To make the NPs water soluble, the hydrophobic oleic acid was replaced by a silica coating using a siloxane derivative (GPTES) molecules via a ligand exchange mechanism. The adsorbed oleic acid on NPs surface is only weakly bound and can be displaced by higher affinity molecules on the NPs surface. For efficient coating, to form stable SPIONs, a high ratio of siloxane to oleic acid (2:1) is required to give densely packed siloxane film to form the silica coating by covalent bond formation (Si-O) around the SPIONs surface (**compound 8**).

During the reaction in the presence of a mixture of polar and non-polar solvents, the SPIONs gradually move from the hexane solvent to the water layer which reflects the successful progress of the ligand exchange reaction. The process takes about 72 h to reach completion. The TEM image shows that the SPIONs have a spherical shape, see Figure 19. The NTA analysis showed much bigger SPIONs present in the solution than expected with a mode diameter of 62 nm and mean diameter of 88 nm. This could be due to the high ratio of siloxane used for coating. Hence, there are clearly some issues with aggregation when this method is applied and further optimisation is required. The ICP-OES analysis detected higher mass percentage of silicon than previously observed at 15.2%. This result is expected as higher silica ratio and lower iron concentration (4 ml/ 20 mg) used in this reaction compared to the previous reaction (0.5 ml/ 300 mg).

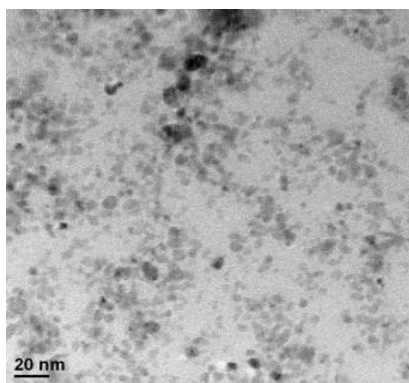


Figure 19: TEM image of NPs coated with a silica layer using the ligand exchange method

2.5. Conclusion

Using SPIONs for biomedical applications has attracted enormous attention, especially in the formation of multifunctional MRI contrast agents for cancer targeting applications. In the work reported in this chapter, SPIONs were fabricated using two different approaches, co-precipitation and thermal decomposition. The two approaches were compared to find out the best method to prepare SPIONs for further research use in this work. An attempt to control the SPIONs size and size distribution, and dispersibility, by changing the base addition speed in the co-precipitation method was not reproducible. This parameter has previously been shown to have a moderate effect on SPIONs sizes, whereas in the thermal decomposition method varying the heating rate provides more precise control of SPIONs sizes with more highly monodisperse SPIONs. The co-precipitation method was selected for further use as the nanoparticles could be separated from larger particulates using syringe filters and it was easier to produce larger amounts of material.

The synthesized SPIONs were coated with a silica shell for effective suspension in aqueous media, biocompatibility and the capability to functionalize the surface. Two silica coating mechanisms were used, firstly, silica was directly formed on the ‘naked’ SPIONs surface, and secondly, the silica shell was formed by displacing a surfactant layer around the SPIONs using a ligand exchange mechanism. The two coating strategies were analyzed and compared, with the formation of the coating onto the ‘naked’ surface giving the most useful results.

The nanoparticle size, size distribution, stable suspension concentration and surface composition are important for the applications investigated in the subsequent research that was carried out. One of the key aspects is the ability to control the functional groups present on the coated surface to adapt the particles as multimodal imaging agents.

Chapter 3

^{68}Ga radiolabelled iron oxide nanoparticles for *in vivo* multimodal imaging

3.1 Aims and background

Nanoparticles with spherical shapes have been designed for research and modified for multimodal imaging purposes, and the progress on this research is summarised in a recent review article.¹¹⁴ Examples includes quantum dots loaded with ^{64}Cu for cancer angiogenesis imaging¹¹⁵, and iron oxide nanoparticles labelled with ^{64}Cu for visualisation of tumours.¹¹⁶

The main aim of the work reported in this chapter is to create functionalised iron oxide nanorods (NRDs) for use in multimodal imaging (MRI/PET) applications *in vivo*. The significant advance of the performed work is in using iron oxide nanorods (NRDs) which have advantages over the commonly used spherical NPs. As described previously, using NRDs has the advantage of giving higher R_2/R_1 relaxivity in MRI imaging experiments and potentially offers a higher radiolabelling capacity due to the higher surface area. There has been no report on using nanorod like structures for multimodal imaging applications, with previous work by other groups focussing on spherical particles.

In this chapter, an overview is given of the field of using nanomaterials for radiolabelling including labelling methods, materials, chelators and suitable isotopes, see section 3.2. This is followed by discussion of the reaction between tert-BuDO3A and a siloxane derivative to prepare the starting material for coating and subsequent radiolabelling of NPs, see section 3.4. The prepared siloxane-macrocyclic derivative was used to form three types of NRDs with various ratios of siloxane-PEG, see section 3.5. The coating reactions were carried out using the previously synthesised NRDs, see section 2.3.4, using the direct attachment method with mixtures of siloxane-macrocyclics and siloxane-PEG to form a silica shell around the NRDs, see section 3.5.1. The different coated constructs were fully characterised and studied with a range of analytical techniques to investigate the coating efficiency, sizes, surface charges and stabilities in physiological media, see section 3.5. For studying the applicability of the designed constructs to be utilized for multimodal imaging (MRI/PET), a series of experiments were carried out. The PET radiolabelling efficiency of the coated NRD constructs with the gallium-68 isotope was investigated, see section 3.5.2.5. MRI contrast properties were characterised under weighted T_1 and T_2 measurements to calculate the R_2/R_1 relaxivity, see section 3.5.2.6. A series of comparisons between coatings materials was carried out to select the best candidate for *in vivo* multimodal imaging (MRI/PET) see section 3.6.

Before conducting *in vivo* multimodal imaging (MRI/PET), the radiochemical stability was analysed since PET is tracing the radionuclide localisation it must be attached to the nanoparticle to provide biodistribution information. For this goal, studies using competitive chelators and proteins (such as EDTA and serum proteins) to measure the labelled NRD constructs stability were carried out, see section 3.7.2. *In vivo* imaging biodistribution (MRI/PET) and *in vivo* stability studies were then performed, see section 3.7.3.

3.2 Introduction

3.2.1. Positron emission tomography (PET) imaging using radiolabeled iron oxide nanomaterials

For clinical and preclinical applications, PET is an excellent diagnostic tool for monitoring the concentration and distribution of radionuclide labelled imaging probes.¹¹⁷

Using nanotechnology for imaging purposes holds great potential to diagnose and treat many diseases including cancer. NPs offer a high surface area for modification with a wide range of molecules such as targeting vectors, multimodal imaging agents, agents for gene delivery and agents for drug delivery. The new approach of using radiolabelled iron oxide nanostructures as PET/MRI multimodal imaging probe is in its infancy and is generating exciting results in the molecular imaging field.

Although there has been rapid progress in radiolabelling NPs for imaging applications, many of the applications of nanoparticles have not moved beyond animal model, as questions remain before the application of such compounds to the human body. For example, the prolonged exposure of NPs to the body may generate long-term toxicity. Using the traditional techniques of monitoring NPs to understand the biological processes is challenging, however, PET imaging has the capability to track the NPs *in vivo* with non-invasive and quantitative analysis in order to analyse how they are processed.¹¹⁸

There are many critical properties of radiolabelled NPs, three aspects in particular must be carefully considered. Firstly, the design of the functionalized NPs, secondly, selecting a suitable isotope to match the properties of the targeted receptor or protein physiology, finally, determining the labelling approach for attaching the radioisotope onto the NPs surface. The radiolabelling approach should be efficient and not make any changes in the physical or chemical properties of the NPs during the labelling process.

3.2.2. Nanoparticle radiolabelling methodologies

Generally, radiolabelling methods can be classified into four different labelling techniques (see Figure 20):

1. Coordination chemistry which is based on radioisotope/chelator complexes forming on the NPs surface.
2. Direct activation of the NP materials to form radioisotopes using the nanoparticles as the accelerator target.
3. Addition of a radioactive precursor during the NP synthesis process.
4. Chelator-free post-synthetic radiolabelling.

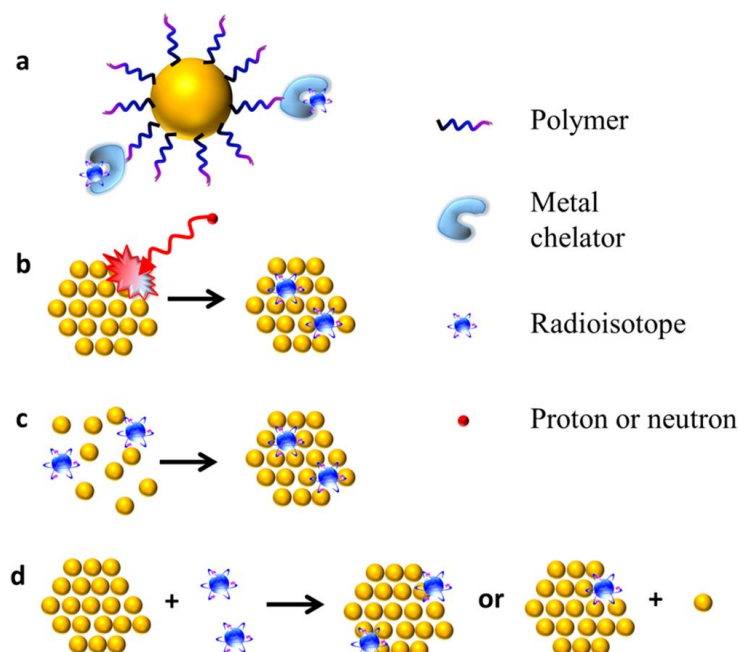


Figure 20: Four approaches for radiolabelling NPs. This Figure is reproduced from a review by Sun et al.²⁷

Anchoring chelating ligands on the NPs surface to coordinate radiometals (Figure 20a) is a convenient method. Two main issues are; firstly the efficiency of NPs surface functionalization can affect the outcome; secondly the nature of the radiometal/chelator complex must offer suitable properties.²⁸ It is critical to form a stable complex between the chelator and radiometal to reduce the transchelation of the radiometal.

Direct radioisotope formation by bombarding the NPs using neutrons or protons to form radiolabelled NPs is possible but highly dependent on the NP material and inconvenient due to the requirement for a particle accelerator.¹¹⁹ Another approach for incorporating radioisotopes inside the NPs is to add radioactive precursors during the NPs synthesis in order to form intrinsically radioactive NPs, see Figure 20c. In this case, the radioisotopes are inside the crystal lattice of NPs hence will be highly stable. However, the time required to synthesise the particles and the handling required are inconvenient and much of the radioactivity will have decayed.

Radiolabelling NPs in the absence of chelators (chelator-free post synthetic radiolabelling) is an interesting method that has been developed recently, see Figure 20d. This method combines the properties of chemical and physical interactions between the NPs and the radioisotopes with a minimal effect of the NPs properties. However, stability must be carefully evaluated.

3.2.3 Nanoparticles and radiolabelled materials used for multimodal (MRI/PET) imaging

To select an appropriate isotope to attach onto the NP surface, four parameters should be taken into consideration:

1. Isotope decay half life.
2. Reliability of radiolabelling methodology.
3. Availability of isotopes
4. Isotope imaging characteristics.

Selecting a suitable isotope half-life is important for targeted applications. For example, ^{64}Cu (12.7h), ^{18}F (109.8 min) and ^{68}Ga (67.7 min) have a wide range of half-lives. The half-life must be long enough for transportation (if required), radiolabelling and match the vector half-life to allow it to reach the site of interest *in vivo*. On the other hand, the isotopes must have as short half-life as possible in order to reduce unnecessary radiation exposure for the patient.

3.2.4. Gallium-68 isotope for PET imaging

Gallium-68 has great potential in novel radiopharmaceuticals for PET imaging purposes. It has a half-life of 68 min and decay that is mainly by positron emission (β^+ 89%, $E_{\beta^+ \text{max}} = 1899 \text{ keV}$).

Recently, ^{68}Ga has attracted major interest due to its accessibility from a $^{68}\text{Ge}/^{68}\text{Ga}$ generator system which was developed to produce high yields of the ^{68}Ga isotope for radiopharmaceutical applications at a clinical site with no need for a cyclotron. The parent isotope ^{68}Ge has a half-life of 270 days to decay to ^{68}Ga and so the generator can last up to a year.

A new generation of $^{68}\text{Ge}/^{68}\text{Ga}$ generators has recently become commercially available which are able to produce high yielding and reproducible ^{68}Ga complexes with DOTA derivative peptides for clinical usage. The $^{68}\text{Ge}/^{68}\text{Ga}$ generator elutes cationic ^{68}Ga with dilute acid (0.1 M HCl). The reliability and availability of the new ^{68}Ga generator system offers efficient purification, high yield and fast production. ^{68}Ga is potentially becoming a useful isotope for PET imaging to rival ^{18}F (and compete with $^{99\text{Tc}}$ SPECT imaging).

In this chapter, ^{68}Ga was the selected radioisotope for study due to favourable properties and the availability of a ^{68}Ga generator in the preclinical PET Research Centre at the University of Hull. There is high potential for translation of gallium-68 labelling protocols to a clinical environment.²⁹

3.2.5. Gallium chelators

It is essential to be able to efficiently radiolabel biomolecules. The radiometal should be coordinated with a bifunctional chelator (BFCs) which offers high stability under physiological conditions and a further functional group for covalently binding to a targeting vector. In this work BFCs will be used to attach the radiometal to the NPs rather than directly to a biotargeting vector. The selection of BFC is dictated by several factors such as the choice of radiometal and its oxidation state.

Five general BFCs requirements:

1. Selectivity: The BFC must bind to the radiometal of interest selectively to avoid low specific activities.
2. Rapid complexation kinetics: The coordination process between radiometal and the BFC must occur in a short time under ambient conditions allowing sufficient time for the radiometal to achieve biological targeting after administration.

3. Stability/inertness: The BFC complex must be thermodynamically stable and a kinetically inert complex to avoid any potential hydrolysis or ligand exchange reactions during the *in vivo* targeting process.
4. Accessibility: The reaction of BFC and radionuclide must be cost effective, straightforward and provide a high yield of the final product.
5. Versatile conjugation chemistry: BFC should allow optimum flexibility to maintain the overall polarity on conjugation to minimally disrupt pharmacokinetics. Accordingly, various chelating agents with different structures, selectivity and stability are available.^{30, 120}

Currently, the designed chelators for gallium(III) labelling are mostly focused on ligands based on cyclen (1,4,7,10-tetraazacyclododecane) and cyclam (1,4,8,11-tetraazacyclotetradecane) structures. Macrocyclic ligand derivatives provide an increased stability over acyclic chelators, although recent advances show new highly effective acyclic chelators. Hence, macrocyclic derivatives are better able to retain the radiometal and prevent transchelation. Ga(III) has six coordination sites, generally forming an octahedral geometry therefore, additional donor groups in the form of side arms linked to the macrocyclic structure are essential to saturate all of the gallium coordination sites.¹²¹

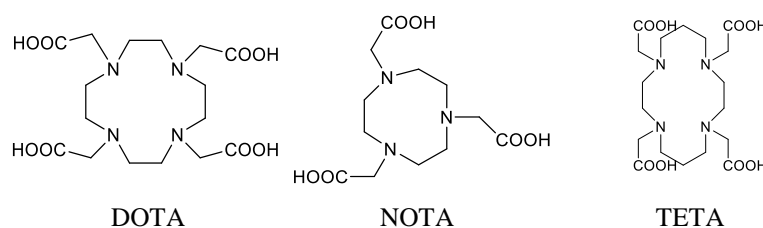


Figure 21: Various ⁶⁸Ga chelators used for *in vivo* applications.

DOTA (1,4,7,10-tetraazacyclododecane-1,4,7,10-tetraacetic acid), which is shown in Figure 21 is able to complex the ⁶⁸Ga with a coordination number of six. In addition, the Ga(DOTA) complex shows higher stability constant than Ga(transferrin) complex which means it has favourable properties for *in vivo* studies.¹²² The gallium(DOTA) coordination is based on encapsulating the metal with a N₄O₂ donor set of the cyclen Ns and two carboxylate groups in an octahedral geometry.¹²³ The two remaining carboxylate groups don't coordinate to the gallium ion.¹²³ Therefore, the overall charge of Ga(DOTA) complex is negative under *in vivo* conditions.

Another useful ligand for gallium complexes is NOTA (1,4,7-triazacyclononane-1,4,7-triacetic acid), shown in Figure 21b. This ligand has efficient gallium complex formation at R.T and high stability under physiological conditions.¹²⁴ In addition, the NOTA ligand has a smaller cavity size than DOTA, hence it displays a higher stability and selectivity toward gallium(III). The Ga-NOTA complex has an overall neutral charge under *in vivo* conditions.¹²⁵

In this section ⁶⁸Ga complexes with DOTA are used for radiolabelling and *in vivo* studies. The DOTA ligand was selected due to the potential for it to be functionalized for

nanoparticle surface attachment and it shows a high stability metal coordination with a relatively easy synthesis procedure. In addition, DOTA derivatives can be produced in a higher yield than related NOTA ligands. The DO3A chelator was synthesised by Mustafa Al-Yassiry and supplied for this work.

3.2.6. Radiolabelled NRDs for *in vivo* biodistribution studies

Studying the biodistribution of the nanomaterials provides important information about the fate of the NPs and if they reach the targeted sites and tissues, such as cancer cells. Biodistribution studies have been carried out using luminescent or fluorescent imaging techniques in mice. These approaches are generally more effective for *in vitro* and *ex vivo* monitoring due to poor tissue depth for imaging.

However, for improved *in vivo* imaging with high sensitivity, good tissue penetration, and quantification, radiolabelled nanomaterials are the most appropriate imaging agents for use in small animals. A cancer targeting moiety can be attached onto the nanomaterial surface to direct the NPs. ^{68}Ga has sufficient half life for localization of the nanoparticles *in vivo*.

Jarrett et al. designed dual-modal PET/MRI active probes consisting of iron oxide NPs coated with a dextran layer. The functionalized NPs were loaded with DOTA chelators before being radiolabeled with $^{64}\text{Cu}^{2+}$ and also labelled with Gd^{3+} . The group faced some problems when they loaded the DOTA onto the NPs surface. They observed that radiolabelling did not occur efficiently, alternatively, they complexed the metal with the DOTA chelators before loading them onto the NPs surface. In this case radiolabelling was effective but with a low radiolabelling yield of 21%.¹²⁶

Tu et al. performed labelling with a similar system but they used silica coated quantum dots (Si-QDs). The silica-QDs were loaded with DOTA then the ^{64}Cu was coordinated with DOTA in a second step. The radiochemistry shows an excellent radiolabelling yield of 100% with no loss under a ligand competition reaction with EDTA after 48 h. The *in vivo* study in mice shows that some of the QDs were extracted quickly via renal filtration and the rest accumulated in the liver.¹²⁷

In another study carried out by Stelter et al., they synthesized iron oxide nanoparticles coated with commercially available siloxane derivatives with amino terminal group ($-\text{NH}_2$). The study investigated the efficiency of ^{68}Ga coordination over the NPs surface exploiting the amino terminal group. The radiolabelling stability of this system was tested in competition with diethylenetriaminepentaacetic acid (DTPA). High radiolabelling stability was found at 92% after 24 h incubation. The *in vivo* biodistribution results showed that NPs accumulated in the spleen and liver 1 h after injection.¹²⁸

The designed system in this work consists of iron oxide nanorods (NRDs) and the silica coating was performed using commercially available siloxy-PEG and synthesised siloxy-tBuDO3A. The gallium-68 coordination was evaluated and an *in vivo* biodistribution study carried out.

3.2.7 Characterisation techniques

3.2.7.1 Zeta-potential analysis

In addition to previously described analytical techniques, the colloidal stability of prepared NPs was analysed using zeta potential measurements. Generally, NPs are stabilized by two dispersion mechanisms, electrostatic repulsion and steric repulsion. Electrostatic repulsion is based on NPs surface charge (higher charge magnitude, more stable NPS). Steric repulsion is caused by attaching ligands onto the NPs surface which prevent close contacts between the NPs.

NPs attraction and repulsion forces are dictated by the surface charges in addition to the pH (dissociated H^+ and OH^- ions). The results of zeta potential are completed by calculating the NPs velocity during electrophoresis using the Henry equation:

$$U_E = 2\epsilon\zeta F (ka)/3\eta$$

Where: Electrophoretic mobility U_E , Zeta potential ζ , viscosity $F(ka)$ and dielectric constant η .

If the zeta potential result is higher than +30 or lower than -30 mV, this means that the NPs will be stable in suspension.

3.2.7.2. Other analytical techniques

Fourier transform infrared spectroscopy (FTIR), mass spectrometry and NMR spectroscopy were used to characterise the precursors. FTIR and elemental analysis are also useful to confirm the presence of the coatings on the NPs. Radio-TLC was used to analyse the labelled NRDs and other gallium-68 containing molecules. Competition stability against EDTA and transferrin was used to determine radiolabelling stability. Transferrin is an iron binding protein present in the blood plasma that is the most effective *in vivo* protein for binding to gallium.

3.3. Aims

The main aim of the work in this chapter is to produce iron oxide nanorods (NRDs) to be used as multimodal imaging contrast agents (MRI/PET). An appropriate combination of characterisation techniques was selected and used to evaluate the product from each stage.

The strategy was to use the already synthesized nanorods (NRDs) that are described in chapter 2 to be silica coated and macrocycle functionalized in a one pot reaction following the direct attachment strategy.

Firstly, the organic synthesis reaction to produce the siloxane macrocycle was carried out and the second stage is coating the NRDs with the synthesised molecules (siloxane-tBuDO3A) along with stabilising group (siloxane-PEG) in different ratios. Characterisation studies were carried out to evaluate the NRDs coating efficiency, sizes, charge, elements present, shape, pH stability, salt stability, relaxivity and ^{68}Ga isotope loading stability. The last stage is examining the NRDs under physiological conditions in order to ensure that the

samples are stable enough to be progressed for *in vivo* applications. Finally, an *in vivo* biodistribution study for multimodal imaging (MRI/PET) was carried out.

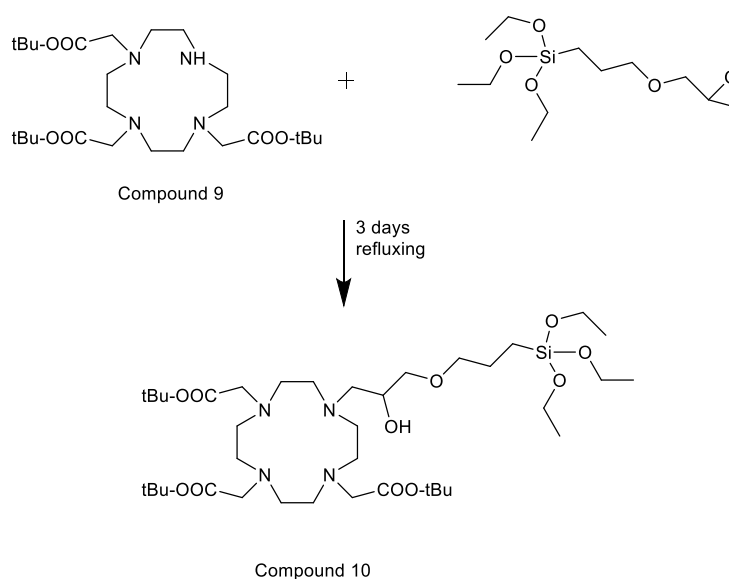
3.4 Synthetic Methodology to Form Functionalised DO3A Derivatives

3.4.1 Chemical synthesis of Si-DO3A

There are numerous macrocyclic chelators that function as gallium(III) ligands including DOTA, TACN, NOTA and TETA. Among them the cyclen derivatives such as DOTA offer high stability and ^{68}Ga transchelation *in vivo* is minimized.¹²² In this work, a secondary amine group on the cyclen is reacted with a siloxane derivative.¹²³

This proceeded via an epoxide ring opening reaction to link tBu-DO3A (**compound 9**) with a commercially available siloxane derivative to form **compound 10**, see Scheme 1. Initially the DOTA type compound was protected by converting the three carboxylic terminal groups into esters (tBu-DO3A, **compound 9**). Therefore, the epoxide is forced to react with the secondary amine site on the cyclen, see scheme 1. 1,4,7-tris(tert-butoxycarbonylmethyl)-1,4,7,10-tetraazacyclododecane (tBu-DO3A, **compound 9**), was supplied by Mustafa Al-Yassiri to be used as starting material for these reactions.

A similar methodology to that reported by Barreto et al.,¹¹¹ was adapted for this work. A mixture in a 1:1 ratio of 1,4,7-tris(tert-butoxycarbonylmethyl)-1,4,7,10-tetraazacyclododecane (tBu-DO3A, **compound 9**) starting material and (3-glycidyloxypropyl) triethoxysilane (GPTES) was dissolved in chloroform and stirred for 3 days under reflux. The desired compound was purified by chromatography and washed with ethanol and water to give **compound 10**. ^1H NMR shows the expected signals and the mass spectrum contains a large molecular ion peak at 793 with no sign of starting material. This method provided high yield of >90% which is comparable with the literature method reported by Barreto et al.¹¹¹ Due to the sensitivity of the product to the air, the sample must be stored under Ar and in the freezer until used.



Scheme 1: Reaction of tert-BuDO3A and GPTES under reflux for 3 days.

3.5 NRDs coating and characterization

3.5.1 Coating iron oxide nanorods (NRDs) with siloxane functionalized DO3A and PEG derivatives using the direct attachment strategy

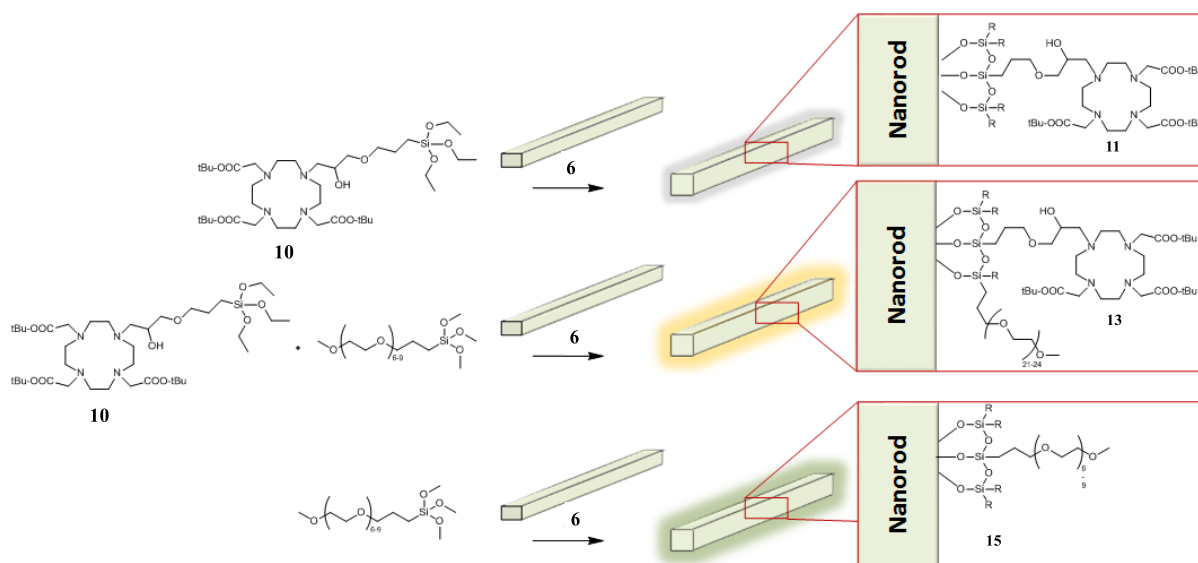
It has been demonstrated that to design stable NRDs across different physiological conditions, the NRDs surface functionality is the key factor. Based on the fact that the NRDs suspension could be highly unstable once injected *in vivo* due to the fact that the columbic repulsion forces generated from ionic charges are diminished at elevated salt concentration, which can lead to rapid NRD aggregation (the human body physiological salt concentration is about 100 mM). Therefore, investigation of stability across an ionic strength range is very important for biomedical applications.

The addition of steric stabilization may also work to prevent NRDs aggregation under a wider range of physiological conditions. Polymers are suitable materials to use biomedical nanotechnology applications. Polymers are able to form a substantial barrier around each NRDs preventing them from getting in contact with each other using steric force repulsion.¹²⁹ The most commonly used polymers in aqueous media, are PEG and carbohydrate derivatives such as chitosan, dextran and starch. Among those polymers, PEG was selected as the most appropriate ligand for long term NRDs stability under blood circulation due to high stability at extremes of pH and high salt concentrations.¹³⁰

In this work, the addition of PEG derivatives was investigated by adding both siloxane-PEG and siloxane-macrocycle derivatives simultaneously to the NRDs suspension. The aim is to incorporate both molecules into a silica shell around the NRDs. This will coat the already created NRDs (see Chapter 2.8) with two different coating components, (siloxane-DO3A) a macrocyclic ligand and (siloxane-PEG) as a stabiliser. Three constructs were produced; see scheme 2.

- 1- NRDs coated solely with siloxane-tBuDO3A (**compound 11**),
- 2- NRDs coated with a mixture of siloxane-tBuDO3A and siloxane-PEG in a ratio of 1:1 (**compound 13**)
- 3- NRDs coated solely with siloxy-PEG (**compound 15**).

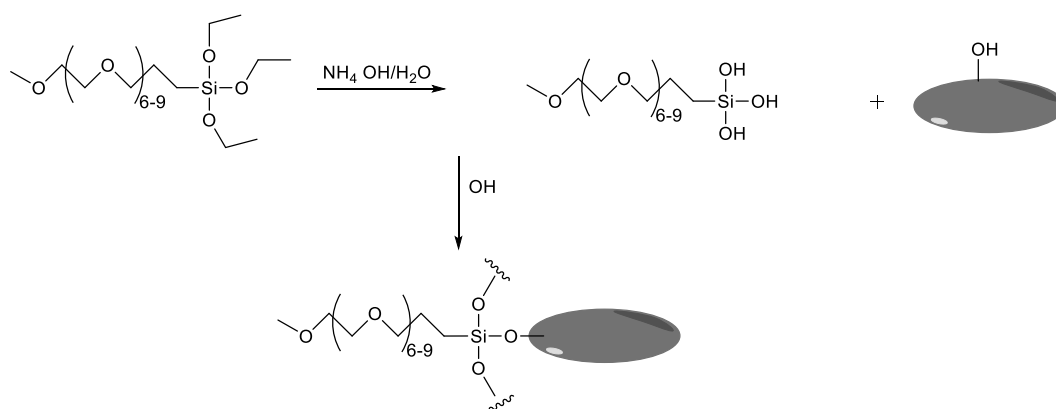
The coating on the NRDs surface was carried out using the direct attachment binding methodology see section 2.4.1. After coating, the NRDs were characterised with a variety of analytical techniques to investigate NRDs coating efficiency, sizes, charge, elements concentration, shape, pH stability, salt stability and relaxivity.



Scheme 2: Different ratios of precursors used in coating of iron oxide nanorods (NRDs). NRDs coated solely with tBuDO3A; NRDs coated with a mixture of siloxy-tBuDO3A and siloxy-PEG (1:1 ratio); and NRDs coated totally with siloxy-PEG.

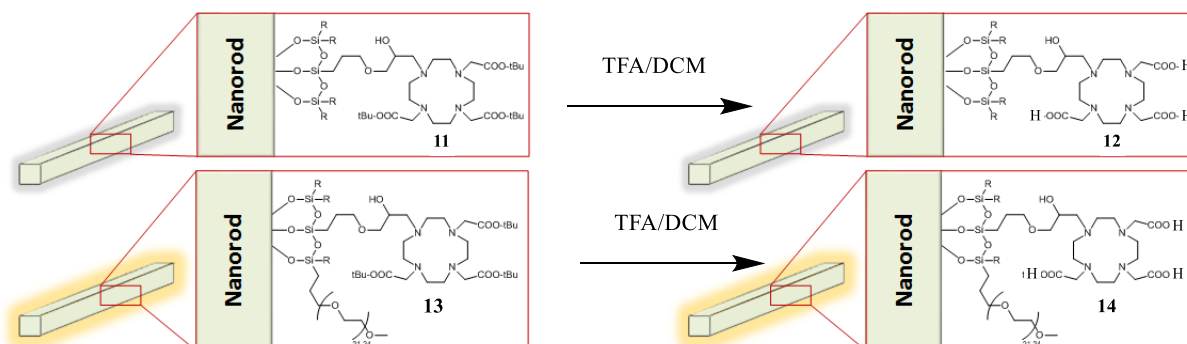
A range of three coated NRDs constructs were produced using varying quantities of PEG and macrocycles (see scheme 2). The coating reaction was adapted from reported work achieved by Barreto et al.¹¹¹ The coating reaction occurred under basic conditions over 48h stirring in a mixture of water and ethanol. The addition of aqueous ammonia was to maintain the pH at around 9 in order for the reaction to progress to give **compounds 11, 13 and 15**. During the hydrolysis part of the reaction, the ethoxy groups on the siloxanes were converted to hydroxyl (OH) groups under the influence of the basic solution (OH⁻). This is followed by a condensation reaction in order to connect the hydroxyl group on NRDs and siloxane releasing a water molecule, see Scheme 3.

After the coating reaction, the NRDs were washed in the same manner as previously described with a series of solvents and using a magnet for NRDs isolation, then the samples were dried. The next step was to subject **compounds 11 and 13** which contain macrocyclic components to a deprotection reactions to expose the carboxylate groups. This step was achieved using trifluoroacetic acid (TFA) in dichloromethane solvent to produce compounds **12 and 14**. 48 h is a sufficient time to perform the siloxane coating process. Using a different solvent ratio (H₂O/ethanol) has an effect on the hydrolysis and condensation, as less aqueous solvent slows down the hydrolysis reaction whereas less ethanol slows down the condensation reaction.



Scheme 3: Mechanism of the first step in silica shell layer formation on the iron oxide nanorods using the direct attachment method (hydrolysis and condensation reaction mechanisms).

The role of the protection groups on the macrocyclic side arms is to prevent unwanted side reactions. The cleavage of the tert-butyl esters group on the tBuDO3A to form carboxylic acids is required. This step was achieved using trifluoroacetic acid (TFA) in DCM solvent (2:1) stirring for 48h before washing the NRDs with a series of solvents as described previously to give compounds **12** and **14**. This step achieved via following the previously described literature methodology,¹³¹ see Scheme 4.



Scheme 4: Deprotection of tBuDO3A on the NRDs surface using TFA.

The deprotection reaction, rendered the NRDs more aqueous compatible as the carboxylic terminal group is water soluble and also opens up the possibility for metal ion coordination on the NRDs surface via the macrocyclic chelators.

3.5.2 Coated NRDs characterisation

3.5.2.1 NRDs iron concentration study

To investigate the effect of the macrocyclic chelator charges on the NRDs stability, the colloidal stability of tBuDO3A-NRDs (**compound 11**) was tested against bare NRDs. The comparison was achieved by suspending **compound 11** and bare NRDs (**compound 7**) at various iron concentrations and observing the speed of colloidal precipitation at the bottom of vials. Iron concentrations of 0.25, 0.5, 1, 2.5, 5, 7.5, 10 and 50 mM were loaded into empty

vials for **compound 11** and **compound 7**. All the samples were suspended in H₂O with extensive sonication until all of the NRDs were fully suspended.

Theoretically, once the bare and coated NRDs are suspended in the H₂O, the pH is expected to be reduced depending on the iron concentration, a higher iron concentration will generally provide a more acidic medium. The measured pH after suspending NRDs ranged between 2.9 and 4.2.

After suspending the samples at eight different concentrations, all of the bare NRDs samples were completely precipitated after 24 h, see Figure 22a. It was expected to have poor stability but it was anticipated that suspensions would be stable for longer than 2 days. The bare NRDs were suspended well during the first 6 h but gradually precipitated up to 24 h. There are only weak positive charges generated from the iron oxide surface, hence the net charge force is unable to separate the NRDs and prevent them from forming aggregated NRDs and accelerating the precipitation process. The macrocycle coated NRDs (**compound 11**) show much better suspension stability in the H₂O, see Figure 22 b. This was expected due to the deprotonated acid arms combined with the protonated ring nitrogen leading to better stability in aqueous solvent. Lower concentrations showed higher stability from precipitation as expected.



Figure 22 (a) Bare NRDs (Compound 7) after 24 hours

Figure 22 (b) Compound 15 after 2 weeks

At higher iron concentration, more NRD aggregation was observed; this is expected as the probability of NPs collisions increases with square ratio of concentration.¹³² Magnetic dipolar force is directly related to NPs concentration.¹³³ The effect of magnetic moment on NPs aggregation increases significantly at high particle concentration as the magnetic force exceeds the electrostatic charge stabilisation by raising the residual magnetisation force which leads to alignment of the magnetic dipoles of close NPs forming chains. At this point, the electrostatic repulsion is at maximum; whereas, the NPs orient their magnetic dipoles in order to facilitate the total attraction force.¹³⁴ Then, the magnetic dipole force becomes dominant cause of NP aggregation. Magnetic dipole force is dependent on the distance between the NPs centres.¹³⁵

Converting the macrocycle ester groups into carboxylic acids (COOH) on the NRDs surface is expected to increase the NRDs suspension stability. The NRD compounds before and after deprotection (**compounds 11** and **12**) were suspended in eight vials and the vials were pictured 2 days after sonication in order to form suspensions, see Figure 23a and b. There are no obvious differences in stability of compounds **11** and **12** which may indicate that either there is no effect of deprotection reaction on the NRDs solubility or possibly that they have partially deprotected under the sonication process.



Figure 23(a) Iron concentration test of Compound 11 (b) Iron concentration test of Compound 12

3.5.2.2 NRDs coating efficiency characterisation

Generally, it is challenging to perform precise analysis on how well coated the NRDs are as traditional analytical methods such as MS and NMR analysis are not useful for such measurements. Therefore, a combination of CHN, ICP-OES and FTIR was used to investigate the coating.

It is anticipated that an increase in carbon, hydrogen and nitrogen percentages would correlate with an increased amount of DO3A on the NRDs surface. The percentage of iron and silicon are expected to be similar for all of the samples as fixed concentrations were used for analysis.

For elemental analysis see Figure 24:

1. NRDs coated solely with DO3A (**compound 12**)
2. NRDs coated with DO3A and PEG 1:1 ratio (**compound 14**).
3. NRDs coated solely with PEG (**compound 15**).

For elemental analysis, ICP-OES analysis was used with a fixed sample mass (1 mg) from all samples. The samples were suspended in 5 ml H₂O, and then the suspensions were diluted to a dilution factor of 10 ppm in purified water and were shaken vigorously. The samples were taken to dryness, then dissolved in nitric acid (3 ml) and HF (1 ml) in a Teflon tube (sealed and heated to 200°C under microwave radiation for 15 minutes). The samples were cooled down, boric acid (5 ml) was added to react with any excess HF, then the samples were reheated again to 170°C, diluted after cooling and analysed with ICP-OES.

The results followed the expected trends; see Figure 24, a significant increase in carbon and nitrogen correlated with increased macrocycle component coating.

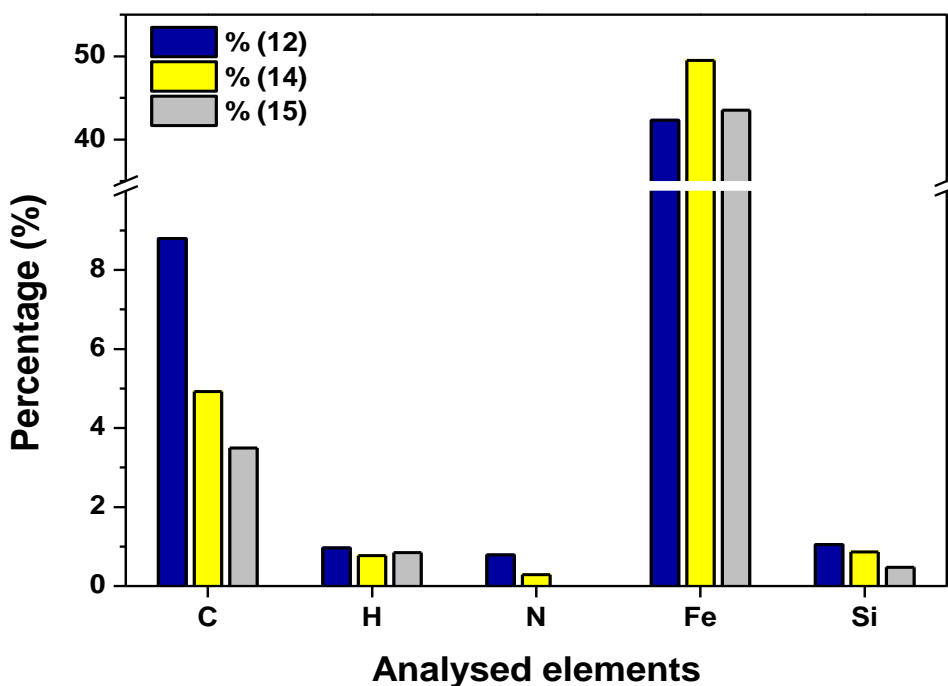


Figure 24: Elemental analysis of the coated NRDs using ICP-OES and CHN to determine the percentage of C, H, N, Fe and Si in each sample. . Three samples were analysed, NRDs coated solely with DO3A (**compound 12**), NRDs coated with a mixture of DO3A and PEG (1:1 ratio, **compound 14**) and NRDs coated totally with PEG (**compound 15**)

Nitrogen percentages show that, for an increased amount of DO3A precursor added to the coating mixture, a higher amount of nitrogen was present. For (NRDs-SiO-PEG, **compound 15**), which does not contain any nitrogen in the molecular structure of the coating, no nitrogen content was observed. The highest nitrogen percentage is observed for **compound 12** which reflects the higher amount of tBuDO3A precursor added compared to the other nano-constructs. Iron percentages are expected to be similar for all constructs. The elemental analysis show that iron percentage ranges between 44% and 49% which is appropriate for the application (over 40% is generally required to give satisfactory MRI relaxivity). This also indicates that the particles were successfully digested to give accurate ICP-OES results. The silicon percentage was again consistent with the proposed construct structures. A lower amount of silicon with an increase in the PEG component as the mass percentage of silicon is lower in siloxane PEG than the siloxane DO3A derivative. It was also demonstrated that there was no silicon present in the ‘bare’ NPs. The CHN and ICP-OES percentage of C, H, N and Si after coating are similar to those observed in the study carried out by Baretto et al.¹¹¹, in which NRDs were coated with various siloxy macrocyclic derivatives. The control sample of bare NRDs results shows the presence of iron (48.9%) and no carbon, hydrogen or nitrogen (within error).

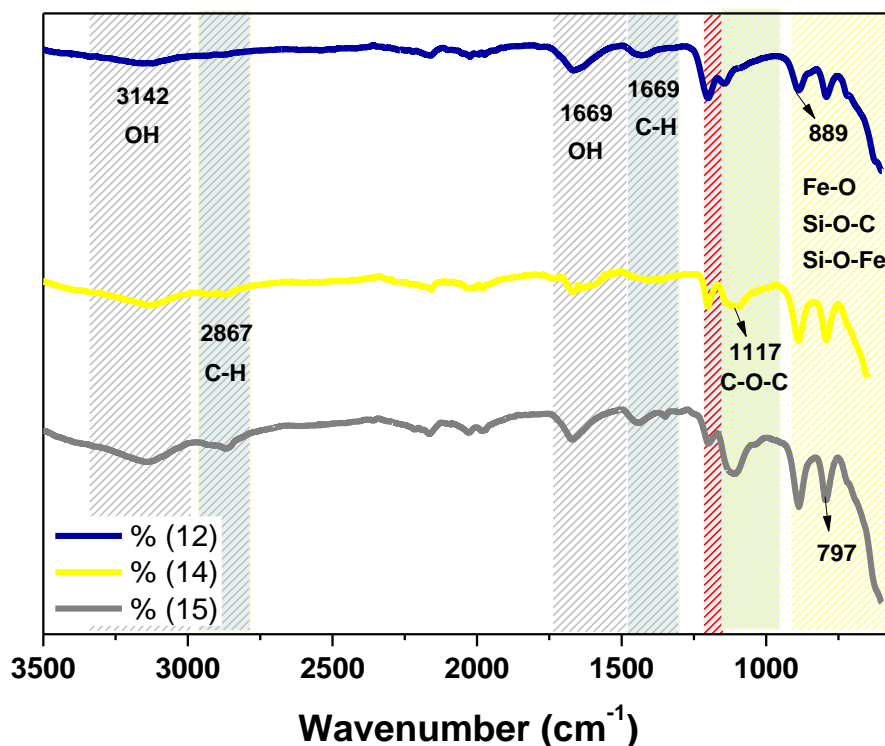


Figure 25: FTIR results of coated NRDs with DO3A (**compound 12**), NRDs-DO3A and PEG 1:1 ratio (**compound 14**) and NRDs-PEG (**compound 15**).

To study the surface functionalities on the surface of NRDs, Fourier transform infrared (FTIR) spectroscopy analysis was employed. The IR spectra are shown in Figure 25, with a strong peak present at 600 cm^{-1} which correlates to the iron Fe-O stretching frequency. For all compounds analysed (**12**, **14** and **15**) the other peaks between 600 and 990 cm^{-1} indicate the presence of the silica coating on NRDs surfaces as they can be attributed to Si-O-C and Si-O-Fe respectively.^{113, 136} For compounds **14** and **15**, peaks are present at 2867 and 1117 cm^{-1} which can be assigned to C-H and C-O-C stretching frequencies respectively that are part of the PEG chain.¹¹³ It was observed that, an increased ratio of PEG gave higher intensity peaks intensity at 2867 and 1117 cm^{-1} . There is a strong peak in compounds **12** and **14** at 1201 cm^{-1} which could be attributed to the C-N stretching frequency of the macrocyclic structure (see Figure 25), although a weaker peak is also present at this frequency for **compound 15** that has no macrocycle present. For **compound 14**, that incorporates a mixture of macrocycle and PEG, a broad peak in the region of 1117 cm^{-1} was observed which indicated the presence of C-O-C stretching. There are intense peaks at 3142 and 2669 cm^{-1} which are attributed to OH groups (indicating the presence of water) and C-H respectively.¹¹³

3.5.2.3 NRDs size and size distribution characterization

This section discusses the coated NRDs size, shape and size distribution and aims to detect any aggregation present in the samples. The size is crucial for biological applications, if the particle sizes exceed $2\text{ }\mu\text{m}$, there is potential for them to be targeted by the immune system and for the particles to be removed from the blood. In addition, large particles can be

removed from the system by the liver or spleen. However, particle sizes less than 300 nm are acceptable for biological *in vivo* applications. The aim is to measure the NRDs sizes and size distribution in order to confirm that they are suitable for *in vivo* applications.^{137, 138}

A combination of techniques was used to confirm the NRDs shape, mode size and average size. TEM (Transmission electron microscopy) and NTA provide an overview of sample size and shape. TEM was carried out to investigate the effect of the coating methodology on NRDs core shape and size. TEM results, see Figure 26, show that the shape of all constructs are similar (nanorods with length varying between 50 nm to 120 nm with width between 5 nm to 12 nm). This shows that the coating reaction only has minor effects on the NRDs shape and size distribution.

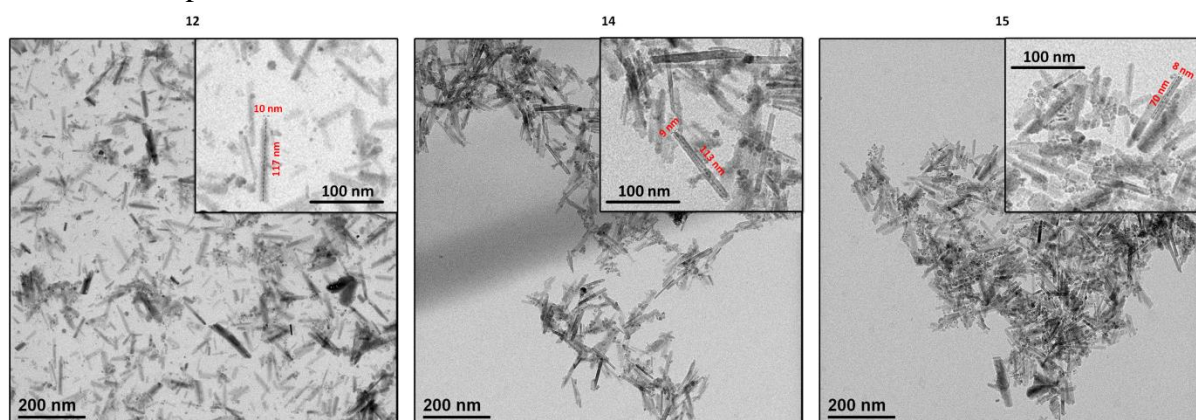


Figure 26: TEM images of coated NRDs. NRDs coated solely with DO3A (**compound 12**), NRDs coated with a mixture of DO3A and PEG in a 1:1 ratio (**compound 14**) and NRDs coated solely with PEG (**compound 15**)

However, the TEM analysis does not reflect the hydrodynamic size and so NTA analysis was carried out. The NTA was used to analyse water suspension samples containing 0.1 mM iron concentration for compounds **12**, **14** and **15**. All the samples show generally similar mode sizes and a range of mean sizes for the constructs at 120 nm mode size with more aggregation related to the increasing macrocycle ratio with mean particle sizes in the range 100 nm to 155 nm, see Figure 27. This range of sizes is acceptable for *in vivo* studies and there was no sign of precipitation on the bottom of the vials after the samples had been standing for one week. Further investigation of the suspension stabilities for the different particles was carried out across pH and concentration ranges.

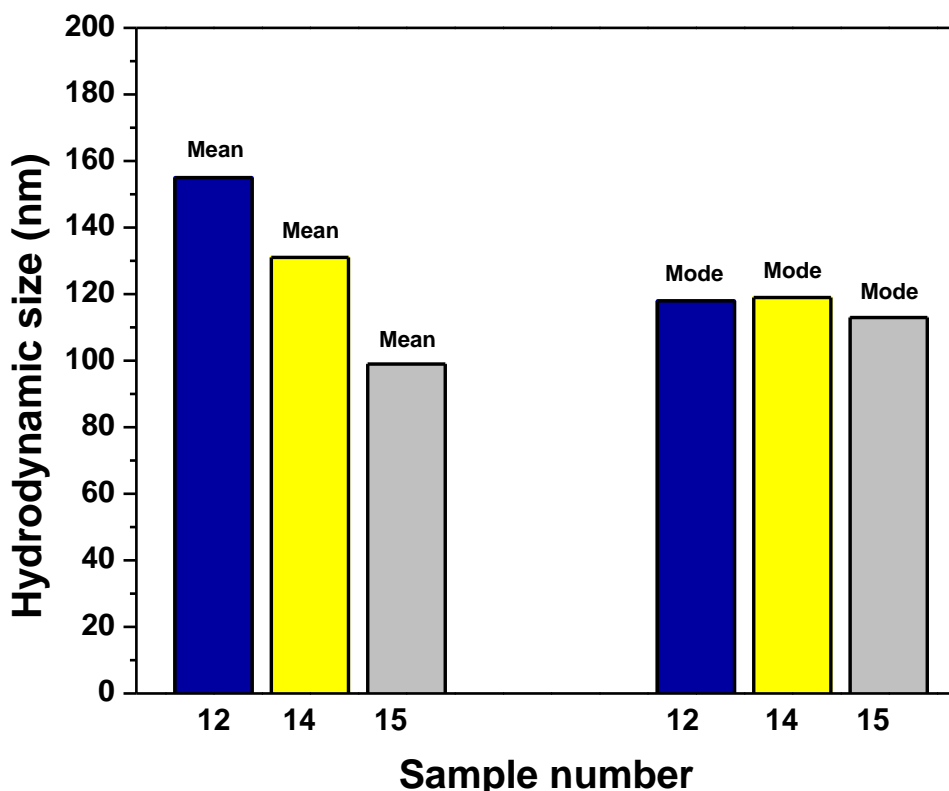


Figure 27: NTA analysis of coated NRDs to give NRDs size and hydrodynamic size distributions. NRDs coated solely with DO3A (**compound 12**), NRDs coated with a mixture of DO3A and PEG 1:1 ratio (**compound 14**) and NRDs coated solely with PEG (**compound 15**)

Compared with the bare NRDs, the NTA results show an increase in NRDs size from 22 nm in bare NRDs to 120 nm of coated NRDs. It is believed that this is due to the coating layer around the NRDs which may contribute in around 1 to 3 nm size increasing and most significantly an aggregation occurs due to cross linking nature of the coating layers and possible chemical interactions and bonds between the macrocycles molecules themselves (**sample 12**) and with PEG (**sample 14**) on the NPs surface. Although the PEG has low probability for such aggregation, looping (bending and folding) over the NPs surface still occurs which reduce the water diffusion and surface permeability which cause NPs aggregations. However, the observed mode and average particle size are suitable for *in vivo* applications.

3.5.2.4 NRDs stability in suspension

Measuring the NRDs stability under various physiological conditions is a critical step to predict the NRDs behaviour in biological systems. The NRDs surface charges play a crucial role in preventing the NRDs aggregation under physiological conditions. Hence, studying the NRDs surface charges is a necessary requirement before using the samples for an *in vivo* investigation. Zeta potential measures surface charges and either high positive or high

negative charges translate to a high electrostatic repulsion between NRDs which gives improved stability and less aggregation.

In this part of the research work, the aim was to measure the stability of all of the coated NRDs constructs produced in this work under various conditions. Firstly, the samples were characterized using zeta potential measurements at a fixed iron concentration of 7.5 mM at pH 7 in PBS, see Figure 28. Then a range of pHs and salt concentrations were used to monitor the NRDs aggregation. This analysis gave valuable information about the NRDs suspension stability before use for *in vivo* applications.

The study was carried out by firstly suspending the NRDs in aqueous solution, then the pH was adjusted using either 0.1M KOH or 0.1M HNO₃ with the pH monitored until the target pH was reached. All of the coated NRDs were negatively charged at pH 7.44. The samples displayed negative charges between -11 to -18 mV. As previously discussed the macrocycles present two potential sites for protonation/ de-protonation: the tertiary amines in the ring and the carboxylic acid groups. At higher pH, it is expected that the functionalized NRDs will be susceptible to precipitation when the NRDs isoelectric point is reached and the net charge is zero.¹³⁹

It can be seen that NRDs coated with a mixture of PEG and macrocycle in a 1:1 ratio, **compound 14**, have the largest surface charge of -17.70 ± 1.80 mV. The samples that are coated with 100% PEG, **compound 15**, showed reduced surface charge at -11.07 ± 0.15 mV and the NRDs coated solely with the macrocycle, **compound 12**, gave a similar value of -11.1 ± 0.3 mV. The 100% PEG coated NRDs were still observed to have high stability (no sign of precipitation after 2 months) which can be attributed to the steric interactions from the PEG groups as there are no ionisable species present in the coating functional groups. The mixed PEG/macrocycle coated NRDs (**compound 14**) have an ideal combination of steric contribution and charge at neutral pH to maintain suspension stability. The results from these experiments demonstrate that the particle suspensions are suitable for *in vivo* applications. The bare NRDs showed very low stability across all pH ranges from 1 to 6 and 8 to 11 with rapid precipitation with the highest stability at pH 7, where zeta potential showed a moderate charge of 1.8 mV.

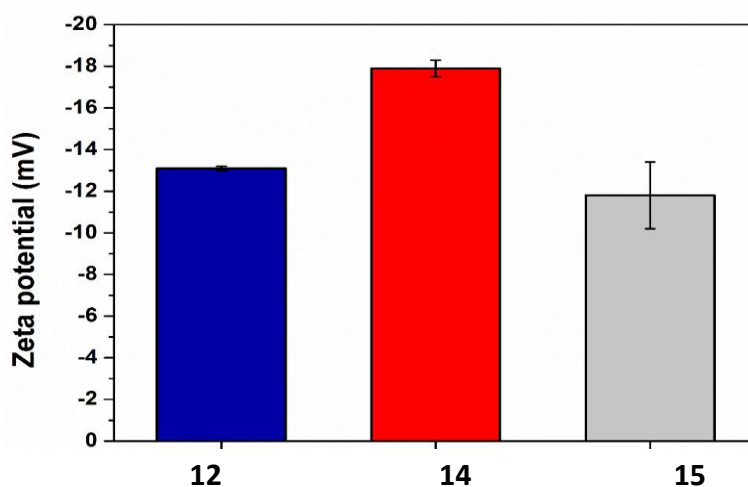


Figure 28: NRDs surface charge measurements using Zeta potential analysis. NRDs coated solely with DO3A (**compound 12**), NRDs coated with a mixture of DO3A and PEG 1:1 ratio (**compound 14**) and NRDs coated solely with PEG (**compound 15**)

Further measurements of the NRDs stability were carried out across a wider range of pH and ionic strength. Three samples of NRDs (**compounds 12, 14 and 15**) were maintained at fixed iron concentration 7.5 mM and suspended in H₂O under extensive sonication. For the pH stability test, the NRD suspensions were adjusted with a range of pHs from 1 to 11 using either 0.1 M NaOH or 0.1 M HCl, then the samples were left to stand for 10 h, see Figure 29. The NRDs coated solely with siloxane-macrocycle (**compound 12**) and the macrocycle/PEG mixture (**compound 14**) showed high stability under acidic and neutral pH values from ca. 1 to 8, whereas the NRDs coated solely with the PEG (**compound 15**) showed stability throughout the pH range tested from 1 to 11, see Figure 29. The results demonstrate that the PEG chains keep the NRDs apart using steric repulsion force that are not influenced by pH. It is also believed that surface hydrophilicity is plays an important role for the NRDs water stabilisation. PEG has previously been demonstrated to have these properties.¹⁴⁰

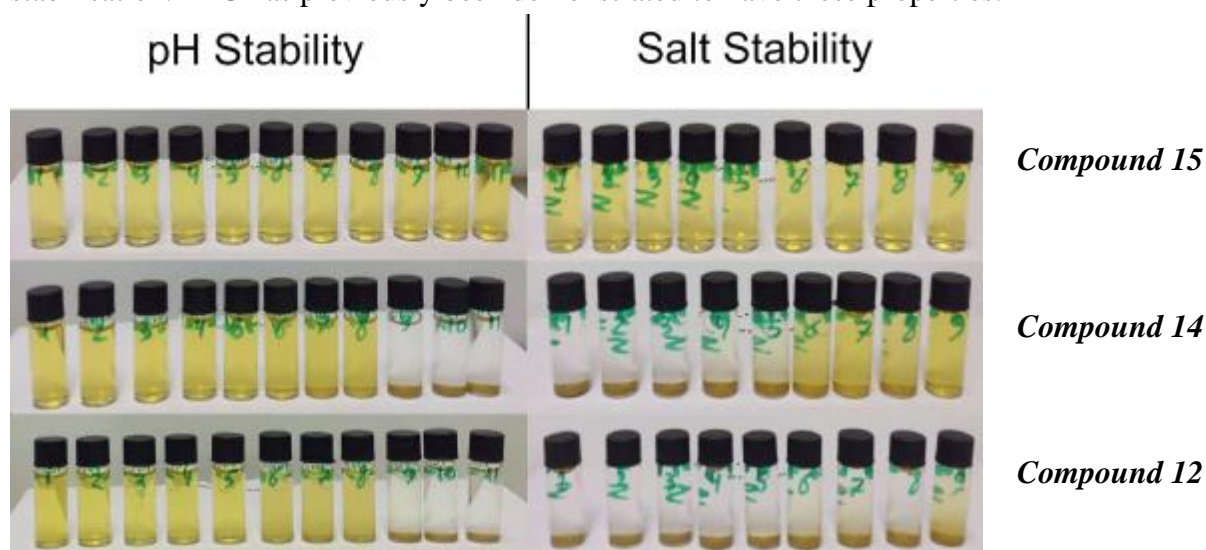


Figure 29: pH (1-11) and salt concentration (1-200 mOsm/L) for compound 15 (NRDs coated PEG), compound 14(NRDs coated macrocycles:PEG 1:1) and compound 12 (NRDs coated with macrocycles).

The NRDs stability was also assessed as a function of the ionic strength of the solution, the NRDs were suspended in solutions with a range of NaCl concentrations (0.001, 0.0025, 0.005, 0.0075, 0.01, 0.025, 0.05 and 0.075 M) and left to stand for 7 days, see Figure 29. It was observed that with an increased PEG percentage there is an increase in the NRDs stability, with the high salt concentration having an ionic strength value of 200 mol L⁻¹ (see Figure 29). A significant effect of NaCl on the electrical charge of macrocycles is generally caused by decreasing the electrostatic repulsion due to formation of a neutralising counter ion layer, therefore, NRDs aggregation can occur.^{141, 142} The results suggest that at higher salt concentration, the electrostatic repulsive force is significantly reduced. These results are consistent with previous studies for NPs.¹⁴²

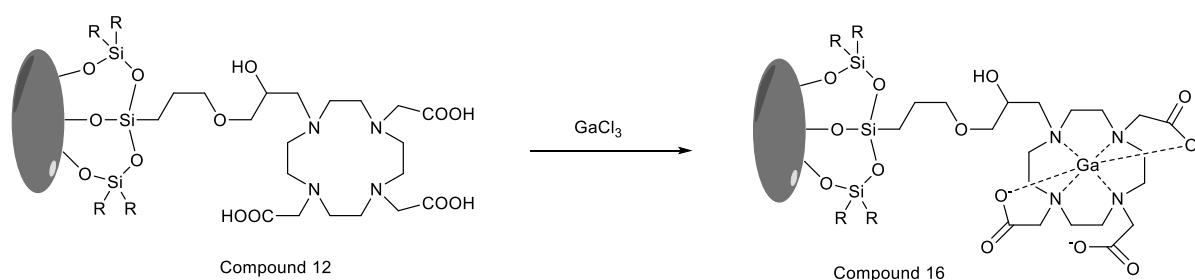
3.5.2.5 Gallium complexation for the DO3A coated NRDs

The half life of ⁶⁸Ga is 68 min. which gives sufficient time to perform metal ion coordination, purification and imaging studies. ⁶⁸Ga loading capacity and a study of the labelling effect on the samples core shape and size after the samples are exposed to high temperature and high

salt concentration were carried out. A ‘cold’ (i.e. non-radioactive) gallium binding experiment was carried out to study the effects of the labelling conditions on the NRDs.

The radiolabelling conditions for metal complexation reactions on the NRDs surface were investigated using stable gallium isotopes but this did not require the use of radiochemistry facilities and hence was easier to progress. One purpose of this experiment is to investigate if there is any attachment of the gallium metal ions to the silica layer coating and also if there is any effect of temperature and salt concentration in the reactions on the core NRDs size and shape. A sample of NRDs coated with silica-PEG (**compound 15**) was used as a control for gallium attachment. The complexation reaction was carried out by stirring the NRDs with GaCl₃ under elevated temperature (95°C) in 0.2 M ammonium acetate at pH 5 for 1 h before washing with a series of solvents (as described previously) to give **compound 16**, see Scheme 5.

To detect the percentage of gallium loading on the NRDs samples, ICP-OES was used. GaCl₃ (5 mg, 0.03 mmol) was used in the complexation reaction. An estimate of the amount of gallium(III) that would be required to form complexes with all macrocyclic chelators (based on the assumption that all of the chelators in the mass percentage of carbon, hydrogen and nitrogen are available for binding) would give *ca.* 0.9% gallium. The determined 1.59% indicates that there is also some attachment of gallium onto the silica layer surface in **compound 16**, see Scheme 5. Gallium attachment to the control sample of silica coated NRDs was carried out to quantify the percentage of attachment of free gallium on the silica layer (**compound 17**). The resulted ICP-OES of the control sample showed metal uptake that was similar to the macrocycle coated NRDs with 1.87% gallium by mass. It is thought that, gallium may have coordination interactions with the oxygen donor atoms present on the porous silica surface.^{143, 144} These may be weaker coordination interactions with the silica layer, when compared to the macrocyclic chelators, which is an important consideration for radiolabelling purposes. However, it is possible that the porous nature of the surface may offer cavities for gallium coordination within the silica shell.



Scheme 5: Complexation of GaCl₃ with DO3A on the surface of the NRDs.

An investigation of the effect of the harsh radiolabelling conditions on the NRDs size, shape and size distribution was carried out by applying an elevated temperature of 95°C and the samples were suspended in sodium acetate buffer (pH 5, 0.2M, 10 ml), **compound 18**. The critical parameters to investigate, after radiolabelling conditions have been applied, are the size and whether the silica coating remains attached. Minimal aggregation and no loss of silica coating are required.

NTA was carried out to detect any difference in the NRDs sizes before and after reaction with gallium(III). It was observed that, the NRDs-DO3A size before gallium coordination have a mode of 120 nm with a mean of 158 nm, whereas after labelling the mode size is 144 nm with a mean of 154nm. This shows a minor effect on the NRDs size and no aggregation occurred under such conditions. This indicates that the radiolabelling conditions should not cause any issues.

3.5.2.6 Measuring coated the NRDs Magnetic Resonance Imaging (MRI) properties

The relaxivity of the three NRD constructs were investigated using magnetic relaxation weighted sequences (T_1 and T_2) at a range of iron concentrations. Also, the influence of the coating materials under magnetic field was investigated to give the (R_1/R_2) relaxivity. Tracing the fate of the NRDs *in vivo* using multiple modalities is the main objective of the research in this chapter. Investigating the magnetic response of the designed NRDs under an applied magnetic field *in vitro* allows understanding of the behaviour of the NRDs constructs under T_1 and T_2 weighted pulse sequences and the correlation with various iron concentrations.

There is an expectation of increased T_2 relaxation correlated with increased NRDs iron concentration. T_1 may change more slowly and less consistently with the changes in applied magnetic field. Determining the ratio of relaxivity (R_2/R_1) reflects the effect of the chemical composition of the coating materials (macrocycles, PEG and silica) properties on the NRDs magnetic behaviour. Coating properties that can affect this include the variation of hydrodynamic size, permeability and hydrophilicity to the water molecules. An increase in the NRDs size is expected to inversely correlate to the R_1 to R_2 ratio. The coating thickness, permeability and hydrophilicity of the coating materials may have a direct relationship to the R_1 to R_2 ratio. Using NRDs instead of NPs may improve MRI relaxivity as described previously in section 2.3.4.

Contrast agent relaxivity can be defined as the ability of agent to improve MRI contrast by increasing the relaxation of the surrounding hydrogen proton nuclear spins using the relaxivity unit of s^{-1} per mmol of iron. The main mechanism of iron oxide contrast to improve T_2 weighted relaxivity relies on the paramagnetic properties of the IONPs. The chemical interchange interaction between the water molecules bound to the paramagnetic material surface and the free water molecules in the surrounding media can also contribute to T_1 weighted relaxivity. The T_2 relaxivity created by a paramagnetic agent leads to inhomogeneity of local magnet field, which has a large effect on T_2 nuclear spins.

The coated NRDs in this study are surrounded by silica which is likely to prevent the chemical interchange interaction. However, magnetic NRDs generally have a higher magnetic moment than gadolinium ions which leads to a much higher magnetic field fluctuation. Therefore, IONRDs have large effects on T_2 weighted signals. The MRI experiments were carried out using a Bruker 11.7 T MRI preclinical scanner and a clinical 3 T GE MRI scanner.

Three samples were prepared at a range of concentrations:

- 1- NRDs-DO3A (**compound 12**)
- 2- NRDs-DO3A and PEG 1:1 ratio (**compound 14**)
- 3- NRDs-PEG (**compound 15**)

The samples were filtered through 0.45 μm filter in order to remove any aggregations presented in the sample before they were applied to *in vivo* investigations, then the samples were diluted to form a range of iron concentrations after ICP-OES analysis (0.1, 0.3, 0.5 and 1 mM). Mass lost after filtration varied from between 35% to 82%.

The results showed the expected linear increase in T_2 relaxivity that correlates with iron concentration, see Figure 30 B. Under a T_1 weighted pulse sequence, all of the constructs responded slowly as expected with a general increase in relaxivity correlated with increased iron concentration see Figure 30 A. The NRDs coated solely with PEG (**compound 15**) gave the highest relaxivity for all iron concentrations. This may correlate with the fact that PEG is playing a significant role in suspending the NRDs and keeping them well separated.

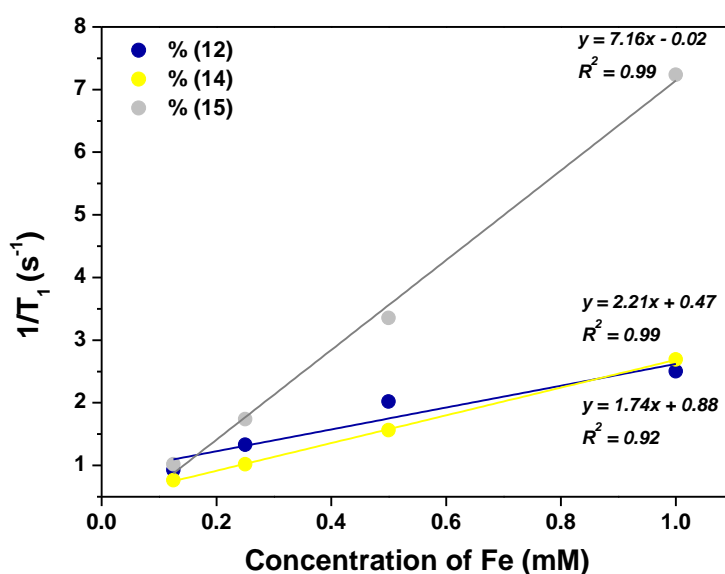


Figure 30 A: T_1 relaxivity plot of compounds 12, 14 and 15

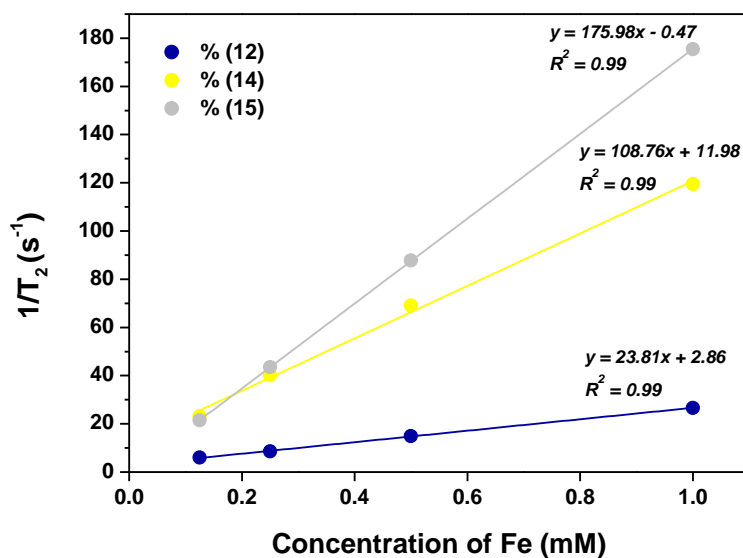


Figure 30 B: T_2 relaxivity plot of compounds **12**, **14** and **15**.

Compared to a previous report which used nanoparticles with a spherical shape coated with dextran,¹⁴⁵ for improving T_2 relaxivity. It is concluded that the NRDs from this work obtained a T_2 relaxivity about twice as big as the spherical NPs due to the effect of particle shape, as previously discussed, see section 2.4.

The R_2/R_1 ratio was calculated for all samples showing that the variability of R_1 and R_2 are dictated by the NRDs surface coating composition, which reflects a number of physical factors such as surface coating permeability to aqueous molecules, hydrodynamic size and hydrophilicity.¹⁴⁶ **Compound 15**, which has the PEG coating, has an R_2/R_1 ratio of 24 whereas for the solely macrocycle coated particles it is 14, see Figure 31. This could be attributed to the water diffusion on the NRDs coating layer as the main factor of determining the R_2/R_1 ratio. The water diffusion accessibility can depend on coating thickness and coating permeability, as well as the NRDs size and surface area ratio. However, further study is needed to fully investigate the effect of the coating properties on the R_2/R_1 ratio.

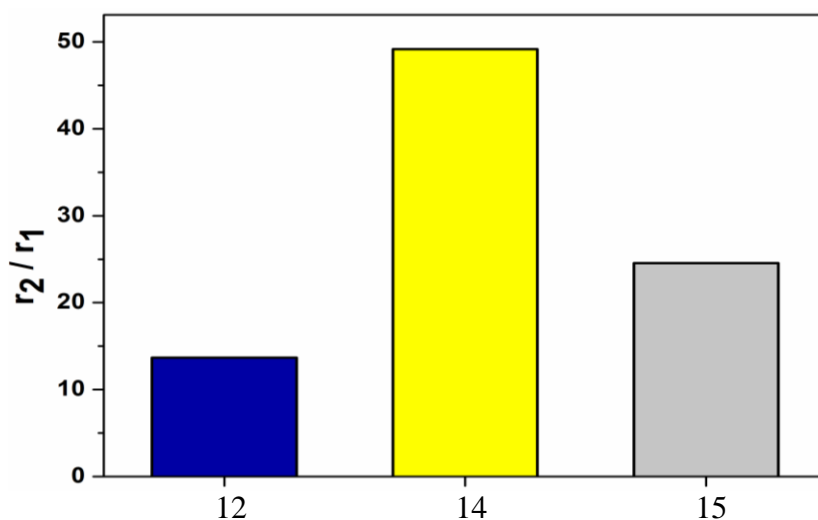


Figure 31: Measurement of MRI R₂/R₁ ratio relaxation for the coated NRDs

Many reports have confirmed that the relaxivity (R_1 and R_2) increases in a linear fashion with an increase in NPs core size.¹⁴⁷ This is expected as increasing the NPs core leads to larger magnetization around the NPs.¹⁴⁸ LaConte et al. attempted an investigation of the effect of the NPs coating thickness on the MRI relaxivity using IONPs coated with PEG. They found that R_2/R_1 value is significantly affected by the NPs coating thickness.¹⁴⁹ In this work, an influence of the coating chemistry components on the relaxivity was also observed. We assume the effect of the functional groups and charges of the NRDs surface (COOH, negative charges) are playing a role in determining the relaxivity values of R_2/R_1 , This is in agreement with previously published work.¹⁵⁰

Compound 14, which contains a mixture of PEG and macrocycles on the surface, shows the highest relaxivity ratio that can be attributed to the influence on the water molecule mobility, the hydrophilicity of the surface and the inhomogeneity of the local magnetic field. This behaviour needs further investigation in order to determine the nature of interactions and how the water molecules are diffusing among the structural components. Water diffusive permeability on the NRDs surface is the control factor of R_1 relaxivity. It is assumed that when the coating materials are permeable to water molecules, higher R_1 values result. On the other hand, when the NRDs coating materials are impermeable to water, the NRDs core size and magnetization are dictating the relaxivity with increasing control of R_2 .

Generally, the paramagnetic properties of the NRDs core have a significant effect on R_2 relaxivity by producing a local inhomogeneity in the magnetic field which promotes the spin-spin relaxation process of surrounding hydrogen protons.¹⁵¹ These properties could be further investigated. This effect on R_1 is reduced by increasing the thickness of the coating materials. Therefore, the coating materials have more influence on R_1 than R_2 .

3.6 Suitability of the coated NRD constructs for radiolabelling and *in vivo* multimodality imaging (MRI/PET)

In terms of the suspension stability of the samples, the solely PEG coating NRDs showed exceptional stability across all pH ranges and salt concentrations. The hydrodynamic sizes are reasonable for biological applications, they are not too large (particles >500nm will be recognized by the immune systems and immediately removed once passed through the spleen and liver) or too small (particles < 6nm are rapidly excreted via the kidneys).¹⁵² It was concluded that compounds **12**, **14** and **15** are suitable for radiochemistry and, potentially, for *in vivo* imaging.

3.7 Radiochemistry Reactions and Radiolabelling Stability Studies for Coated NRDs with Gallium-68

In this part of the research work, the NRDs were labelled with ⁶⁸Ga and the radiochemistry studies included experiments to give RCY, labelling stability analysis in serum and EDTA in an attempt to mimic the NRDs constructs labelling stability in physiological environments.

3.7.1 ⁶⁸Ga radiolabelling procedure for coated NRDs

⁶⁸Ga is a radioisotope with high positron decay % (90%) and a suitable half-life (68 min) for PET imaging applications.¹⁵³ In aqueous conditions, ⁶⁸Ga is entirely present in oxidation state III and all synthetic processes must proceed in the presence of weak coordinating ligands such as acetate, citrate and oxalate at pH between 3 to 5 in order to prevent production of insoluble Ga(OH)₃. Ionic hard base donor chelating ligands, such as DO3A or DOTA, are able to displace the weakly bound ligands to form six coordinate complexes with an octahedral geometry using four donor nitrogen atoms and two carboxylic acid donors.²⁸

The designed NRDs constructs (see section 3.5.1) were radiolabelled in a similar process to that described previously with cold gallium, see section 3.5.2.5. The reaction was adapted from a previous study with ⁶⁴Cu complexed with various macrocycles over IONPs surface¹¹¹ in order to investigate the coordination reaction of ⁶⁸Ga with DO3A.

The labelling procedure was carried out by suspending the NRDs (10 mM iron concentration) in ammonium acetate buffer (0.2 M, pH 5) and a solution of ⁶⁸GaCl₃ was prepared by elution from a 20 mCi Eckert and Ziegler ⁶⁸Ge/⁶⁸Ga generator in 5 ml of 0.1 M HCl which was then transferred to an acetone/ 0.1M HCl solution (97:3) before being completely dried at 90°C under a flow of compressed air. The ⁶⁸GaCl₃ solution was added to the prepared iron suspension and incubated for 15 min at 90°C to give the labelled construct. The reaction mixture was monitored by eluting the TLC plate with 0.2M citric acid to determine the presence of free ⁶⁸Ga and coated NRDs by radio-TLC. This method was used to investigate the radiolabelling differences in the presence or absence of PEG or DO3A chelators on the NRDs surface.

3.7.2 Radiolabelling stability tests for the coated NRDs

In this section, the ^{68}Ga radiolabelling stability was investigated. It is believed that there are two types of attachments to the NRDs surface, firstly, ^{68}Ga coordination with the macrocycle which was originally considered the strongest and desired attachment, secondly, attachment between the ^{68}Ga ions and the silica layer around the NRDs which was originally thought to be a weak bonding interaction that could be detached easily under physiological conditions.

EDTA is able to form metal complexes with Fe(III) and it is commonly used for chelating iron ions. Therefore, EDTA was selected as a competitor for NRDs/Ga binding. After labelling of the three coated NRDs constructs (compounds **12**, **14** and **15**) a 10 fold excess of EDTA (5 μL of a 10 mM solution) was added to the NRDs suspension with shaking for 60 min under elevated temperature at 90°C . The mixture was analysed by radio-TLC to determine the percentages of EDTA/ ^{68}Ga , free ^{68}Ga and ^{68}Ga -NRDs.

Around 16.5% of free gallium-68 was observed for samples containing macrocycles after 1 hour under these conditions with around 80% of the NRDs still radiolabelled (see Figure 32). It was also surprisingly observed that the NRDs coated solely with PEG, **compound 15**, were as stable as the macrocyclic coated NRDS (compounds **12** and **14**) which means that the gallium-68 is attached strongly onto the NRDs silica coating and/or among the PEG structure chains (see Figure 32).

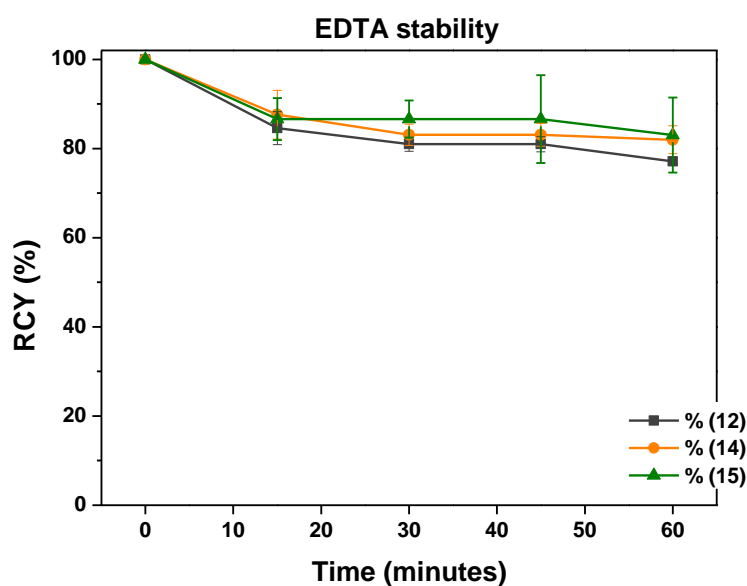


Figure 32: Testing the ^{68}Ga attachment stability of the coated NRDs against a competitive chelators EDTA for three samples, NRDs coated solely with DO3A (**compound 12**), NRDs coated with a mixture of DO3A and PEG, 1:1 ratio, (**compound 14**) and NRDs coated solely with Si-PEG (**compound 15**)

Unexpectedly, all the constructs loaded with ^{68}Ga in a high RCY. We anticipated that the control sample which has only silica PEG on NRDs surface (**compound 15**) to show no stable gallium attachment as there are no chelators present on the NRDs surface, but all samples were found to give high radiochemical yields (RCY) and labelling stability.

Once the free gallium ion is introduced in the human blood, it rapidly binds to the iron transport protein, transferrin. In addition, under normal conditions, the serum transferrin is only partially saturated with iron at around 30%, therefore, there is high capacity for binding

other metal ions such as gallium. The binding constant of the gallium(III) with transferrin is of similar magnitude as iron(III) binding constant. In addition, gallium(III) has a similar atomic radius to iron(III), *in vivo* the free gallium expected to be treated as iron by being complexed with apo-transferrin in blood plasma.¹⁵⁴

Human or mouse serum was used to investigate the release of gallium under physiological conditions. The solution of gallium-68 NRDs (compounds **12**, **14** and **15**) were then challenged against 5 ml of mouse serum at 37°C for 3 hours with constant shaking, following purification by centrifugation, the samples were analysed using radio-TLC. In the serum stability test, all the coated NRDs showed excellent radiolabelling stability with more than 90% of the NRDs still radiolabeled (see Figure 33) at the end of the experiments. This was again surprising as the NRDs coated solely with PEG (**compound 15**) were as stable as the macrocycle coated samples, (compounds **12** and **14**). It can be concluded that different coating materials do not make an obvious difference in the binding stability in serum.

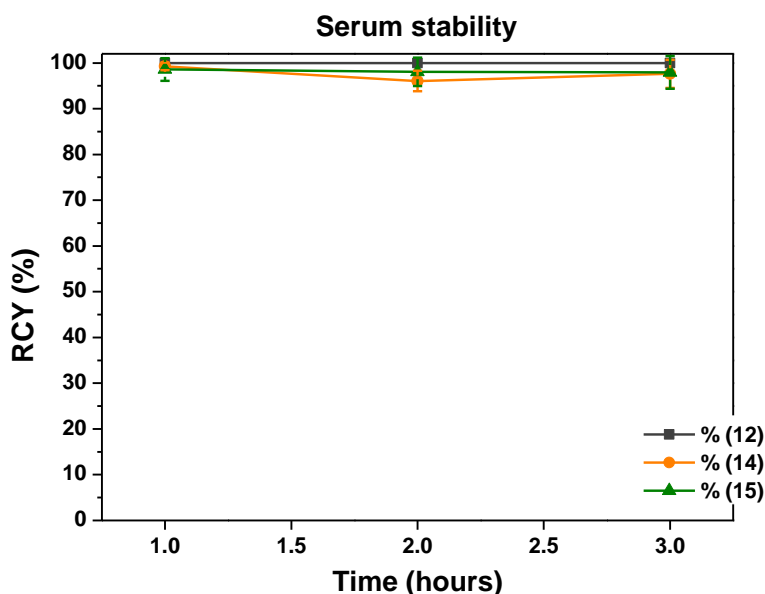


Figure 33: Testing the ⁶⁸Ga attachment stability to the coated NRDs against a competitive transferrin serum solution for three samples, NRDs coated solely with DO3A (**compound 12**), NRDs coated with a mixture of DO3A and PEG in a 1:1 ratio (**compound 14**) and NRDs coated solely with silica-PEG (**compound 15**)

From the obtained stability results, the gallium attachment to the NRDs surface is shown not to require macrocyclic chelators, the gallium may be interacting with the mesoporous silica surface and binding stably into surface accessible pores. Alternatively, gallium could be interacting with the oxygen atoms in the PEG chain. However, it is important to note that there is no need to use macrocycles for the final step radiolabelling as there is sufficient radiolabelling stability for all of the coated NRDs under challenge from EDTA and serum.

In comparison with other research in this area, Spiccia and co-workers studied the ⁶⁴Cu-NPs stability in a solution containing a cyclam competition chelator.¹¹¹ The free cyclam ligands were able to transchelate around 30% of the radioisotope after reacting for 5 min. Another study was carried out by Torres and co-workers to investigate the stability of ⁶⁴Cu and ^{99m}Tc attached to IONPs.^{155, 156} Their experiments were carried out for a longer time as

they used isotopes that have longer half-lives. Both of these samples showed no decomposition which demonstrated that it is a promising method.

In this experiment, the gallium labelling showed high stability attachment to all of the produced NRDs but the mechanism of gallium coordination is not yet fully understood. It is thought to be due to the interactions with the mesoporous silica surface. Controls have shown that under these conditions PEG alone does not provide sufficient stability for binding.

3.7.3 *In vivo* MRI/PET Imaging Biodistribution Study

Biodistribution provides information tracking a specific chemical compound of interest when administered systemically to the body of a human or animal. Biodistribution studies are performed to optimize drug efficacy and give valuable information about agent accumulation in different organs in the body. This information can give feedback on how to optimise agents and formulations to develop the desired biodistribution properties and excretion pathways.

The sample of NRDs coated solely with PEG (**compound 15**) showed the most attractive properties, as despite the absence of chelating units, it could be radiolabelled effectively with high stability. Therefore, this sample was progressed into biodistribution studies using multi modal imaging (PET/MRI) studies with CD1 nude female mice.

The mice were anaesthetised and the sample was intravenously tail vein injected and the PET imaging was performed straight after the injection. It is shown that the IONPs with sizes between 100 to 200 nm when used *in vivo*, are removed quickly from the system by the reticuloendothelial (RES) system and accumulate in the liver.¹⁵⁷ Tracking the NRDs-PEG-⁶⁸Ga using PET scanning, gave the observation of rapid accumulation of the construct in the liver after 5 min with a small quantity accumulated in the lung and spleen (see Figure 34). The PET images shows that the sample had the greatest uptake in the liver due to uptake by macrophages and Kupffer cells in the liver as part of reticuloendothelial system. Similar observation was noted in other published studies.¹⁵⁸ The PET scan showed a high uptake in liver for the NRDs, however the control with gallium-68 bound to either DOTA (not attached to NRDs) or transferrin (see Figure 34 right) the radioactivity was observed in the bladder, which indicates that the NRD construct is stable as this pathway was not observed for radiolabelled NRDs, see Figure 34.

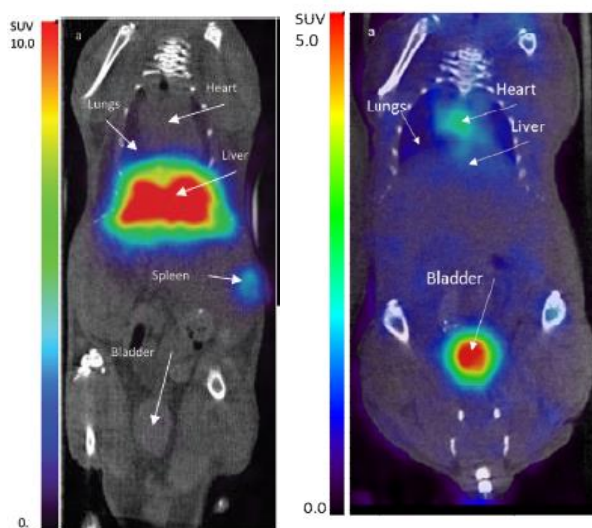


Figure 34: Biodistribution study of (left) NRDs coated with PEG (**compound 15**) using PET imaging and (right) a control of gallium-68 transferrin (labelled ex vivo). The images were acquired 5 min after intravenous injection.

After completing the PET scanning study, the mouse was sacrificed and moved to a wide bore MRI scanner (11.7 T) to acquire T_1 and T_2 weighted images, see Figure 35. This imaging technique aimed to reveal the differences in liver contrast with the expectation of a darker image at the site where the iron oxide NRDs are present. It was observed that in the T_2 weighted image, the liver is significantly darker than the T_1 weighted imaging. This was expected as the iron oxide has significantly more influence on the accumulated site under T_2 weighting.

The images proved that the radiolabelled NRDs were stable *in vivo* and the radioisotopes are strongly attached to the NRDs. The compounds have sufficient stability for *in vivo* imaging as the known biodistribution for free gallium or gallium-transferrin was not observed.

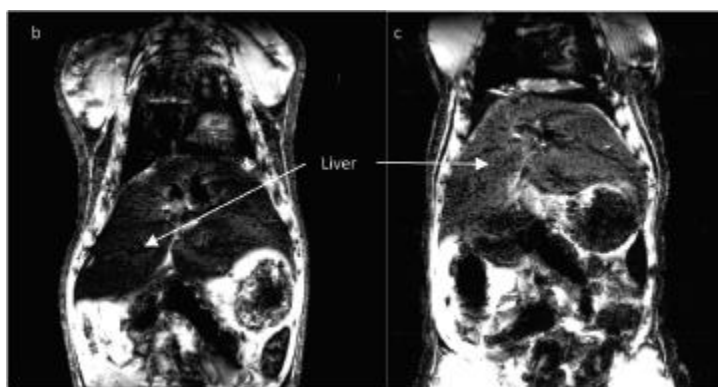


Figure 35: Biodistribution study of NRDs coated with PEG (**compound 15**) using MRI T_1 and T_2 weighted imaging. The images were acquired directly after PET imaging was performed at 20 min post injection.

Liver extraction experiments were performed after sacrifice of the mice and for the Ga-transferrin control experiment, the results showed that most of the radioactive species was bound to transferrin as expected. On the other hand, for ^{68}Ga -NRDs experiment, 90% of the

radioactive species was still attached to the surface of NRDs after 90 min post injection confirming the stability that was also observed in the imaging experiments.

3.8. Conclusion

This chapter describes the formation of radiolabelled iron oxide NRDs to be investigated as multimodal (MRI/PET) imaging agents. Three types of silica coated NRDs were designed with various ratios of PEG and DO3A molecules attached onto the surfaces. The silica layer coating was performed using the direct attachment method and the samples were fully characterized to ensure that they were suitable for biological applications using techniques including NTA, TEM, FTIR, zeta potential, MRI relaxivity, CHN and ICP-OES.

All of the samples showed appropriate hydrodynamic sizes, suitable surface charges and the presence of a silica coating layer. The solely PEG coated sample showed the optimum pH and salt stabilities and most importantly provide the highest MRI T₂ weighted relaxivity. The NRDs samples demonstrated better MRI relaxivity compared to spherical NPs due to the rod shape.

The labelling of the samples was initially tested under ‘cold’ reaction conditions to mimic the ‘hot’ labelling process. The samples showed high loading capacity, which indicated that the macrocycle is not required on the NRDs surface for stable radiolabelling as the silica-PEG coating could be labelled stably. This may be due to the ability of oxygen atom situated on the mid of PEG structure to interact with the gallium metal, although it is more likely that the silica surface is playing the key role in this system. All of the gallium-68 radiolabelled NRD samples demonstrated excellent stability in several competition assays using EDTA or serum with no sign of a chelator effect on the labelled NRDs stability. A negligible loss of the radiolabel was observed after 3 h of incubation for all the constructs. As there is no effect of the chelators on the ⁶⁸Ga complexation, NRDs coated solely with PEG were selected for an *in vivo* bio-distribution study using multimodal imaging techniques (MRI/PET). *In vivo* stability was determined and the NRDs could be detected using both imaging modalities.

Chapter 4

Targeting cancer cells using iron oxide nanoparticles attached to CXCR4 antagonists

4.1 Aims and background

Generally, the cancer imaging field is defined as using knowledge and methodologies that aim to supply the physician with information on the cancer characteristics and visualisation if the cancer has spread to other body parts. Using nanoparticle based agents for targeting cancer cells is opening up a broad new field of cancer diagnosis and treatment due to the unique nano-material properties that allow them to be equipped for a variety of targeted therapeutic, diagnostic and other multifunctional application purposes.¹⁵⁹

Many NPs based agents are used as core of the cancer targeting constructs, including, magnetic NPs, quantum dots (QDs), liposomal carriers, carbon nanotubes, dendrimers, silica NPs, polymeric NPs and other inorganic metal-based NPs.^{160, 161} Various molecules can be conjugated to the NPs for specifically targeting cancer cells *in vivo*, such as antibodies or peptides.¹⁶² This chapter focuses on the potential of targeting cancer cells using iron oxide NPs as a core. The targeting system is aiming to target the CXCR4 chemokine receptors that are overexpressed on the surface of many types of cancer cells.

This study aims to validate the targeting of a specific cell surface receptor on cancer cells *in vitro*. The designed CXCR4 antagonist was reacted to form a siloxane derivative and attached to the NPs surface using the ligand exchange method. The targeting of the receptor was confirmed using flow cytometry analysis with a leukemia cell line.

The previously synthesised iron oxide NPs described in section 2.4.2 were used as the core of the targeting vehicle. Two different siloxane macrocycle derivatives were synthesised, siloxy-cyclam (SiO-cyclam) and siloxy-cross bridge cyclam (SiO-CB-cyclam), see sections 4.3.1 and 4.3.4. Both systems were incorporated on to the NPs surface using the ligand exchange method, section 4.4, to form silica coated NPs with different macrocycles attached to the silica layer. The macrocycles were coordinated to metal ions to give complexes on the NPs surface with three metals used (copper(II), nickel(II) and zinc(II)) (see Section 4.4). The nanoparticle-macrocycle compounds were used to target Jurkat cancer cells *in vitro* to demonstrate their targeting capability, section 4.5.

The surface functionalised NPs were characterised via a series of techniques including TEM, NTA, FTIR, CHN, ICP-OES and the targeting validated with flow cytometry.

4.2 Introduction

Molecular imaging applied to cancer can be defined as a range of techniques employed to analyse tumour function at a molecular level. One purpose of cancer imaging is to provide information to develop a personalised treatment for the patient.

The size, surface chemistry and the possibility for loading molecules for delivery make nanoparticles flexible agents for diagnosis and therapy of cancer which could be achieved in a single treatment course whilst monitoring the treatment response using multimodality imaging.¹⁵⁹

4.2.1. Vectors for identifying and targeting cancers

Cancer cell recognition is based on targeting ligands to promote specific binding to a biomarker on the cancer cells. This type of targeted imaging will provide the physician with information about the cancer profile to allow them to perform a more precise diagnosis and give an appropriate therapeutic treatment.

Over the past decades, many biological processes specific to cancer progression have been discovered. A number of proteins and mechanisms that could be targeted and/or detected on the surface of cancer cells have been identified such as markers associated with variations in the extracellular matrix, membrane receptors stimulated by growth factors and markers of apoptosis.

To date, many biomarkers have been exploited for cancer targeting, for example, the transferrin receptor (TfR) was found to be overexpressed on the cancer cell surface. Some breast cancers were found to present a five-fold excess of TfR compared to normal cells. Also, an increased percentage of TfR receptors was found on prostate cancer, non-Hodgkins lymphoma, chronic lymphocytic leukemia and bladder carcinomas.

Another well studied group of receptors is the folate receptors. They are considered as highly selective cancer biomarkers and are overexpressed by many types of cancer cells such as lung, breast, colorectal, ovarian, renal and endometrial. The advantage of this receptor is that it almost completely absent in normal cells making it a good targeting marker for tumours. A further targeting marker has recently been evaluated and used for targeting cancer cells called underglycosylated MUC-1 antigen (uMUC-1). This antigen is overexpressed on many cancer cells including colorectal, gastric, prostate, lung and breast cancer cells. The cancer targeting biomarkers continues to expand with many other successful markers including $\alpha_v\beta_3$ integrin, HER2/neu receptor, CD20 receptors and c-MET.

In this section, the aim is to target a cell surface receptor called the CXCR4 chemokine receptor that is overexpressed on the surface of many cancer cells.

4.2.2 Nanoparticles targeting cancer cells:

NPs can be used for targeting cancer cells passively based on natural pharmacokinetic and phagocytic mechanisms that will control the NPs localisation. For specific targeting NPs can be functionalized and attached to a particular vector to target molecular processes in cancer cells. The active targeting mechanism allows physicians to more accurately diagnose the disease and, as already mentioned, establish suitable therapeutic treatments.

A study has been performed using SPIONs conjugated to a TfR protein targeting agent. The study showed around 45% reduction in signal intensity at the site of cancer cells using a T₂-weighted MR imaging sequence. Although the TfR protein is a good tool for targeting various cancers, it is also expressed in a moderate number on several types of normal cells such as Kuepfer cells, hepatocytes, endocrine system, pancreas, basal epidermis and testis.¹⁶³ Another study demonstrated that SPIONs attached to folate, which were injected intravenously into a rat model, could target implanted nasopharyngeal epidermal carcinoma xenografts. The MRI scan shows that the signal intensity at the tumour site decreased by about 40%.¹⁶⁴

Kiessling *et al.*¹⁶⁵ studied SPIONs attached to an RGD peptide for targeting $\alpha\beta3$ integrins overexpressed in nude mice bearing A431 or HaCaT-ras-A-5RT3 tumour xenografts. MRI imaging clearly identified the tumour's heterogeneous properties compared to non-targeted SPIONs, and the uptake of RGD-SPIONs was much more localised. For improved IONPs cancer targeting, Lee *et al.* produced IONPs coated with poly aspartic-acid attached to cyclic RGD peptides. The peptides were again designed for binding to integrin receptors ($\alpha\beta3$). The coated NPs also were attached to the DOTA chelator adjacent to the peptides for ^{64}Cu radiometal coordination in order to achieve multimodal imaging (MRI/PET). The authors proved that U87 tumour was targeted with very high and clear contrast compared to normal cells.¹¹⁶

In this work, iron oxide nanoparticles have been attached to a CXCR4 chemokine receptor antagonist for targeting the CXCR4 receptor on the cancer cells. The NPs were coated with a silica layer using the ligand exchange reaction and the CXCR4 binding macrocycles attached on the surface were used to form metal complexes and the constructs applied to targeting of cancer cells overexpressing the receptor *in vitro*.

4.2.3. Chemokines & Chemokine Receptors

Biologically, chemokines have a direct role in the migration of cells and particularly leukocytes to the locations of inflammation and they are also responsible for the immune system network regulation. Their effect arises by binding of signalling chemokine proteins to their chemokine receptors. Generally, the chemokine and chemokine receptor family consist of 50 chemokines and 18 chemokine receptors. The following sections particularly highlight the relationship between the CXCR4 (chemokine receptor) and CXCL12 (signaling chemokine) pair as they are the main targets for this work.

4.2.3.1. Chemokines

Chemokines can be defined as small proteins possessing molecular weight 8-12 kDa. Chemokines are classified into four sub groups depending on the orientation of the two cysteine residues that exist in all chemokines. Chemokines are an important component in the organization of the immune cell trafficking system, movement of leukocytes, angiogenesis, growth regulation and embryonic development.^{166, 167}

4.2.3.2. Chemokines receptors

Chemokine receptors are seven transmembrane helix domain proteins, they belong to the G-protein-coupled cell surface receptors (GPCRs) family that are 340 to 370 amino acids in length and are designated CXCR1 through CXCR5, CCR1 through CCR11, XCR1, and CX3CR1, based on their specific preference for certain chemokines.¹⁶⁸

Chemokine receptors are expressed in various kinds of non-hematopoietic and leukocytes cells. They function mainly in leukocyte chemotaxis and inflammation. Currently, almost 40% of approved drugs in the market are targeting GPCR receptors due to their accessibility on the cell surface and key biological roles.

4.2.3.3. CXCR4/CXCL12

Generally, CXCR4 receptors are presented on the surface of hematopoietic cells and a lower level is presented on astrocytes, neurons and vascular endothelial cells. CXCR4 plays a role in cardiac development and in hematopoiesis in the gastrointestinal tract.

The CXCR4 receptor binds to CXCL12 based on electrostatic properties in the binding mechanisms. The CXCL12 first and second β strands are positively charged whereas the α -helix contains negative charge. The charges contribute to the binding of CXCR4 and the CXCL12 ligand. CXCL12 is mainly generated from stromal cells in the bone marrow but also some other organs produce CXCL12 such as lung, liver, brain. CXCR4 receptor and its CXCL12 ligand are associated with inflammatory liver diseases, HIV and various types of cancer.^{169, 170}

Leukocytes that are produced from inflamed joints were shown to express CXCR4 and it was demonstrated that CXCL12 is involved in the pathogenesis of murine collagen-induced arthritis by attracting CXCR4(+) leukocytes to the location of inflammation. The connection between the CXCR4 and CXCL12 pair and cancer growth, metastasis and survival is becoming increasingly important. It was initially reported that CXCR4 shows overexpression in various cancer cells such as haemopoietic, mesenchymal and epithelial cancers.^{171, 172} In addition, CXCR4 is also highly expressed in further cancers including breast, colorectal, cervical, lung, prostate and pancreatic cancers. CXCR4(+) tumour cells travel to the location where there is abundant CXCL12 present such as the lung, liver and bone. In the presence of a CXCR4 antagonist, cancer cells movement will be inhibited in order to prevent cancer growth and spread.

4.2.3.4. CXCR4 Antagonists

Identification of a CXCR4 antagonist molecule is an important issue in terms of targeting the CXCR4 receptor. Using tetraazamacrocycles in the design of such antagonists has been validated and shown to provide effective binding to the CXCR4 receptor in cancer cells. A number of macrocyclic compounds have been investigated for CXCR4 receptor targeting such as AMD3100, AMD3465 and AMD3389. AMD3100 is the only licensed drug for a CXCR4 targeted therapy. Mainly cyclen (twelve membered) and cyclam (fourteen membered) tetraazamacrocycles have been used in the antagonist design. The amino groups in the azamacrocycles are protonated at physiological pH and provide the positive charge required for electrostatic interaction with the CXCR4 receptor surface.

Cyclam and cyclen azamacrocycles have a suitable cavity size and donor atoms for metal ion coordination and showed a high affinity for metal ions particularly first row transition metals. Pendant arms on macrocycles have the ability of formation of metal complex by directing the metals inside the macrocycle cavity but in this case the aim is to leave available coordination sites on the metal to bind to protein side chains (aspartate and/or glutamate on the CXCR4 protein surface).¹⁷³ The metal complex macrocycles have a higher affinity for the CXCR4 receptors than the free macrocycles due to the formation of coordinate bonds.¹⁷⁴

4.2.4 Techniques used for characterizing NPs cancer cell targeting properties

4.2.4.1. Flow cytometry

Flow cytometry is a technique utilized to study micrometre objects, such as cells, quantitatively. The aqueous sample is passed through a laser light and the interaction between the laser and the sample is reflected as a scattered beam and fluorescence can be detected. The received information is used to provide chemical and physical analysis of cells passing through.

The sample is injected into a flow cell where the sample cells are hydrodynamically focused into a thin stream with a sheath of fluid, which allows the cells to pass through the beam a single cell at a time. The cell flow pathway intersects with the applied laser, which is located in an orthogonal position to the flow. A cell passes through the sensing point, allowing the laser light to interact with it to generate scattered or fluorescence light, which is directed to a photo-detector to produce voltage pulses proportional to the number and intensity of the photons. The translated voltage pulses are converted into signals that can be displayed graphically.

The generated optical response consists of side scattered and forward scattered light. Also, the absorbed light from attached optically active dyes or cellular components can produce signals with different characteristics in term of wavelength and shifts compared to those produced by the exciting beam (fluorescence). This can be exploited by adding components, such as antibodies to target the CXCR4 chemokine receptor, which have a fluorescent dye attached to determine the presence of the receptor or whether antagonists are blocking it. The magnitude of the forward scattered beams (low angle scattered light at 0.5 to a few degrees) is directly proportional to the cell size whereas, the side scattered light (90°) is directly proportional to cell internal structure and granularity giving information about cell populations.

4.3. Synthesis of siloxane functionalised macrocycles (CXCR4 antagonists)

Cyclam is 14-membered N₄-donor macrocycle and cyclen is 12-membered N₄-donor macrocycle. Both molecules are widely used for drug production because they provide highly stable metal binding using the carbon skeletons to support the four nitrogen for coordination to the metal centre. Liang & Sadler *et al.* have summarised a literature review of the cyclam and cyclen complexation and their current and potential biomedical applications.¹⁷⁵

The full chemical names of the cyclam derivatives used in the work are:

- 1,4,8,11-tetraazacyclotetradodecane (cyclam)
- 5-(methyl)-1,5,8,12-tetraaza-bicyclo[10.2.2] hexadecan (methyl side bridged cyclam)
- 1,4,8,11-tetraazabicyclo [6.6.2] hexadecane (cross bridged cyclam)
- 4-benzyl-1,4,8,11-tetraazabicyclo[10.2.2] hexadecane (benzene side bridged cyclam)

The cyclam derivatives were synthesised to provide high affinity antagonists for the CXCR4 receptor that can be attached to NPs. The configurational restriction of the molecules on complex formation with a metal centre (due to the generation of chiral nitrogen) using an ethylene bridge ligand gives side bridge (SB) and cross bridge (CB) macrocycles. They allow metal ion coordination which provides improved CXCR4 receptor targeting affinity due to optimisation of the coordination sphere for binding to the protein. The most suitable metals for cyclam complex formation are transition metals include zinc(II), nickel(II) and copper(II).

The aim is to target the CXCR4 receptors on the surface of cancer cells using various synthesised macrocyclic CXCR4 antagonists that are attached to the surface of nanoparticles. The cyclam is configurationally restricted by forming side bridges and cross bridges with alkyl links between the nitrogen across the cyclam skeleton. Three different metal ions (nickel(II), copper(II) and zinc(II)) were coordinated to the synthesised antagonists in order to investigate the influence of the metal centres.

Preparation of various cyclam macrocycles linked to siloxane groups were produced to perform silica coating of the CXCR4 antagonists onto NPs using a ligand exchange mechanism. The functionalised particles can be used for targeting Jurkat cancer cells *in vitro* to investigate the affinity of the produced NPs toward the CXCR4 receptors on the cancer cells.

The chemical reactions included the initial synthesis of cyclam, side bridged cyclam and cross bridged cyclam, which were then reacted with siloxane (GPTES) molecules before complex formation with three different metal ions, copper(II), nickel(II) and zinc(II). The synthetic methods to produce the siloxane macrocycles derivatives are based on reported procedures for related molecules with some minor modifications.

4.3.1. Synthesis of the siloxane derivative of cyclam and metal complex formation

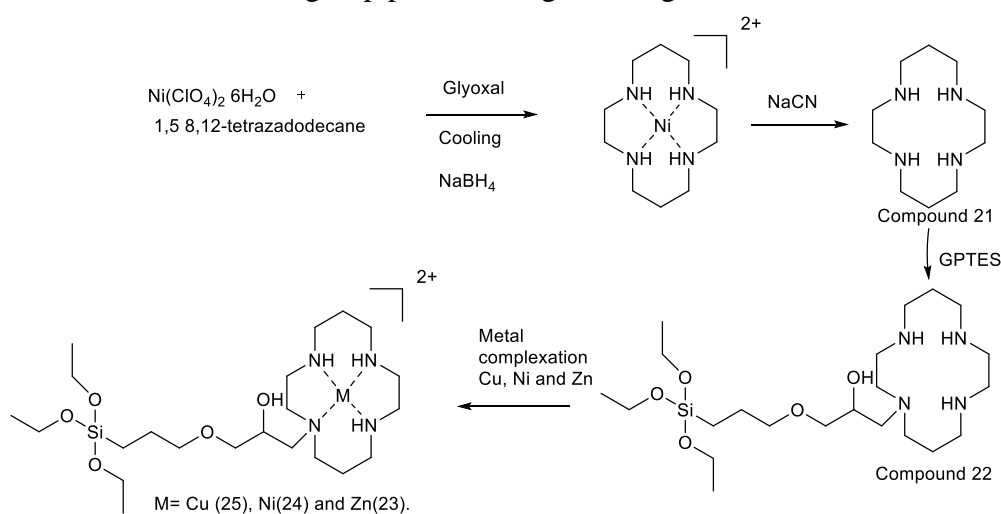
The first step towards producing the siloxane cyclam compound was synthesis of cyclam by following reported methods and then it was reacted with a siloxane derivative before reaction with transitional metal salts to form the complexes. Cyclam was synthesised following a reported method from Barefield *et al*¹⁷⁶.

1,4,8,11-Tetraazacyclotetradodecane (cyclam, **compound 21**) was prepared by reacting 1,5,8,12-tetrazadodecane; an acyclic amine with 1:1 molar ratio of glyoxal in presence of nickel(II) perchlorate and an excess amount of sodium borohydride. Those components result in a cyclised nickel containing macrocycle. Then sodium cyanide was used to remove the nickel(II) from the cavity of the macrocycle (**compound 22**).

In more detail, the cyclam synthesis reaction occurs when the pair of electrons on NH₂ present in acyclic 1,5,8,12-tetrazadodecane react with one of the carbon atoms on glyoxal which results in CO double bond on the glyoxal forming a C-OH group. The presence of sodium borohydride (NaBH₄) reduces the imine that subsequently forms. The nickel(II) ion serves as a template to fix the macrocycle shape orienting the nitrogen to react and close the ring to form 1,5,8,12-tetrazadodecane. Sodium cyanide is used for removing the nickel(II) ion in the complex with cyclam, see Scheme 6. The NMR spectra are consistent with the results reported by Barefield.¹⁷⁶

After cyclam synthesis, a single siloxane pendant arm is attached to the cyclam following a similar method to that performed by Barreto *et al.*¹¹¹ The reaction occurs by refluxing GPTES with 1:5 molar ratios of cyclam for 24 h. The excess of cyclam was used due to the presence of four nitrogen atoms on the cyclam which are all potentially reactive, however a 1:1 reaction is desired. Cold toluene was used to precipitate the unreacted cyclam which could be removed by filtration. The solvent was removed and the product dissolved in chloroform and washed with aqueous sodium hydroxide to give **compound 22**.

The product was characterised using NMR spectroscopy and mass spectrometry. The NMR signals showed the protonated molecular ion of the target siloxane cyclam. The results were in agreement with those reported by Barreto *et al.*¹¹¹ with multiple signals in the proton NMR spectrum in the range between 2.5-3.5 ppm suggesting that the cyclam is attached to the siloxane at the desired site. The methyl signal at 1.15 ppm could be used to quantify the amount of the siloxane group present using the integrals and showed a 1:1 reaction.



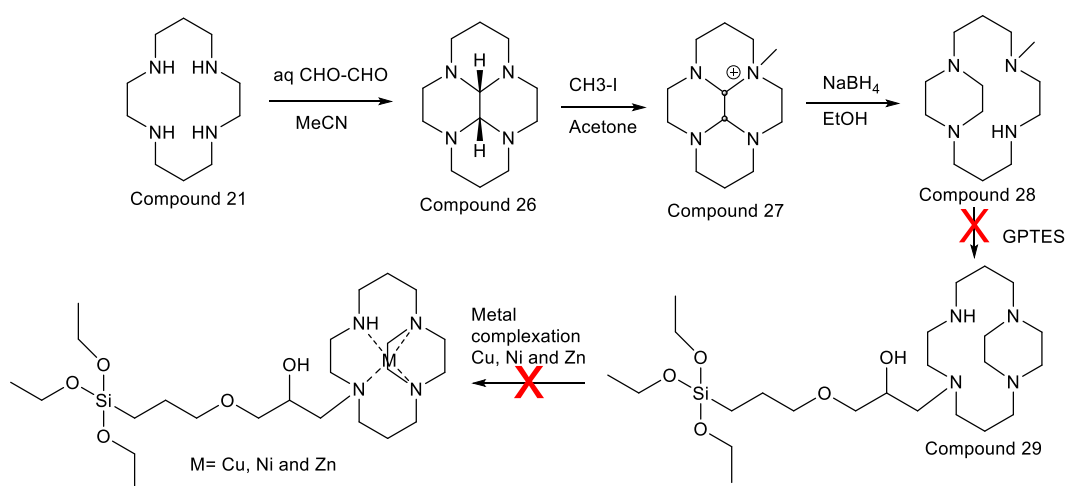
Scheme 6: Synthesis of siloxane cyclam derivative and metal complexation (Cu(II), Ni(II) and Zn(II)).

For the metal ion complex formation, acetate counter anions were used as it is a coordinating anion species and could mimic the binding interaction with CXCR4 aspartate residues. The metal complex formation reactions proceed by mixing the chelator solution with slight excess of the metal salts in an ethanolic solution. The excess acetate salt in solution was removed on purification using size exclusion chromatography. The mass spectrum shows molecular ion peaks at 541.3, 540.4 and 535.4 respectively for the zinc(II), copper(II) and nickel(II) complexes, compounds **23**, **24** and **25**.

4.3.2. Siloxane derivative of side bridged cyclam and metal ion complex formation

A further cyclam derivative with configurational restriction was synthesised by adding an ethyl side bridge between two adjacent nitrogen atoms in the cyclam ring. The aim is to compare the configurationally restricted molecules with the other synthesised cyclam derivatives when used for NPs coating and targeting the CXCR4 receptors.

The first step of the SB cyclam synthesis was adapted from a previously reported method performed by Kolinski *et al.*¹⁷⁷



Scheme 7: Attempted synthesis of siloxane methyl side bridged cyclam (SB)

Compound 21 can be bridged with glyoxal to produce a bis-aminal bridged cyclam, **compound 26**, which can be functionalised and derivatised to produce structurally rigidified side bridged macrocycle, **compound 28**, before an attempt to functionalise the macrocycle with the siloxane derivative to give **compound 29** which was not successful, see Scheme 7.

The bridged cyclam synthesis was based on the previously reported experimental methodology by Le Baccon et al.¹⁷⁸ The reaction was carried out under cold conditions at low temperature (-10°C) to prevent the formation of oligomers and the glyoxal was added slowly under the cooled conditions to give **compound 26**. The compound was synthesised in good yields ($>70\%$) providing a precursor to synthesise a range of configurationally restricted macrocycles. The ^1H NMR spectrum showed 22 protons with the expected complex splitting patterns due to the rigidity of the molecule.

Methyl iodide was used to mono-alkylate the glyoxal bridged cyclam followed by reduction of the quaternised bisaminal using NaBH_4 to give **compound 28**. The reduction procedure was carried out by slow addition of sodium borohydride over 1 hour to the mixture and then the reaction mixture was left to stir at RT for 8 h.

The four nitrogens of glyoxal bridged cyclam do not have the same reactivity due to the rigid nature of the molecule and orientation of the lone pairs on the nitrogen. Two of the nitrogens are available for substitution reactions and two are not accessible as they point in towards the molecular cavity. Furthermore as the first alkylation step quaternises one of the nitrogens and introduces positive charge into the molecule, a suitable solvent can be selected that will precipitate the monoalkylated product to prevent further reaction. This precipitation prevents the methyl iodide from attacking the other accessible nitrogen of the glyoxal bridged cyclam.

To introduce the siloxane component to the synthesised side bridged cyclam, a reaction was carried out with a 1:1 molar ratio of GPTES to side bridged cyclam and the mixture was refluxed for 3 days in an attempt to form **compound 29**. The mass spectrum of the product initially seemed consistent with the desired siloxane side bridge cyclam at 519.4 however this is the $[\text{M}]^+$ ion rather than the $[\text{M}+\text{H}]^+$ or $[\text{M}+\text{Na}]^+$ that would normally be observed. This is characteristic of a positively charged species which would be isolated if one

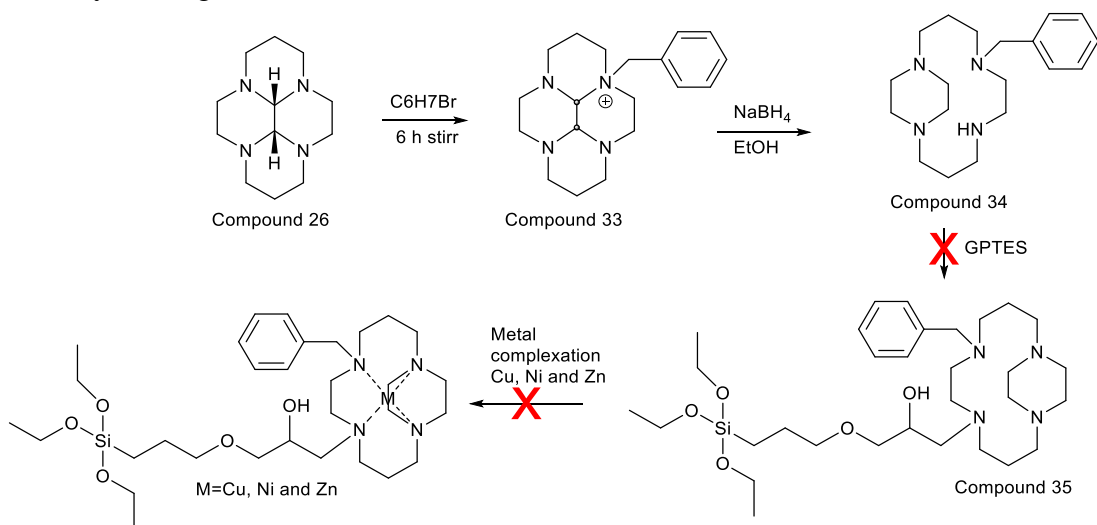
of the nitrogens had been quaternised, see Figure 36. There is precedent for this type of reaction when reacting side bridged cyclam species with alkyl halides and it is attributed the hydrogen bonding within the macrocycle which orients one of the piperazine ring nitrogens to increase its reactivity. Further evidence for this species comes from the attempts to form metal complexes, which were unsuccessful and demonstrate that the positively charged cavity cannot bind a metal ion (as would be expected). The mass spectra collected after reaction of the isolated species showed no peaks for metal complexes.

4.3.3. Siloxane derivative of the benzyl side bridged cyclam and attempted metal ion complex (copper(II), nickel(II) and zinc(II))

Similar methods to those in the previous section were applied in an attempt to synthesise the side bridged cyclam benzyl derivative to see if the desired compound could be isolated.

Scheme 8 shows the steps of siloxane benzyl side bridged cyclam synthesis. An analogous procedure was followed to the methyl derivative.

The mass spectrum showed the major peak at 595.5 which is the $[M]^+$ peak. Once again this indicates that whilst the siloxane has been attached it has not attached at the target nitrogen position, forming the quaternised species, see Figure 36. This is supported by the inability of the compound isolated to form complexes with the transition metal ions. There were no peaks for the metal complexes in the mass spectra following the reactions with the metal ions, only starting material was observed.



Scheme 8: The attempted synthetic steps to make the siloxane benzyl side bridged cyclam (SB)

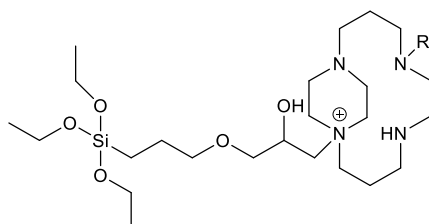
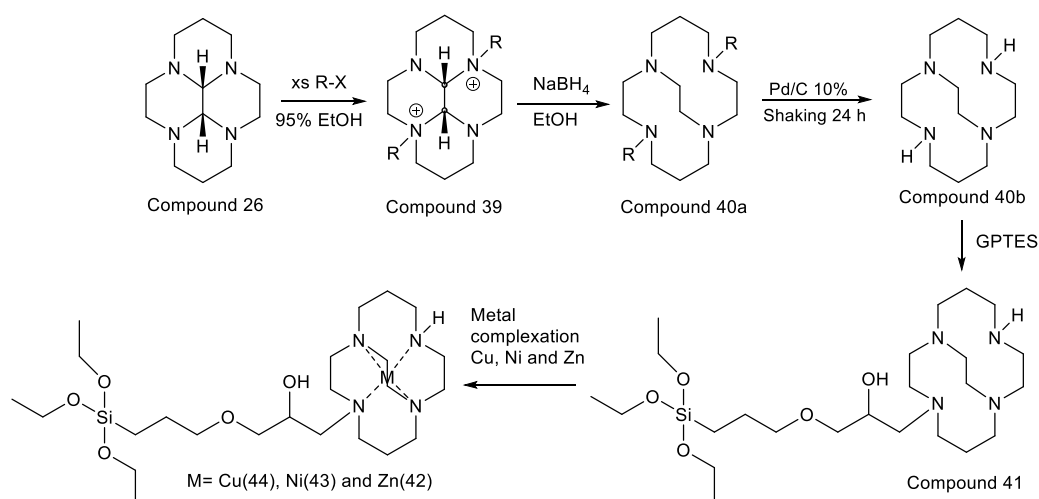


Figure 36: Quaternised product isolated from the reaction with the side bridged cyclam instead of the desired product

4.3.4 Siloxane derivative of cross bridged cyclam and metals complex formation

A further configurationally restricted cyclam structure, in this case a cross bridged cyclam was then selected for use as these chelators are known to have high binding affinity for the CXCR4 chemokine receptor and they will also avoid the issues of reactivity encountered with the side bridged species.

Scheme 9 shows the siloxane cross bridged cyclam synthesis steps, this is a novel compound but similar methodology for functionalising cross bridged cyclam with other functional groups has been reported by Wong *et al.*¹⁷⁹ The glyoxal bridged cyclam **compound 26** was synthesised as described previously. The next step is reacting benzyl bromide with the glyoxal bridged cyclam for 14 days in order to perform a substitution reaction on two of the nitrogen positions to give **compound 39**. NaBH₄ is then used in large excess to reduce the quaternised bisaminal to give the bis-benzylated cross bridged cyclam. This reaction is performed at R.T over 16 days to form **compound 40a**, if gentle conditions are not used then by-products are produced and yields are low. After the reduction step, the benzyl groups were removed by hydrogenation under an H₂ atmosphere with 10% Pd/C as catalysis to give **compound 40b**.



Scheme 9: Synthesis steps to form the siloxane cross bridged cyclam (CB) and to form metal ion complexes

The hydrogenation reaction works most efficiently at high pressure with shaking for 16 h to push the reaction to completion and give **compound 40b**. The product was characterized by ¹H NMR and mass spectrometry. The data was as expected and in agreement with previously reported similar work achieved by Wong *et al.*¹⁷⁹

Siloxane functionalization of the cross bridged cyclam was carried out by refluxing CB cyclam in a 1:1 molar ratio with GPTES in ethanol for 3 days to give **compound 41**. The mass spectrum shows the major peak for the desired product.

Metals complex formation was carried out by mixing ligand solutions with a slight excess of the metal salts in ethanolic solution. The excess metal salt was removed by size exclusion chromatography. The mass spectrometry result shows the main peak at 567.2, 568.4 and 561.3 for the three compounds which corresponds to zinc(II), copper(II) and nickel(II) complexes respectively, compounds **42**, **43** and **44**. Those results and further

analysis indicate the successful formation of the metals complexes with the siloxane CB cyclam derivative.

4.4. IONPs coated with siloxane macrocycles using the ligand exchange method

The aim is to coat the NPs with a silica coating and attach the CXCR4 antagonists in a single reaction using a ligand exchange coating method. There are various methodologies for silica coating of NPs including direct attachment and electrostatic interactions, see section 2.4 for more details. Using ligand exchange was utilized for attaching the various targeting vectors as it has previously been successfully used in this work (see chapter 3). This is the first attempt to use this silica shell methodology for attachment of CXCR4 antagonists onto the surface of NPs. The metal ion complex formation reaction was carried out on the surface of the NPs after attaching the free macrocyclic ligands.

The NPs were synthesised as previously described by mixing ferric, ferrous and oleic acid components under elevated temperature. The synthesised NPs become coated with oleic acid and are soluble in non-polar solvents such as toluene. After washing, the next step is the ligand exchange reaction by removing the oleic acid layer and replacing it with the siloxane macrocycle to react and form a silica layer with the macrocycle on the surface of the NPs. Two compounds were used; the siloxane cyclam (**compound 22**) and the siloxane cross bridged cyclam (**compound 41**). The exchange reaction was adapted from a literature report by Esben *et al.*¹¹³ The reaction is carried out in toluene and under basic conditions with aqueous triethylamine forming a biphasic system. The NPs coating reaction was achieved in a single step using this solvent mixture.

A range of characterisation techniques were used to demonstrate the presence of the coating including optical emission ICP-OES, NTA and CHN analysis. The NPs-OA (**compound 8**) was suspended in an organic solvent due to presence of oleic acid on the surface which renders the NPs soluble in polar solvents. The siloxane coating process via the ligand exchange reaction makes the NPs water soluble by replacing the OA with the silica, hence the particles leave the organic phase and move into the aqueous phase which can easily be separated. The mixture was stirred vigorously for 24 h at R.T to give the desired silica coated NPs with the macrocycles on the surface (compounds **45** and **46**).

NTA gives the NPs size and size distribution after the siloxane coating treatment (see Table 10).

NTA results Table	Mode	Mean	SD
Compound 47	95nm	121nm	±79nm
Compound 48	75nm	101nm	±40nm
Compound 49	108nm	161nm	±106nm
Compound 50	102nm	160nm	±81nm
Compound 51	72nm	92nm	±40nm
Compound 52	85nm	156nm	±94nm

Table9: NTA of NPs coated with macrocycles and after subsequent metal complex formation

In all cases, the NTA shows that the NPs size and size distribution increases after coating by approximately 10-50 nm when compared to the precursor NPs coated with OA which showed mode size of 62nm and average size of 88nm (**compound 8**). As seen in Table 10, after metal ion complex formation on the NPs surface, the size had increased in all the samples due to the silica coating.

NTA shows that, after metal complex formation with nickel(II) and zinc(II), the size and size distribution of NPs seems to be further increased, see Table 10. This could be attributed to a change in charge on the surface of the NPs, however with the amino macrocycles they would already have had positive charge due to protonation of the amine groups at neutral pH. It could simply be an effect of the reaction process and purification..

In the CHN elemental analysis (see Table 11), the carbon percentage of cyclam and CB-cyclam coating NPs, compounds **45** and **46** showed similar percentages showing consistent coating between the two different siloxy derivatives.

Elemental analysis	Carbon	Hydrogen	Nitrogen
Compound 45	21.15%	3.65%	4.46%
Compound 46	21.66%	5.26%	3.45%

Table10: elemental analysis of NPs coated Si-cyclam (45) and Si-CB cyclam (46)

The ICP-OES analysis of the metal ions over the NPs surface (copper(II), nickel(II) and zinc(II)) was carried out using direct injection of the NPs into the plasma using a method developed in the Archibald group with Dr Bob Knight. The zinc(II) complexes of both cyclam and CB cyclam compounds **49** and **52** showed reduced iron and high level of zinc on the NPs surface compared to the other metals (Cu^{2+} and Ni^{2+}) (see Table 12). However, the other metals showed similar iron and silica amounts and also, similar metals uptake over the NPs surface, copper(II) (compounds **47** and **50**) and nickel(II) (compounds **48** and **51**), see Table 12.

Elemental analysis	Iron	Silicon	Copper	Nickel	Zinc
Compound 47	6.67%	4.17%	0.418%	0.002%	0.003%
Compound 48	6.21%	3.180%	0.002%	0.484%	0.003%
Compound 49	0.98%	3.83%	0.003%	0.002%	9.39%
Compound 50	5.56%	2.033%	0.523%	0.001%	0.002%
Compound 51	5.58%	3.411%	0.004%	0.613%	0.002%
Compound 52	1.189%	1.87%	0.002%	0.003%	7.084%

Table11: Elemental analysis of metals complexed NPs coated with siloxane-yclam and siloxane-CB cyclam

4.5. Biological Studies of chemokine receptor binding using *in vitro* assays

The aim of this part of the research is to investigate the binding efficiency of the designed NPs toward CXCR4 receptors which are known to be overexpressed on many types cancer cells. Flow cytometry can be used to detect the attachment of the NPs to the cancer cells and determine how effectively that they can compete with monoclonal antibodies for binding.

There are several techniques that can be used to determine the NPs targeting of the cancer cells and the mechanism of binding such as ELISA, Western blot and immunostaining assays. However, flow cytometry is particularly useful for studying cell surface properties and markers. It counts individual cells with the properties plotted in a histogram.

In vitro targeting using Jurkat cancer cells was attempted. This leukemia cell line is known to overexpress the CXCR4 chemokine receptor and is relatively easy to culture. The Archibald group has previously used this cell line successfully in binding assays to assess CXCR4 antagonists. The assay is a binding competition assay which competes a known high affinity antibody for the CXCR4 receptor against the receptor bound nanoparticle. The aim is to investigate how well the antagonist coated nanoparticles bind to the cancer cells and their potential for *in vivo* targeted imaging. As discussed previously, flow cytometry is the ideal technique for characterising optical responses in cells and this can be combined with a fluorescent tag on the CXCR4 specific antibody to allow its detection. The side and forward scattered light also gives other information on cell properties but this is less important for this study.

In this experiment, the goal is to measure whether the NPs-Si-CB-cyclam-Ni (**compound 51**) binds to the CXCR4 receptors that are overexpressed on the cancer cells surface by introducing a competitive binding antibody. If the NPs inhibit the antibody binding then it will be confirmed that they are bound effectively to the CXCR4 receptor. The CXCR4 antibody mAb (44716.111) was used together with a secondary antibody that was tagged with a fluorescent dye. The binding assay is carried out by quantifying the number of mAbs bound the CXCR4 receptors by addition of a secondary anti-mouse IgG fluorescein tagged antibody that binds to the primary antibody. If no shift is observed from the positive control this means that either the nanoparticles are not bound to the receptor or that they are unable to compete with the anti-CXCR4 mAb whereas if there is a shift from the positive control this means that the mAb has been unable to displace the NPs bound to the receptor.

The positive control for Jurkat cells are shown in Figure 37. This shows the fluorescence count on adding the CXCR4 binding antibody to the cells followed by binding of a fluorescently tagged secondary antibody in the absence of the NPs (i.e. this is a maximum signal). This demonstrates the high level of expression of the CXCR4 receptor on these cells. The software plots the histograms which provide the median number for the cell population. Based on median number, any shift in fluorescence intensity can be measured in relation to the fluorescence intensity (MFI) value and compared. This can be expressed as a binding percentage.

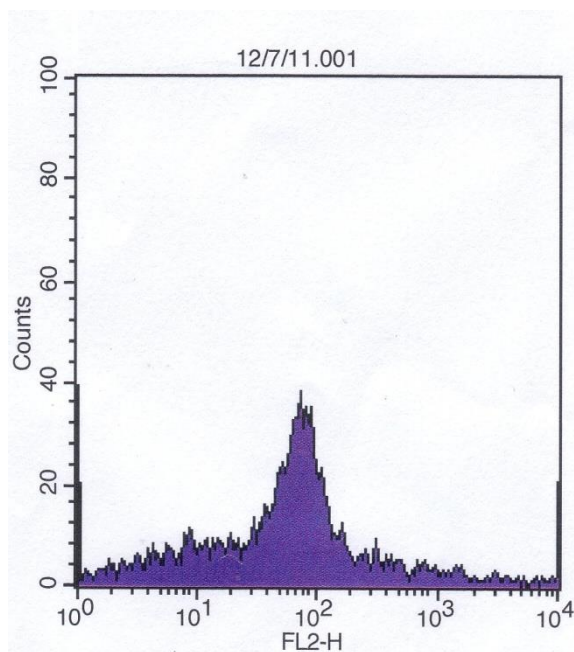


Figure 37: Positive control showing the level of CXCR4 receptor expression on the surface of Jurkat cells.

Flow cytometry also provides gating options which allow the selection of specific subset of cells to measure by rejecting any undesirable cells (i.e. dead cells) from analysis. This is achieved by making a dot plot of side scattering against forward scattering signals in order to present cell size distributions and granularity. This property also allows the deletion of cell clusters, cell fragments and cell debris.

The cell culture and flow cytometry measurements were carried out by Kate Nicholson. The sample containing NPs-silica-macrocyclone was applied to cultured Jurkat cancer cells which were cultured within a solution containing O₂ 95% and CO₂ 5% at 37 °C for one week to grow to a sufficient number. Before the experiment, the cells were centrifuged and re-suspended in PBS (4 ml) and the number of cells counted in order to prepare three samples for the positive control, negative control and the NPs sample with each containing 50 µl of cell suspension. For the NPs binding experiment, the NPs-silica-CB Cyclam-Ni (10µL of a 20mg/mL solution of **compound 51**) was added and incubated under refrigeration (4 °C) for 1 h. The negative and positive controls were set up as described previously. The nanoparticles sample then had the anti-CXCR4 antibody solution added to it (10µL) and the mixture was further incubated for 1h at 4 °C before being washed with PBS again, addition of the secondary antibody and analysis by flow cytometry. In Figure 38, the green peak represents the positive control which would equate to none of the particle sample being bound to the receptor if this was reproduced with the NPs sample. The solid purple peak represents the negative control, which indicates no anti-CXCR4 antibody bound, if this is emulated in the test sample it equates to 100% saturation of the receptor with NPs which are not displaced by the antibody. The NPs sample data (pink peak) virtually overlaps with the negative control which means that the nanoparticles based agent has blocked most, if not

all, of the CXCR4 receptors on the Jurkat cancer cells. A binding calculation depending on MFI median showed a binding efficiency of ca. 100%, see Figure 38.

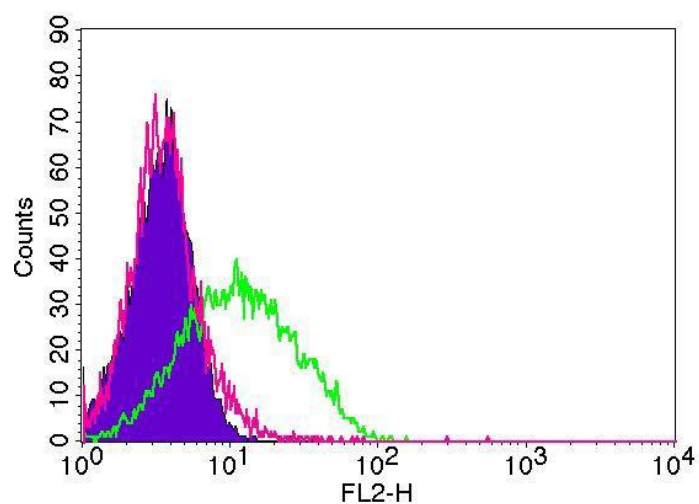


Figure 38: flow cytometry histogram of negative, positive and NPs based samples for detecting the NPS attachment on cancer cells surface.

The result demonstrates the potential for high affinity nanoparticles that can bind to the CXCR4 cell surface using azamacrocyclic antagonists attached to the NP surface via a silica shell mechanism. This is a validation of the strategy that shows significant potential for future development.

4.6. Conclusion

The current research that aims for improvements in the use of NPs for cancer diagnosis and therapy is focussed on improving the biocompatibility, imaging contrast properties and specific targeting to the sites of interest

In this chapter, a review of some of the latest developments in using NPs for cancer cell targeting and the also the use of CXCR4 antagonist vector was described. There have been a large volume of papers published regarding using nanotechnology for targeting purposes *in vitro* and some have transferred to *in vivo* studies. There is still a lot of work yet to be done to transfer these studies into clinical use and studying the potential for multifunctional applications that could be approved for cancer diagnosis and therapy.

In this work, the aim of targeting CXCR4 receptors on cancer cells using IONPs with molecular antagonists on the surface was achieved. The designed NPs were coated with a silica shell using some novel siloxy derivatives of cyclam macrocycles. Organic synthesis steps were carried out to attach a siloxane derivative to three cyclam derivatives. This was successfully carried out for the cyclam and cross bridged cyclam derivatives but there was an issue with the side bridged derivative where the alkylation took place at a tertiary amine site rather than a secondary amine site, and so the desired product was not isolated. Metal ions (copper(II), nickel(II) and zinc(II)) were complexed with the macrocycles to provide higher affinity CXCR4 antagonist units. The siloxane cyclam and siloxane cross bridged cyclam were synthesised in greater than 55% yield and showed efficient complex formation with first row transition metal ions. The compounds were then used for coating NPs prior to a preliminary assessment of one of the compounds in a biological assays to determine its receptor targeting properties. The coating mechanism based on the ligand exchange route. The coated NPs were analysed and found to have an acceptable size and coating efficiency to be used for *in vitro* and potentially *in vivo* experiments.

An *in vitro* cancer cells targeting assay using the NPs was performed using flow cytometry. This showed high affinity of one of the samples of the coated NPs in binding to the overexpressed CXCR4 receptors on the Jurkat cancer cells. Further investigation of toxicity and a full screen of all of the NP samples will be required to better understand the targeting capabilities. Other biological assays can then be carried out to determine 50% inhibitory concentrations and residence time at the receptor.

Chapter 5

Conclusion

5.1 Overall approach and key achievements

This work details the synthesis of iron oxide nanostructures for functionalisation, radiolabelling and the potential to target cancerous tissues. Two types of nanostructures were prepared; nanorod particles (NRDs) and nanosphere particles (NPs). The NRDs were equipped for multimodal imaging (MRI/PET) whereas the NPs were functionalized on the surface for targeting the CXCR4 chemokine receptor. MRI is an excellent technique for spatial resolution whereas PET offers high sensitivity for detection of the contrast agent.

Iron oxide is a paramagnetic material which offers high T_2 relaxivity as an MRI contrast agent. The shape of the NRDs is also shown to further enhance relaxivity properties compared to the commercially available NP agents. The NRDs offer a high surface area for radiolabelling of the NRDs. The NRD system was coated, the stability optimised, radiolabelled (^{68}Ga) and characterized using *in vivo* biodistribution studies.

The nanosphere system was demonstrated to bind to cancer cells using an *in vitro* model. The NPs were coated, conjugated to protein targeting molecules and tested using an *in vitro* targeting system in order to determine the competition binding against a target specific antibody using flow cytometry.

5.2 Synthetic methods to produce and coat iron oxide nanoparticles

Chapter 2 details the research work to synthesise and coat two different iron oxide based nanostructures in order to optimize core particle production. Iron oxide nanoparticles were synthesized and characterized to form the core material for further surface functionalization. Two synthesis methods were used; co-precipitation and thermal decomposition. The co-precipitation method was carried out by mixing ferrous and ferric components under basic conditions. The resultant NPs were reasonable in terms of size and size distribution with a low aggregation percentage. In an attempt to more precisely control the NPs sizes and size distribution other parameters were varied. Iron concentration, reaction time, base concentration and many other factors can affect the outcome. In this piece of work, the effect of the rate of base addition on the NPs size and size distribution when using the co-precipitation method was carried out. The main aim was to investigate the effect on NPs nucleation and growth stages, however it was determined that the effects were inconsistent. The focus was switched to the synthesis of iron oxide NPs using thermal decomposition approach.

The thermal decomposition method produced suitably sized NPs with a narrow size distribution. The two methods were compared in order to select one method as a standard way for producing the NP materials for the future experiments in this study. The co-precipitation showed only a reasonable size and size distribution but provided high yield, fast synthesis and used low cost chemical components, whereas the thermal decomposition method provided ideal NPs sizes and a very narrow size distribution but the precursors are expensive and the final yield is relatively low. Therefore, the co-precipitation method was selected to synthesise the core iron oxide NPs in this work despite its limitations.

Coating the NPs with an appropriate material is a critical step for biomedical applications. Silica is commonly known to have suitable properties such as biocompatibility, biodegradation pathways and low toxicity. The target is to achieve a simple, effective and rapid method of coating the NPs with a silica layer. Commercially available siloxane derivatives with the desired terminal functionality were used to produce silica coated NPs. Two coating strategies were applied; a direct attachment strategy and a ligand exchange method. The direct attachment method exploited the iron-hydroxyl groups present on the bare NPs surface to be reacted with a methoxy terminal group on the siloxane molecules to form Si-O bonds by a hydrolysis process to form coordinate bonds with the NPs Fe surface (Fe-O-Si). The resulting NPs were coated with a low percentage of aggregation and small NPs sizes. The ligand exchange method was applied using an oleic acid layer to be exchanged with the siloxane. This method also successfully produced silica layer on the NPs surface with acceptable size and size distribution. In conclusion, using siloxane derivatives with both coating methods (direct attachment and ligand exchange) produced suitable nanoparticles for biomedical applications.

The aim of influencing the MRI T₂ relaxivity by tuning the nanostructure shape was also accomplished. A key result from the work presented in chapter 2 is the synthesis of iron oxide nanorod structures by the application of an external magnetic field to the reaction flask during the NPs synthesis process. The sizes of all structures produced were applicable for biomedical applications with size and size distribution less than 100 nm.

5.3 Radiolabelling of nanoparticles with gallium-68

Chapter 3 focused on the preparation of three different ⁶⁸Ga radiolabelled NRDs for *in vivo* biodistribution studies using MRI/PET imaging techniques. The key advances presented in this chapter are:(1) using the NRDs shape to improve MRI relaxivity properties and (2) stable radiolabelling and *in vivo* imaging using MRI/PET imaging.

Initially, synthesis of siloxane-¹BuDO3A as a coating starting material was achieved by connecting ¹BuDO3A to the epoxy terminal functional group on the commercially available siloxane. This compound was effective in coating the nanoparticles to supply the materials for future experiments. Both or either of siloxy-¹BuDO3A and siloxy-PEG were used to coat the NRDs via the direct attachment method. Three types of coated particles were prepared as follows; NRDs solely coated with siloxy-¹BuDO3A, NRDs coated with a mixture of siloxy-¹BuDO3A and siloxy-PEG in a 1:1 ratio and finally NRDs solely coated with siloxy-PEG. The effect of the deprotection reaction conditions (to unmask the acid groups on the macrocyclic chelator) on the coated NRDs was tested.

The coating efficiency of all the designed constructs was characterised using FTIR and elemental analysis techniques. The presence of the silica coating layer, macrocycles and PEG was confirmed by assigning FTIR peaks at Si-O-Fe, C-O-C and C-N stretching frequencies and the elemental analysis techniques showed an increased percentage of silica, with carbon and nitrogen values correlated to the increased ratio of macrocycle over the NRDs surface which confirms the presence of each chemical component. The designed constructs sizes were characterized using TEM and NTA which show that all of the coated

NRDs produced had reasonable size and size distributions for biomedical applications. Also, the precipitation stability of the constructs to remain in suspension was tested against a range of pHs and salt concentrations and confirmed that the presence of PEG on the NRDs surface offers improved stability across the pH and salt concentration ranges tested. All NRDs constructs responded consistently (in a linear fashion against concentration) with respect to T₂ relaxivity, hence they are suitable for *in vivo* MRI imaging. The R₂/R₁ ratio was calculated based on the T₁ and T₂ slope extracted from relaxation measurements against iron concentrations and found to be suitable for effective imaging.

Gallium-68 radiolabelling was performed and all the designed constructs showed equal labelling reactivity with no influence of the macrocycle ratio, which was unexpected. The construct size and size distribution after radiolabeling were characterized using NTA and the results showed that the radiolabelling conditions have a slight effect on the NRDs size and size distributions for all samples, although acceptable sizes for biomedical applications were maintained.

In stability tests, all of the radiolabeled samples were tested in competitive assays against EDTA and serum. All of the constructs showed high stability toward the assays with more than 90% radioactivity retained after 3 h. Surprisingly, the control NRDs that coated totally with PEG showed as high radiolabelling and stability as the chelator functionalised samples. Therefore, NRDs coated with 100% PEG were selected to proceed to *in vivo* biodistribution study using multimodal imaging techniques MRI/PET. The biodistribution study showed that the NRDs accumulated in the liver of the animal with the attached radioisotope retained *in vivo*.

5.4 Conjugation of targeting materials

Chapter 4 reports an investigation of the NPs targeting potential against a cell surface protein. The prepared NPs coated with oleic acid were used to coat with a range of CXCR4 antagonists. Initially, four reactions to attach siloxane to various types of macrocyclic CXCR4 antagonists were performed. The produced products were complexed with various metals (Cu, Ni and Zn). Amongst the four species, the siloxane cyclam and siloxane cross bridged cyclams showed excellent metal ion complexation. Therefore, they were selected for further study and cellular assays.

After complexation reactions, the sample size and size distribution were analyzed using NTA. The samples showed a range of sizes between 72 nm to 180 nm which are acceptable for *in vivo* applications. The elemental analysis (ICP-OES) showed that the metals were complexed to the NPs successfully with the exception of zinc which showed a lower amount present than the copper and nickel loading.

A biological study of chemokine receptor (CXCR4) binding was carried out with siloxane-CB cyclam-nickel complex NPs using flow cytometry technique. The sample showed a high percentage of binding to Jurkat cancer cells in the competition assay (*ca.* 100%). This result is promising for future *in vivo* targeting applications.

5.5 Future Directions

Coating the NPs with a bisphosphonate (BP) layer could be a useful extension of this research work as BP is biocompatible and has useful *in vivo* applications. BP can also be used for direct gallium-68 complexation (and a range of other metal radioisotopes) without the need for high temperature conditions. This is a significant advantage as the elevated temperature causes some issues with aggregation (as observed in chapter 3). BP can strongly bind to the NPs surface and could also be combined with the silica coating and/or PEG derivatives to form particles with high suspension stability.

Chapter 6

Experimental

6.1 Materials

All of the chemicals were purchased from either Sigma Aldrich or Fisher Scientific. All reagents were used as supplied unless otherwise stated. Solvent drying procedures were carried out using molecular sieves that were oven-dried at 180°C for 24 hours. The standard organic work up used in this research work was to remove water from the solution with either sodium sulphate or magnesium sulphate (added as solid), and subsequently evaporate with the use of a rotary evaporator at reduced pressure in order to remove the solvents. The compounds were then further dried via Edwards RV5 oil pump linked to a Schlenk line with the potential to backfill for storage under inert atmosphere (either nitrogen or argon). Chemical dialysis processes were carried out using Spectra-por® Float-A-Lyzer® G2 with two different MW molecular weight cut-off membranes 100 kDa and 8-10 kDa, which were purchased from Spectrum Labs (Germany). The magnet used for nanomaterial purifications to influence the particle shape is a neodymium n52 block magnet with square dimensions (37.6 mm) and was purchased from MAGTECH.

6.2 Instrumentations

6.2.1 Inductively coupled plasma optical emission spectrometry (ICP-OES)

The results of the ICP-OES were obtained using a Perkin Elmer Optima 5300 DL spectrometer at the University of Hull operated by Dr Bob Knight. Most samples were supplied in the solid state and digested prior to analysis (mixture of HCl and nitric acid). Some samples were directly diluted and analysed without digestion to study the elemental distribution on the particle surface. Element standards references were prepared using 1000 ppm of iron, nickel, zinc and copper, all of which were purchased from Romil Pure Chemistry-UK. The reference solutions were diluted to prepare 1 and 10 ppm of iron, nickel, copper and zinc standard solutions for calibrations.

6.2.2 TEM

Suitable dilutions of samples were dropped onto carbon-coated copper grids and allowed to air-dry. Images were obtained using a Gatan US4000 digital camera (Gatan UK, Abingdon, Oxford) mounted onto a JEOL 2010 transmission electron microscope (Jeol UK, Welwyn Garden City, Herts) running at 200kV. Dr Ann Lowry contributed by recording the TEM images of all samples.

6.2.3 XRD

The X-ray diffraction machine was manufactured by Siemens, based in Germany (model AXS Diffractometer D5000). Dr Vincent Rocher contributed to the recording and interpretation of the XRD results.

6.2.4 Ultrasonicator

The ultrasonicator used was manufactured by Misonix Inc., which is based in New Highway, Farmingdale (USA) (model XL-2020). The sonication process was carried out as follows: the flask was placed in an ice bath and the ultrasonicator tuned; a 2-minute pulse-on and 1-minute pulse-off sequence was implemented with 70% of 200W power. Over a period of 15

minutes, 3ml of APTES was added drop-wise during the on-pulse stage of the sonication sequence.

6.2.5 Nanosight Nanoparticle Tracking Analysis (NTA)

Nanoparticle Tracking Analysis (NTA) was carried out with a LM10-HS microscope from NanoSight using a 75mW laser at 532nm (green). The concentration of the samples needed to be adjusted before analysing with NTA.

6.2.6 FTIR

The FT-IR spectra were recorded using Fourier transform infra-red spectrometer manufactured by Perkin Elmer.

6.2.7 CHN

CHN analysis was performed using Perkin Elmer EA1108 series II CHN/S Analyser.

6.2.8 Zeta Potential

Zeta potential analysis was carried out using an ELSZ-1000 type Zeta-potential & Particle Size Analyser, Otsuka Electronics Co. Ltd. Measurements were performed by Alicja E. Kownacka.

6.2.9 NMR

All ^{13}C NMR and ^1H NMR spectra results were recorded on a JEOL JNM-LA400 spectrometer (400 and 100 MHz, respectively). Splitting patterns are referenced against residual solvent signals, and are designated as *s* (singlet), *d* (doublet), *t* (triplet), *q* (quartet), *quin* (quintet), *m* (multiplet), *dt* (double triplet) and *br* (broad). Deuterated solvents were purchased from either Goss Chemicals Ltd or Cambridge Isotopes Ltd.

6.2.10 Mass Spectrometry

Mass spectrometry was carried out using electrospray ionisation (ESI) on a Finnigan LCQ Spectrometer at University of Hull. The results of the mass spectrometry were analysed and calculated based on the predominant natural isotopes of C, H, N and O, and on Ni, Cu and Zn metals.

6.2.11 Flow Cytometry

The sample was analysed on a FACScan flow cytometer (BD Biosciences Europe, Erembodegem, Belgium). Data were acquired and analysed with CellQuest software (Becton Dickinson) on an Apple Macintosh computer.

6.2.12 MRI

MR imaging used a Bruker Avance II 500 MHz NMR. Both T_1 and T_2 weighted images were measured in 1mm slices through a tube within a tube system, where the outer tube contained pure water as an internal control. The repetition time for T_1 and T_2 were 100 and 1000 ms,

respectively, whereas the gradient echo time for T_1 and T_2 were 3.3 and 10.3 ms, respectively. Prof. Mark Lorch assisted in the recording the MR images.

6.2.13 UV-vis Spectra

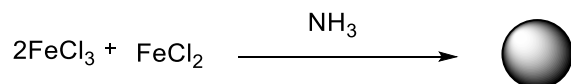
The results of the UV-vis were obtained using an Agilent 8453 diode array spectrometer. The samples were diluted to 100 μL concentration in methanol solvent.

6.2.14 Fluorescence Spectroscopy

Fluorescence spectra were obtained using a fluorescence spectrometer manufactured by Perkin Elmer (model LS 55 fluorimeter).

6.3 Synthesis and Coating of Iron Oxide Nanoparticles

6.3.1 Synthesis of iron oxide nanoparticles using co-precipitation: Compound 1



A hydrochloric acid solution was prepared (0.85ml, 12M) in deionised water (25ml). A mixture of ferric chloride (2g, 12.3mmol) and ferrous chloride (5g, 25.15mmol) were mixed and added drop wise to the prepared HCl solution over 60 minutes. NaOH (15g, 1.5 M, 250 ml) was added drop wise to the iron solution. During the NaOH addition, the pH of the mixture was adjusted to between 11–12. The reaction stirred for a further 1h at R.T. An external permanent magnetic was applied to attract the precipitated nanoparticles and then the supernatant was removed. This washing step was repeated four times with absolute ethanol. The NPs were then resuspended in a solution of diluted HCl (500 ml, 0.01M) and stirred for 2 h, centrifuged (3000 rpm, 15 minutes) and the isolated NPs were peptised with water until a clear transparent cationic colloidal suspension was obtained (**Compound 1**, 6.1 g).

TEM average particle diameter (taken from measurement of 10 particles): 8nm. See Figure A1. The standard error of TEM measurements ± 5 nm.

NTA. Mode 28 nm, mean 93 nm, SD ± 100 nm. See Figure B1.

6.3.2. A general method for synthesis of NPs with various sizes using dropwise addition timing approach

A mixture of FeCl_2 (2g, 12.3mmol) and of FeCl_3 (5g, 25.15mmol) in a diluted solution of hydrochloric acid (HCl) (25ml, 0.5M), were stirred for 1 h. NaOH (20ml, 1.5M) was added to the solution dropwise over various times (5, 10 and 30 min). The mixture was stirred for a further hour before an external permanent magnetic was applied to attract the precipitated NPs and the supernatant was removed by decantation. The resulted NPs were re-suspended in diluted solution of HCl (500 ml, 0.01M) and stirred for 2 hours. The NPs were centrifuged, and peptised by water until the resulting product was clear transparent cationic colloidal.

6.3.2.1. NPs synthesis with dropwise base addition (30 min):Compound 2

Final yield of compound 2, 6.04 g.

TEM: average particle diameter (taken from measurement of 10 particles): See Figure A2a: 10 nm. The standard error of TEM measurements ± 5 nm.

XRD: 30° (2 2 0), 35.4° (3 1 1), 43° (4 0 0), 54° (4 2 2), 58° (5 1 1), 63° (4 4 0).

NTA: Mode 42 nm, mean 55 nm, SD ± 14 nm. See Figure B2.

6.3.2.2. NPs synthesis with drop-wise base addition (10 min):Compounds 3

Final yield of compound 3: 6 g

TEM: average particle diameter (taken from measurement of 10 particles): See Figure A2b: 9 nm. The standard error of TEM measurements ± 5 nm.

XRD: 30° (2 2 0), 35.4° (3 1 1), 43° (4 0 0), 54° (4 2 2), 58° (5 1 1), 63° (4 4 0).

NTA: Mode 31 nm, mean 76 nm, SD ± 29 nm. See Figure B3.

6.3.2.3. NPs synthesis with drop-wise base addition (5 min) using:Compounds 4

Final yield of compound 6.2 g..

TEM: average particle diameter (taken from measurement of 10 particles): 8 nm See Figure A2c . The standard error of TEM measurements ± 5 nm.

XRD: 30° (2 2 0), 35.4° (3 1 1), 43° (4 0 0), 54° (4 2 2), 58° (5 1 1), 63° (4 4 0).

NTA: Mode 29, mean 94 nm, SD ± 51 nm. See Figure B4.

6.3.3 Synthesis of iron oxide nanoparticles using thermal decomposition method: Compound 5

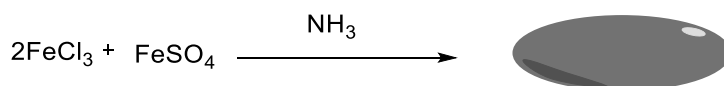
A mixture of oleic acid (1.69 ml, 6 mmol), phenyl ether (20 ml, 117.6 mmol), 1,2-hexadecanediol (2.58 ml, 10 mmol), oleylamine (1.6 ml, 6 mmol) and Fe(acac)₃ (0.706 g, 2 mmol) were added and stirred together under argon. The mixture was gradually heated over a period of 30 minutes until it reached 200°C, and was kept at this temperature for another 30 minutes. The temperature was then further increased slowly over a period of 30 minutes until the mixture refluxed at 265°C, and kept refluxing for 30 minutes. The temperature was reduced to R.T by removing the heating source. Ethanol (40 ml) was added to the solution, black deposit immediately formed, which was isolated by centrifugation, and re-dispersed in a mixture of hexane (20 ml) and oleylamine (0.05 ml) and oleic acid (0.05ml). The mixture was centrifuged and the precipitated NPs powder were isolated and the supernatant was kept. Ethanol (40 ml) was then added to the precipitated NPs again, and was centrifuged to discard the supernatant and re-dispersed powder in hexane. (0.09g, Compound 5).

TEM: average particle diameter (taken from measurement of 10 particles) 3.5nm. See Figure A3. The standard error of TEM measurements ± 0.5 nm.

XRD: Intensity/(2 theta): 31° (2 2 0), 35.5° (3 1 1), 43° (4 0 0), 54.5°(4 2 2), 58° (5 1 1), 63° (4 4 0).

NTA: Mode 9 nm, mean 8 nm, SD ± 3 nm. See Figure B5.

6.3.4. Synthesis of iron oxide nanorods (NRDs) via co-precipitation method:Compound 6



A mixture of FeCl_3 (5.4g, 20 mmol) and FeSO_4 (3 g, 10 mmol) in a solution of HCl (400 ml, 0.1 M) mixed with absolute ethanol (600 ml), which was bubbled with N_2 for 30 minutes prior to addition of the reagents. An external rare earth magnet was placed and fixed at a close range to the reaction flask (1- 1.5 cm) away from the round flask while adding a solution of concentrated ammonia water (35%, 15 ml) dropwise over 20 minutes under N_2 flow. The mixture stirred for a further 40 minutes before withdrawing the stirrer magnet bar; the magnet was applied to isolate the solid nanorods. The solid was separated and the supernatant was decanted. The solid was washed successively with absolute ethanol (x2), 60% ethanol (x2) and diethyl ether. The NRDs were dried and stored under N_2 for future experiments. The provided yield was 2.2g (Compound 6).

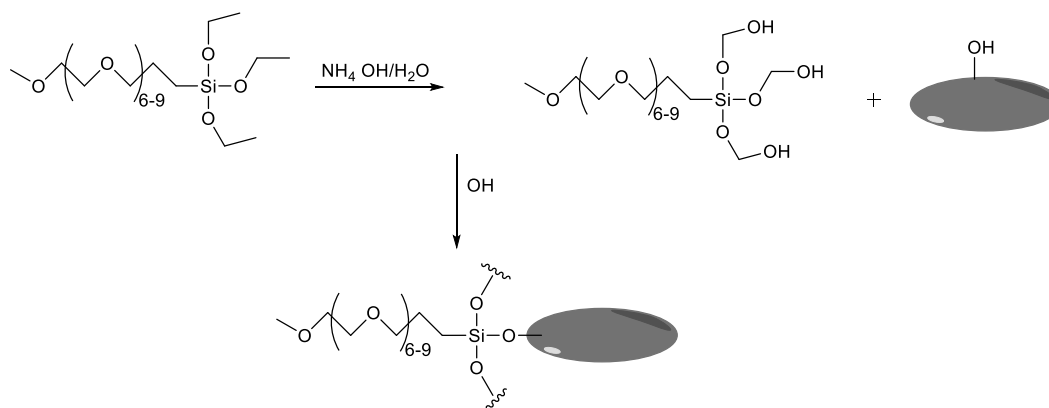
TEM: average particle diameter (taken from measurement of 10 particles) Length: 20 to 100nm, Width: 3-5nm. See Figure A4. The standard error of TEM length measurements ± 15 nm and width ± 1.2 nm.

NTA: Mode 20 nm, mean 32 nm, SD ± 15 nm. See Figure B6.

Zeta potential: pH 7.44, -1.73 mV.

Elemental analysis	
C	0.70%
H	1.15%
N	0.51%
Fe	57.94%

6.3.5. Iron oxide nanorods coated with silica layer by direct silica attachment: Compound 7



A mixture of $\text{FeCl}_3 \cdot 6\text{H}_2\text{O}$ (10.9 g, 0.04 mol) and $\text{FeSO}_4 \cdot 7\text{H}_2\text{O}$ (6g, 0.022 mol) was added to HCl (400 ml, 0.1 M) and ethanol (600 ml) and the solution stirred for 45 minutes under Ar. Ammonium hydroxide (35%, 20ml) was added to the iron solution drop-wise over 15 minutes while an external rare earth magnet was placed and fixed at a close range to the reaction flask (1–1.5 cm) away from the round flask, a black precipitate formed immediately. The mixture was further stirred for 30 minutes. The colloidal NPs were isolated using an external rare earth magnet and the supernatant was decanted. The NPs were washed successively with 60% ethanol (2 x 500ml), absolute ethanol (2 x 500ml) and diethyl ether (500ml) before being dried under a high vacuum to give a yield of 6 g).

The prepared NPs (0.3g, 1.3 mmol) were suspended in a solution of 60% ethanol (100ml) by extensive sonication. Ammonium hydroxide (20ml, 35%) was added dropwise to the NPs suspension and the solution was stirred for 30 minutes. GPTES (0.5 g, 2.11 mmol) in absolute ethanol (10ml), which was added dropwise to the NPs suspension over 15 minutes. The reaction was stirred for 48 hours under R.T and N_2 . The NPs were washed successively with 60% ethanol (2 x 100ml), ethanol (2 x 100ml), methanol (2 x 100ml) and diethyl ether (100ml), before being dried under high vacuum to give yield of 12.2g (compound 7).

TEM: average particle diameter (taken from measurement of 10 particles): 7.5nm. See FigureA5. The standard error of TEM length measurements ± 15 nm and width ± 1.3 nm.

Zeta potential: pH 7.4: SiO-NPs: 12 mV, NPs: 10mV.

NTA: Mode 28 nm, mean 54 nm, SD ± 40 nm. See Figure B7.

Elemental analysis (ICP-OES)	Fe	Si
NPs	57.9%	0.00%
SiO-NPs	54.7%	1.13%

6.3.6. Iron oxide nanoparticles coated with silica layer via ligand exchange method:Compound 8

NPs coated with oleic acid were prepared by mixing FeCl₃ (14g, 0.075 mol) and FeCl₂ (5g, 0.03 mol) in deionised water (300 ml). NaOH (250 ml, 1 M), acetone (200ml) and oleic acid (2.5 ml) was prepared under Ar and heated to 85°C over 15 min. Then the iron mixture and oleic acid (5 ml) was added dropwise over 10 minutes under Ar flow. The mixture was stirred for a further 20 minutes and then cooled at R.T. The NPs were precipitated with MeOH/acetone (1:1) and isolated using an external magnet and the supernatant was discarded. This washing process was repeated three times and the provided NPs were dried and stored under Ar condition.

NPs were suspended in toluene (20mg/5 ml) then GPTES (4ml), triethylamine (10ml) and deionised water (1ml) were added successively in a dropwise manner to the NPs suspension with stirring. The mixture stirred for 48 hours under Ar. Pentane (10 ml) was added drop wisely to the NPs mixture and the precipitated NPs were isolated using an external magnet and the supernatant was decanted. The pentane washing procedure was repeated three times and the NPs were dried and stored under Ar (9.8 g, Compound 8).

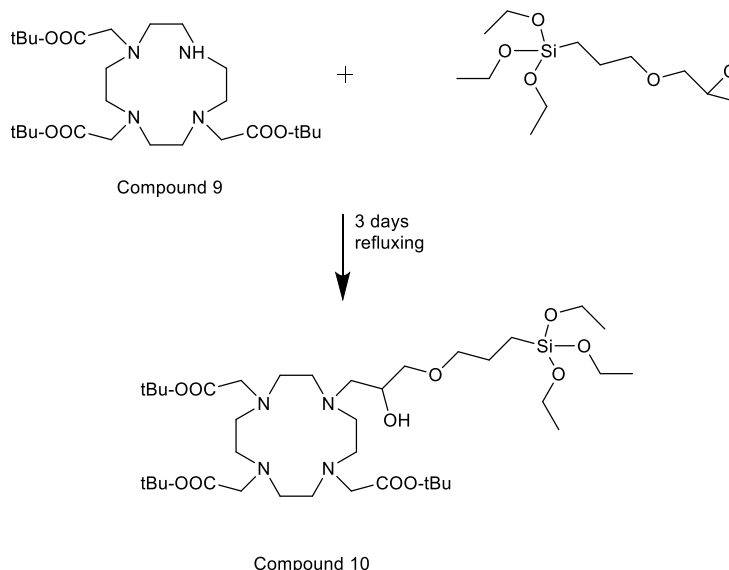
TEM: average particle diameter (taken from measurement of 10 particles): 7.5 nm. See FigureA6. The standard error of TEM measurements ± 1.2 nm.

Zeta potential: pH 7.14: 14.4mV.

NTA: Mode 62 nm, mean 88 nm, SD ± 54 nm. See Figure B8.

Elemental analysis (ICP-OES)	
Fe	43.2%
Si	15.2%

6.3.7. Synthesis of tri-*tert*-butyl 2, 2', 2''-(10-(2-hydroxy-3-(3-(triethoxysilyl)propoxy)propyl)-1,4,7,10-tetraazacyclododecane-1,4,7-triyl) triacetate: Compound 10



Method

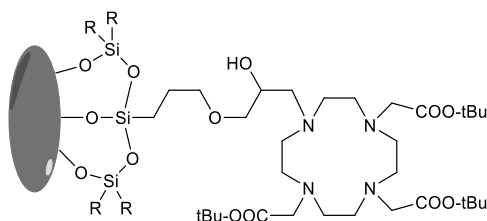
Compound 9 (669 mg, 1.3 mmol) was dissolved in CHCl₃ (30 ml). GPTES (360mg, 1.3 mmol) was dissolved in CHCl₃ (30 ml). The silica solution was added dropwise to the macrocycle solution, and the reaction was heated slowly until reflux. The reaction was refluxed for 3 days and was then concentrated *in vacuo*. The crude oil was redissolved in CHCl₃ (20 ml), washed with water (20 ml), dried (Na₂SO₄), filtered and concentrated *in vacuo* to yield an off-white oil (1.09g, compound 10).

¹H NMR: (CDCl₃):0.57-0.60 (m, 2H), 1.13-1.18 (t, 9H, CH₃), 1.32-1.39 (m, 27H, (CH₃)₃), 1.60- 1.64 (m, 2H, CH₂), 2.53-2.548 (q, 3H, CH₂), 2.62-2.88 (m, 2H, CH₂), 3.01-3.45 (m, 14H, CH₂), 3.61-3.68 (m, 10H, CH₂), 3.71-3.78 (m, 6H, CH₂).

<i>Elemental analysis (CHN)</i>	<i>Expected results%</i>	<i>Found results%</i>
<i>C</i>	56.41	56.35
<i>H</i>	10.08	9.91
<i>N</i>	11.44	11.29

MS (ESI): 793.8 [M+H⁺] (Compound 10).

6.3.8. Synthesis of tri-*tert*-butyl 2, 2', 2''-(10-(2-hydroxy-3-(3-(triethoxysilyl)propoxy)propyl)-1,4,7,10-tetraazacyclododecane-1,4,7-triyl) triacetate functionalised Magnetite Nanorods (Compound 11)

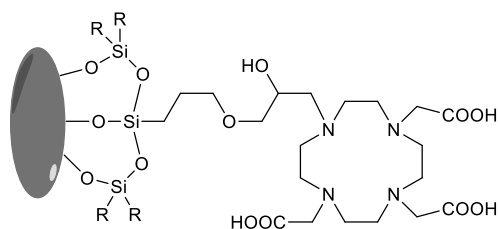


Compound 12

Magnetite nanorods, compound 6, (300 mg, 1.33 mmol) were suspended in a solution of EtOH (50ml, 60%). A solution of concentrated aqueous ammonia (28%, 6 ml) was added to the NRDs suspension dropwise over 10 minutes whilst stirring. To this suspension, Compound 10 (266 mg, 1.3 mmol) in EtOH (5ml) was added dropwise with stirring, and the reaction stirred at RT under N₂ for 48 hours. The solid was isolated using a rare earth magnet and washed successively with 60% EtOH (2 x 25 ml), EtOH (2 x 25 ml), MeOH (20ml) and ether (20ml), then dried *in vacuo* to yield a black solid (210 mg, compound 11).

Elemental analysis (CHN)	
C	5.65%
H	1.69%
N	0.67%
Fe	44.01%

6.3.9. Synthesis of Tri-*tert*-butyl-2,2',2''-(10-(2-hydroxy-3-(3-(triethoxysilyl)propoxy)propyl)-1,4,7,10-tetraazacyclododecane-1,4,7-triyl)triacetate functionalised magnetite nanorods: Compound 12



Compound 12

Compound 12 (194 mg) was suspended in DCM (30ml) with extensive sonication, then TFA (20ml) was added. The reaction stirred for 24 h at R.T under N₂. The solid was separated using a rare earth magnet, and the NPs were washed successively with EtOH (2 x 20ml), MeOH (20ml) and ether (30ml) then concentrated *in vacuo* to yield a black solid (yield 179mg of compound 12).

TEM (average taken from measurement of 10 nanoparticles in the field of view) length: 117nm, width: 3–5nm. See FigureA7. The standard error of TEM length measurements ± 16 nm and width ± 1.5 nm.

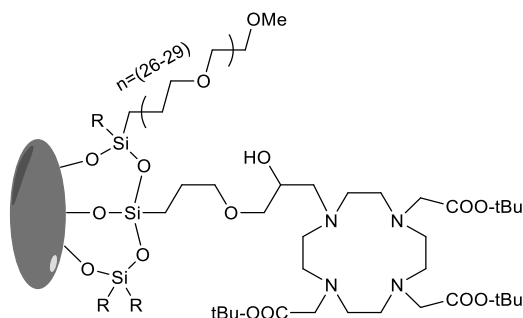
NTA: Mode 118 nm, mean 154 nm, SD ± 30 nm. See Figure B9.

Zeta potential pH 7.4 -13 mV.

FTIR: 3142, 2410, 2390, 1669, 1200, 1150, 889, 850, 600 cm⁻¹

Elemental analysis	
C	4.88%
H	0.95%
N	0.78%
Fe	43.05%
Si	0.95%

6.3.10. NPs coated with mixture of Si-tBuDO3A and Si-PEG 1:1 ratio via direct attachment method: Compound 13

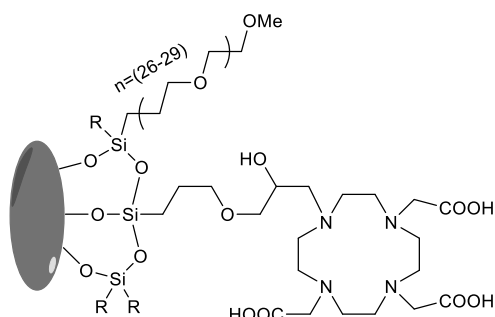


Compound 13

Compound 6 (300mg, 1.3mmol) was suspended in EtOH (60%, 50ml) solution, which was bubbled with Ar prior to use. A solution of ammonia (28%, 6ml) was added to the above suspension dropwise manner over 10 minutes. Compound 10 (133mg, 1.3mmol) in EtOH (5ml) and Si-PEG (52mg, 1.3mmol) were added sequentially to the iron suspension in a dropwise manner, and the mixture stirred for 48 h at R.T under N₂. The solid was separated using a rare earth magnet, and washed successively with 60% EtOH (2 x 25ml), EtOH (2 x 25ml), MeOH (20ml) and ether (20ml) then concentrated *in vacuo* to yield a black solid (260mg) (Compound 13).

Elemental analysis (CHN)	
C	4.34%
H	0.82%
N	0.17%
Fe	43.81%

**6.3.11. De-protection of NRDs coated with mixture of Si-BuDO3A and Si-PEG 1:1 ratio:
Compound 14**



Compound 14

Compound 13 (194mg) was suspended in DCM (20ml) with extensive sonication, then TFA (20ml) was added to the suspension and the reaction was shaken at R.T for 24 hours under N₂. The solid was separated using a rare earth magnet, washed successively with EtOH (2 x 20ml), MeOH (20ml) and ether (30ml) then concentrated *in vacuo* to yield a black solid (yield 149mg of compound 14).

TEM: (average taken from measurement of 10 nanoparticles in the field of view) Length: 111nm, width: 7nm. See FigureA8. The standard error of TEM length measurements ± 15 nm and width ± 1.2 nm.

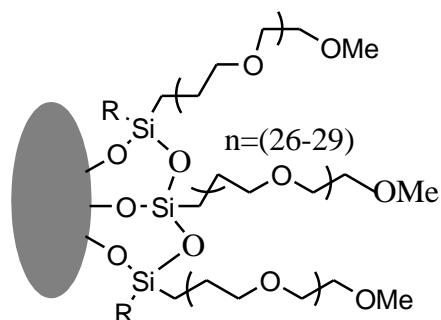
NTA: Mode 120 nm, mean 130 nm, SD ± 11 nm. See Figure B10

Zeta potential: pH 7.44 -18.1 mV

FTIR: 3142, 2867, 2390, 1669, 1117, 910, 880, 600 cm⁻¹

Elemental analysis	
C	4.92%
H	0.80%
N	0.29%
Fe	50.01%
Si	0.81%

6.3.12. NPs coated with of Si-PEG via direct attachment method: Compound 15



Compound 15

Compound 6 (300 mg, 1.3 mmol) was suspended in EtOH (60%, 50ml) solution, which was bubbled with Ar prior to use. A solution of aqueous ammonia (28%, 6 ml) was added to the NRDs suspension dropwise over 10 minutes. To this mixture, Si-PEG (116 mg) in EtOH (5ml) was added to the iron suspension in a drop-wise manner, and the mixture was stirred for 48 h at R.T under N₂. The solid was separated using a rare earth magnet, washed successively with 60% EtOH (2 x 25ml), EtOH (2 x 25ml), MeOH (20ml) and ether (20ml), concentrated *in vacuo* to yield a black solid (yield 240mg) (Compound 15).

TEM: (average taken from measurement of 10 nanoparticles in the field of view) 118 nm.

See FigureA9. The standard error of TEM length measurements ± 10 nm and width ± 1.2 nm.

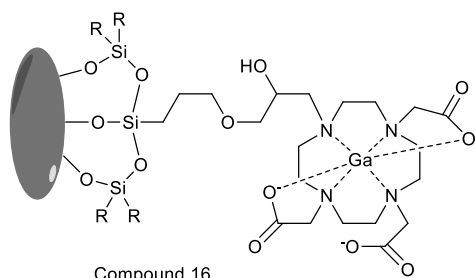
NTA: Mode 95 nm, mean 112 nm, SD ± 25 nm. See Figure B11

FTIR: 3138, 2873, 1644, 1410, 1201, 1088, 881, 797, 600 CM⁻¹.

Zeta potential: pH 7.4: -11.1 mV

Elemental analysis (CHN, ICP-OES)	
C	3.35%
H	1.09%
N	0.00%
Fe	43.2%
Si	0.52%

6.3.13. Synthesis of gallium(III) complex of 2, 2, 2-(10-(3-(3-(dihydroxysilyl)propoxy)-2-hydroxypropyl)-1, 4, 7, 10-tetraazacyclododecane-1, 4, 7-triyl) triacetic acid coating NRDs (Compound 16)



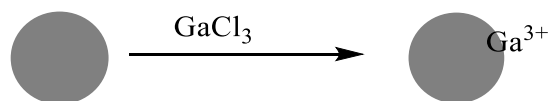
Compound 12 (20 mg, 0.086 mmol) was suspended in sodium acetate buffer (pH 5, 0.2M, 10 ml) and added to GaCl₃ (5mg, 0.03mmol) dropwise. The mixture was heated to 95°C and kept heated for 1 hour under N₂. The reaction cooled down to R.T and the solid was separated using a rare earth magnet, washed successively with 60% EtOH (2 x 20ml), EtOH (2 x 20ml), MeOH (20ml) and ether (20ml), then concentrated *in vacuo* to yield a black solid (27mg, Compound 16).

TEM: (average taken from measurement of 10 nanoparticles in the field of view) Length 112 nm, width: 5nm. See FigureA10. The standard error of TEM length measurements ±19 nm and width ±2 nm.

NTA: Mode 118, mean 134 nm, SD ±20 nm. See Figure B12.

Elemental analysis (ICP-OES)	
Fe	32.47
Si	0.426
Ga	1.59

6.3.14. Synthesis of (3-glycidyloxypropyl)triethoxysilane functionalised magnetite nanoparticles (Compound 17)



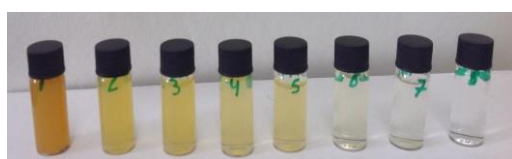
Compound 6 (309 mg, 1.34 mmol) was suspended in EtOH (60%, 25 ml) and ammonia (28%, 2.5 ml). GPTES (93mg, 0.335mmol) in EtOH (2ml) was added dropwise to the NPs suspension, and the reaction was stirred for 48 h at R.T under N_2 . GaCl_3 (50mg, 0.28mmol) was added to the iron suspension drop wisely, and the reaction was heated to 95°C and kept for 1 hour before being cooled down to R.T. The solid was separated using a rare earth magnet, washed successively with 60% EtOH (2 x 25ml), EtOH (2 x 25ml), MeOH (20ml) and ether (20ml), then concentrated *in vacuo* to yield a black solid (282 mg) (Compound17).

NTA: Mode 19, mean 36 nm, SD ± 32 nm. See Figure B13

Elemental analysis (ICP-OES)	
Ga	1.87
Fe	54.796
Si	1.133

6.3.15. Iron concentration stability test of 2-, 2'-, 2''-(10-(3-(3-(dihydroxysilyl)propoxy) 2-hydroxypropyl)-1-, 4-, 7-, 10-tetraazacyclododecane-1-, 4-, 7-triyl) triacetic acid functionalised magnetite nanorods (NRDs)

A dried sample of compound 12 (5.8 mg) was used for this measurement. NRDs were separated into eight different quantities (3.47mg, 100 mM), (1.738mg, 50 mM), (0.347 mg, 10 mM), (0.173 mg, 5 mM), (0.0347mg, 1 mM), (0.0173mg, 0.5 mM), (0.00347 mg, 0.1 mM) and (0.00173 mg, 0.05 mM). They were added into empty vials (2 ml capacity) before adding H₂O (2 ml) into each vial. The vials were sonicated until all NPs were suspended with no precipitate at the bottom of the vials. The pictures were taken at a series of intervals (5 minutes, 30 minutes, 1 h, 2 hours, 4 hours, 12 hours, 1 day, 1 week, 2 weeks and 1 month).



10 min



1 month

6.3.16. Studying the effects of PEG addition on NRDs stability with range of pHs

Three samples of ca, 7 mg from compounds 12, 14 and 15 were suspended in H₂O (22ml) separately with extensive sonication with no sign of precipitation on the bottom of the beakers. Each suspension was distributed within 11 2 ml vials. Solutions of diluted hydrochloric acid HCl (0.1M, 100 ml) and diluted ammonia water (0.1 M, 100ml) were prepared as stock solutions. A pH meter instrument was used to measure the pH in each vial. The pH was adjusted in each vial from 1 to 11 through the addition of diluted HCl and NH₃ with continuous pH monitoring. The samples were shaken, sonicated and aligned in three rows. Each sample vial was pictured after 2 weeks.

The effect of PEG on pH stability test: pH from 1 to 11.



Compound 12

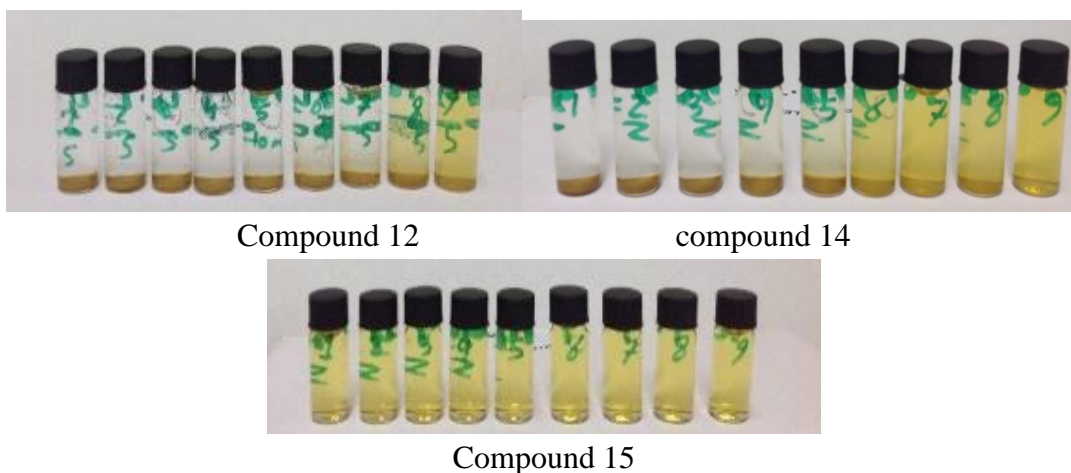
compound 14



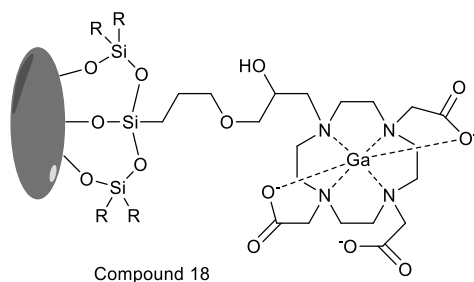
Compound 15

6.3.17. Studying the effect of PEG addition on NRDs stability with range of salt concentrations

Nine 2 ml vials were loaded with compound 12 (0.52mg), nine 2 ml vials were loaded with compound 14 (0.52mg) and nine vials were loaded with compound 15 (0.52mg). A stock solution of NaCl (0.1M, 100ml) was prepared, and added directly to one of each vials with shaking and sonication. The NaCl stock solution was then diluted to a range of lower concentrations 0.075M, 0.05M, 0.025M, 0.01M, 0.0075M, 0.005M, 0.0025M and 0.001 M and added to the remaining vials for each sample with shaking and sonication. The vials were pictured after 2 weeks.

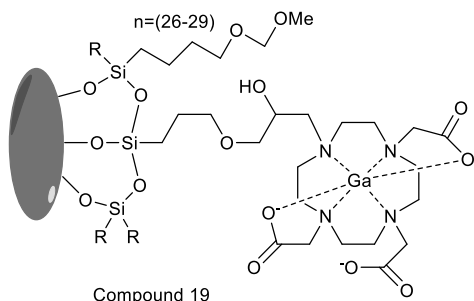


6.3.18. Synthesis of gallium(III) complex NRDs coated with DO3A (compound 18)



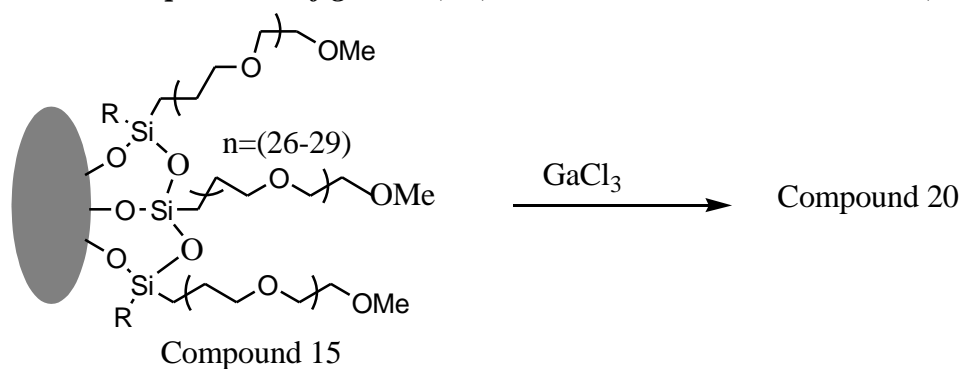
Compound 12 (20 mg) was suspended in sodium acetate buffer (pH 5, 0.2 M, 10 ml) and added to GaCl_3 (5mg, 0.03mmol) dropwise. The reaction heated to 95°C and kept heated for 1 hour under N_2 . The reaction was cooled to R.T and the solid was separated using a rare earth magnet, washed successively with 60% EtOH (2 x 20ml), EtOH (2 x 20ml), MeOH (20ml) and ether (20ml), then concentrated *in vacuo* to yield a black solid. (27mg, Compound 18).

6.3.19. Synthesis of gallium(III) complex of NRDs coated with DO3A and PEG 1:1 ratio (Compound 19)



Compound 14 (20mg) was suspended in sodium acetate buffer (pH 5, 0.2M, 10 ml) and added to GaCl_3 (5mg, 0.03mmol) dropwise. The reaction heated to 95°C and kept heated for 1 hour under N_2 . The reaction was cooled to R.T and the solid was separated using a rare earth magnet, washed successively with 60% EtOH (2 x 20ml), EtOH (2 x 20ml), MeOH (20ml) and ether (20ml), then concentrated *in vacuo* to yield a black solid. (26 mg, Compound 19).

6.3.20. Complexation of gallium(III) with NRDs coated with Si-PEG (Compound 20)



Compound 15 (20 mg) was suspended in sodium acetate buffer (pH 5, 0.2M, 10 ml) and added to a GaCl_3 solution (5mg, 0.03 mmol) dropwise. The reaction was heated to 95°C and kept heated for 1 hour under N_2 . The reaction was cooled to R.T and the solid was separated using a rare earth magnet, washed successively with 60% EtOH (2 x 20ml), EtOH (2 x 20ml), MeOH (20ml) and ether (20ml), then concentrated *in vacuo* to yield a black solid (27mg, Compound 20).

6.3.21. EDTA stability of ^{68}Ga complex of 2-, 2'-, 2''-(10-(3-(3-(dihydroxysilyl)propoxy)-2-hydroxypropyl)- 1-, 4-, 7-, 10-tetraazacyclododecane-1-, 4-, 7-triyl)triacetic acid functionalised magnetite nanorods (NRDs)

Ethylenediaminetetraacetic acid (EDTA) (5 μL , 10 mM) was added to the ^{68}Ga complexed NRDs (compound 18, 200 μL) and the mixture shaken for 1 hour at 90°C . The mixture was analysed using radio TLC.

Radio-TLC	% inc 90 C
Time (min)	
0	100
15	82
30	80
45	79
60	78

6.3.22. EDTA stability of ⁶⁸Ga complexed NRDs coated with Siloxy-DO3A and Si-PEG 1:1 ratio

Ethylenediaminetetraacetic acid (EDTA) (5 uL of 10 mM) was added to the ⁶⁸Ga complexed NRDs (compound 19, 200 μL) and the mixture shaken for 1 hour under high temperature 90°C. The mixture was analysed using radio TLC.

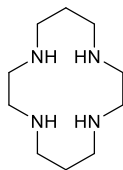
Radio-TLC	% inc. 90 C
Time (min)	
0	100
15	83
30	84
45	80
60	79

6.3.23. EDTA stability of ⁶⁸Ga complexed NRDs coated with Si-PEG

Ethylenediaminetetraacetic acid (EDTA) (5 μL, 10 mM) was added to the ⁶⁸Ga complexed NRDs (compound 20, 200 uL) and the mixture shaken for 1 hour under high temperature 90°C. The mixture was analysed using radio TLC.

Radio-TLC	% inc. 90 C
Time (min)	
0	100
15	83
30	85
45	80
60	79

6.3.24. Synthesis of macrocyclic ligands, synthesis of cyclam (compound 21)

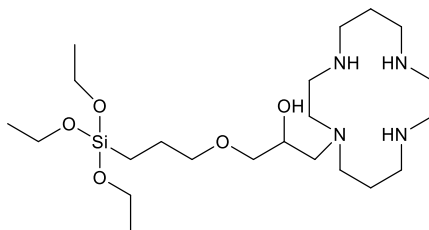


Nickel(II) perchlorate hexahydrate (54.7g, 0.15mol) was added to 400ml of deionised water. A solution of 1, 5, 8, 12-tetraazadodecane (24g, 0.15mol) was added dropwise to the nickel solution and the mixture stirred for 15 minutes before cooled to 5°C using ice bath and the mixture kept cooled for 30 minutes. Glyoxal (22.5 ml) was added dropwise to the mixture over 15 minutes, and the reaction continued stirring at R.T overnight. The mixture was again cooled to 5°C by ice bath and kept cooled for 30 minutes before adding NaBH₄ (11g, 0.3mol) portion-wise over one hour whilst the mixture was stirring rapidly. The mixture then was heated to 90°C, filtered whilst still hot and NaCN (29g, 0.6mol) was added to the filtrate solution. The mixture then was further heated to reflux and kept refluxing for two hours. An orange solution resulted after the mixture was cooled to R.T. The mixture was filtered through hyper flow powder. NaOH (15g, 0.6mol) was added with stirring and the aqueous layer washed several times with chloroform (6 x 80ml). The combined organic layers were dried with MgSO₄, filtered and concentrated to provide solid product (15.3g). The solid product was re-crystallised from chlorobenzene (150ml) by heating the mixture until all solid product dissolved and left for overnight re-crystallisation at R.T. The final product was white needles (9.9g).

¹H NMR (CDCl₃): δ 1.65-1.73 (quin, 4H, N-β-CH₂), 2.4 (br s, 4H, NH), 2.67 (s, 8H, N-α-CH₂), 2.68-2.75 (t, 8H, N-α-CH₂).

¹³C NMR (CDCl₃): δ 31.48 (N-β-CH₂), 51.42 (N-α-CH₂), 52.80 (N-α-CH₂).

6.3.25. Synthesis of siloxane ligand on cyclam (Compound 22)



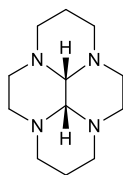
Toluene (40 ml) was heated to 70°C, cyclam was added (2.5g, 12.5 mmol, compound 21) and the resultant mixture heated to reflux. GPTES (0.7g, 2.5 mmol) in toluene (30 ml) was added to the prepared solution in a dropwise manner whilst refluxing. Heating at reflux was continued for 24 hours before the mixture was cooled and stored in the freezer overnight. The mixture was filtered, washed with cold toluene (20 ml) and evaporated to yield colourless oil. The oil was in chloroform, washed with NaOH (0.1M, 20 ml) solution, dried over sodium sulphate, and evaporated again to produce clear oil (1.1g, 93%, compound 22).

$^1\text{H NMR}$ (CDCl_3): δ 0.30 (m, 2H), 0.90 (m, 9H), 1.37 (m, 2H), 2.05 (m, 18H), 3.11 (m, 4H), 3.49 (m, 7H).

$^{13}\text{C NMR}$ (CDCl_3): δ 6.65, 18.35, 23.03, 45.50, 46.60, 47.53, 52.3, 57.93, 67.56, 73.06, 73.23.

MS: (ESI) m/z [M-I]. LRMS: calculated for $\text{C}_{22}\text{H}_{50}\text{N}_4\text{O}_5\text{Si}$: 479, observed 479.2.

6.3.26. Synthesis of cis-3a, 5a, 8a, 10a-tetraazaperhydropyrene (compound 26)

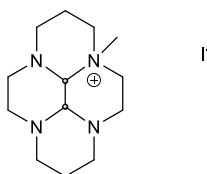


Cyclam (1.08g, 5 mmol, compound 21) was added to methanol (40 ml) and cooled to -10°C in an ice bath. A cooled glyoxal 40% solution (0.78g, 5 mmol) was added to the prepared solution slowly in a dropwise manner over 90 mins whilst stirring. The mixture was stirred for a further 40 mins at constant temperature before removing the cooling source, and the stirring process was continued for a further 4 hours at R.T. The mixture was concentrated and the crude solid product was dissolved in diethyl ether (200 ml). The solid residue was filtered and dried with MgSO_4 . The resulting solution was evaporated to give a white/yellow solid after further drying (1.2g, 100%).

^1H NMR (CDCl_3): 1.19-1.24 (m, 2H, N- β - CH_2), 2.08-2.37 (m, 8H, N- α - CH_2), 2.73-2.76 (d, 2H, N- β - CH_2), 2.91-3.02 (m, 6H, N- α - CH_2), 3.1 (s, 2H, H amin), 3.51-3.57 (t, 2H, N- α - CH_2).

^{13}C NMR (CDCl_3): δ 20.60 (N- β - CH_2), 45.70 (N- α - CH_2), 53.50 (N- α - CH_2), 55.37 (N- α - CH_2), 56.06 (N- α - CH_2), 77.4 (C amine).

6.3.27. Synthesis of 3a-[methyl]-decahydro-3a,5a,8a,10a-tetraaza-pyrenium iodide (compound 27)



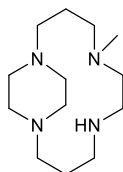
Cis-3a,5a,8a,10a-tetraazaperhydropyrene (1.77g, 8 mmol, compound 26) was dissolved in acetone (50ml). Methyl iodide (0.5 ml, 8 mmol) was added dropwise to the solution and stirred for 6 h at R.T. The mixture was filtered, the product washed with acetone (80ml), collected and dried to yield a white powder (2.45g, 95%).

^1H NMR: (D_2O) δ 1.32-1.35 (m, 1H), 1.74-1.78 (m, 1H), 2.15-2.43 (m, 6H), 2.78-2.97 (m, 8H), 3.23 (s, N- α - CH_3), 3.36-3.61 (m, 4H), 3.94-3.95 (d, 1H), 4.14-4.19 (m, 1H).

^{13}C NMR: (D_2O) δ 18.17 (N- β - CH_2), 18.91 (N- β - CH_2), 42.27 (N- α - CH_2), 46.58 (N- α - CH_2), 48.83 (N- α - CH_2), 51.39 (N- α - CH_2), 52.24 (N- α - CH_2), 53.16 (N- α - CH_2), 54.02 (N- α - CH_2), 64.80 (N- α - CH_3), 69.65 (C amine), 83.03 (C amine).

MS: (ESI) m/z 237 [M-I]. LRMS: calculated for $\text{C}_{13}\text{H}_{25}\text{N}_4$: 237.1; observed 237.324.

6.3.28 Synthesis of 5-(methyl)-1-, 5,8,12-tetraaza-bicyclo[10.2.2] hexadecane (compound 28)



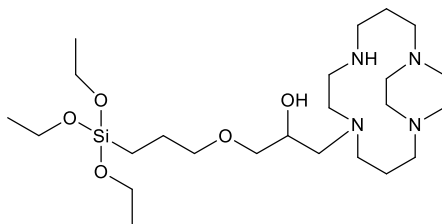
3a-[methyl]-decahydro-3a,5a,8a,10a-tetraaza-pyrenium bromide (2.5g, 69 mmol, compound 27) was dissolved in ethanol (200 ml), cooled to 0°C and sodium borohydride (5.24g) was added dropwise over 30 minutes. The mixture was then stirred for 24 hours at R.T. The mixture was refluxed for 3 hours before being left stirring at R.T for a further 24 hours. The solution was concentrated and re-dissolved in water (75 ml). The mixture pH was increased to 14 by KOH pellets before extracting the base solution using with DCM (6 x 100ml). The organic phases were combined, dried, filtered and concentrated to yield a colourless oil (0.5g, 50%).

^1H NMR: (CDCl_3) δ 1.57-1.67 (m, 4H, N- β - CH_2), 2.05 (s, 3H, N- α - CH_3), 2.13-2.21 (m, 2H, N- α - CH_2), 2.39-2.53 (m, 10H, N- α - CH_2), 2.16-2.63 (m, 2H, N- α - CH_2), 2.77-2.8 (m, 2H, N- α - CH_2), 2.91-2.94 (m, 2H, N- α - CH_2), 3.17-3.24 (m, 2H, N- α - CH_2), 4.46 (br s, 1H, NH).

^{13}C NMR: (CDCl_3) δ 23.86 (N- β - CH_2), 26.32 (N- β - CH_2), 39.38 (N- α - CH_3), 47.50 (N- α - CH_2), 48.47 (N- α - CH_2), 51.10 (N- α - CH_2), 51.93 (N- α - CH_2), 56.50 (N- α - CH_2), 57.02 (N- α - CH_2), 59.71 (N- α - CH_2), 59.89 (N- α - CH_2)

MS: (ESI) m/z 237 [M-I]. LRMS: calculated for $\text{C}_{13}\text{H}_{28}\text{N}_4$: 240.1 observed 240.324.

6.3.29. Attempted synthesis of siloxane ligand on methyl side bridged cyclam (compound 29)



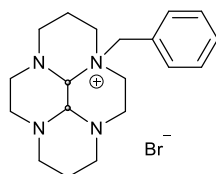
Methyl side bridged cyclam (0.4g, 1.3mmol, compound 28) was dissolved in chloroform (40 ml) and added to a solution of GPTES (0.37g, 1.3 mmol) in chloroform (40 ml). The mixture was stirred for one hour at RT before being refluxed for 72 hours. The solvent was removed to produce a reddish oil in chloroform, which was washed with de-ionised water, dried and evaporated to produce a reddish oil, compound 29.

^1H NMR (CDCl_3): δ 0.5 (m), 1.15 (t), 1.6 (m), 2.05-2.14 (m), 2.41-2.54 (m), 3.20 (td), 3.35-3.48(m), 3.74(t).

^{13}C NMR (CDCl_3): δ 9.6, 21.5, 26.2, 42.6, 47.6, 54.1, 59.4, 60.01, 61.5, 62.9, 74.6, 77.00.

MS: (ESI) m/z [M-I]. LRMS: calculated for $\text{C}_{25}\text{H}_{54}\text{N}_4\text{O}_5\text{Si}$: 518.90. Observed 519.4 (70%) and 797.9 (23%).

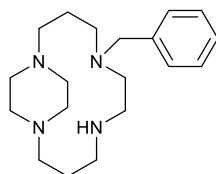
6.3.30. Synthesis of 3a-benzyl-decahydro-3a,5a,8a,10a-tetraazapyrenium bromide (Compound 33)



cis-3a, 5a, 8a, 10a-Tetraazaperhydropyrene (1.27g, 5.71 mmol, compound 26) was dissolved in dry acetonitrile (40 ml). Benzyl bromide (2.7ml, 22.7mmol) was added dropwise to the prepared solution and the reaction stirred for 16 hours at RT. The mixture was filtered, white precipitate collected, washed with diethyl ether (4x 70 ml) and dried to give white solid (1.56g, compound 33).

^1H NMR: (D_2O) δ 7.58-7.50 (m, 5H), 5.02 and 4.75 (2H, $\text{CH}_2\text{-Ar}$), 4.33 (br s, 1H, CH), 4.17 (td, 1H), 3.65 (br s, 1H, CH), 3.56-3.43 (m, 2H, $\text{CH}_2\text{-N}$), 3.32-3.19 (m, 2H, $\text{CH}_2\text{-N}$), 3.12-2.95 (m, 7H, $\text{CH}_2\text{-N}$), 2.61 (td, 1H, $\text{CH}_2\text{-N}$), 2.47-2.40 (m, 2H, $\text{CH}_2\text{-}\beta\text{-N}$), 2.28-2.09 (m, 3H, $\text{CH}_2\text{-N}$), 1.74 (br d, 1H, $\text{CH}_2\text{-}\beta\text{-N}$), 1.43 (br d, 1H, $\text{CH}_2\text{-}\beta\text{-N}$).

6.3.31 Synthesis of 4-benzyl-1-, 4-, 8-, 11-tetraazabicyclo[10.2.2]hexadecane (Compound 34)

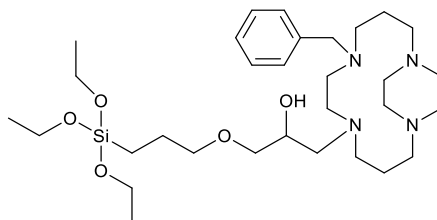


3a-Benzyl-decahydro-3a,5a,8a,10a-tetraazapyrenium bromide (1.35g, 3.43 mmol, compound 33) was dissolved in ethanol (80 ml). The mixture was cooled to 0°C before sodium borohydride (3.21g, 84.9 mmol) over 90 minutes whilst stirring. The cooled mixture was stirred for a further 30 minutes before stirring overnight at RT. The mixture was refluxed for 3 hours before being stirred for overnight. Deionised water (20 ml) was added to decompose the excess NaBH₄, solvents were removed to give a white powder. Water (50ml) was added to the powder followed by addition of KOH to adjust the pH to 14. The mixture was extracted with benzene (4x 40ml) and the organic phases were combined, dried and concentrated to yield an oily product (0.5g, compound 34).

¹H NMR: (CDCl₃): δ 7.20-7.35 (m, 5H), 3.69 (s, 2H, CH₂-Ar), 3.22-3.31 (m, 1H, CH₂-N), 2.98-3.05 (m, 2H, CH₂-N), 2.90-2.99 (m, 2H, CH₂-N), 2.74 (t, 1H, CH₂-N), 2.65-2.54 (m, 2H, CH₂-N), 2.53 (s, 2H, CH₂-N), 2.48-2.31 (m, 5H, CH₂-N), 2.29-1.98 (m, 5H, CH₂-N), 1.92-1.64 (m, 2H, CH₂-β-N), 1.50-1.31 (m, 2H, CH₂-β-N).

MS: (ESI) m/z [M-I]. LRMS: calculated for C₁₉H₃₂N₄: 316.48 observed 316.434.

6.3.32. Attempted synthesis of siloxane ligand on benzyl side bridged cyclam: Compound 35



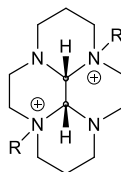
Benzene side bridged cyclam (0.4g, 1.3 mmol, compound 34) was dissolved in chloroform (2 ml) and added to a solution of GPTES (0.37 g, 1.3 mmol) in chloroform (2 ml). The mixture was stirred for one hour at RT before being refluxed for 72 hours. The solvent was removed to produce dark oil. The product in chloroform, washed with deionised water, dried and evaporated to produce a product as black reddish oil (0.88g, compound 35).

¹H NMR ((CDCl₃): δ 0.5 (m), 1.15 (t), 1.6 (m), 2.05-2.14 (m), 2.41-2.54 (m), 3.20 (td), 3.35-3.48(m), 3.74(t).

¹³C NMR (CDCl₃): δ 9.6, 21.5, 26.2, 42.6, 47.6, 54.1, 59.4, 60.01, 61.5, 62.9, 74.6, 77.00.

MS: (ESI) m/z [M-I]. LRMS: calculated for C₃₁H₅₈N₄O₅Si: 594.90. Observed 595.1 (100%).

6.3.33. Synthesis of (10ba,10ca)-Decahydro-3a,8a-bis(phenylmethyl)-1H,6H-3a,5a,-8a,10a-tetraazapyrenium Dibromide Monohydrate(3a.h2o) (Compound 39)

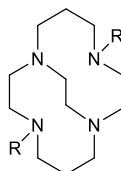


cis-3a, 5a, 8a, 10a-Tetraazaperhydropyrene (9.04g, 40.6mmol, compound 26) was dissolved in MeCN (200 ml). Benzyl bromide (100g, 0.585 mol) was added to the solution and the mixture was stirred for 14 days at rt. The mixture was filtered, the white precipitate washed with MeCN (2 x 40 ml), CH₂Cl₂ (2x70ml), collected and dried to yield white powder (20.2 g, 88%, compound 39).

¹H NMR: (D₂O) δ 1.81-1.91 (dm, 2H, C-CH-C), 2.15-2.34 (qm, 2H, C-CH-C), 2.76 (td, 2H), 3.12-3.25 (dm, 4H), 3.34-3.60 (m, 6H), 3.70 (td, 2H), 4.38 (td, 2H), 4.70 and 5.23 (AB, 4H), 5.04 (s, 2H, CH), 7.35-7.75 (m, 10H).

¹³C NMR: (D₂O) δ 18.8, 46.7, 47.5, 51.9, 61.1, 63.1, 77.5, 125.5, 130.2, 132.2, 134.0.

6.3.34. Synthesis of 4,11-Dibenzyl-1-, 4-, 8-, 11-tetraazabicyclo[6.6.2]hexadecane. Compound 40a

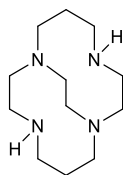


(10ba,10ca)-Decahydro-3a,8a-bis(phenylmethyl)-1H,6H-3a,5a,-8a,10a-tetraazapyrenium dibromide monohydrate (20.25 g, 34.77 mmol, compound 39) was suspended in EtOH (1000 ml). NaBH₄ (66.70g, 1.76 mol) was added dropwise in small portions over 120 minutes. The mixture stirred for 16 days at R.T. The mixture was cooled to 2°C and HCl (3 M, 800ml) was added dropwise over 90 minutes. The mixture was concentrated and dried to produce a white powder. Deionised water (500ml) was added to the white powder with stirring and the mixture pH was raised to 14 by adding KOH pellets with cooling. The basic phase was washed with benzene (8 x 250 ml), the combined organic extracts were dried with MgSO₄ and the solution was concentrated *in vacuo* to yield (8.2g, compound 40).

¹H NMR: (CDCl₃) δ 1.29-1.43 (m, 2H, C-CH-C), 1.48-1.63 (m, 2H, C-CH-C), 2.24-2.51 (m, 12H), 2.36-2.52 (m, 2H), 2.83 (ddd, 2H) 3.09-3.27 (m, 2H), 3.15 and 3.76 (m, 4H), 3.94 (ddd, 2H), 7.13-7.43 (m, 10H).

¹³C NMR: (CDCl₃) δ 27.03, 51.0, 53.1, 55.3, 56.1, 56.2, 59.1, 126.5, 128.0, 128.9, 141.0

6.3.35. Synthesis of 1-, 4-, 8-, 11-tetraazabicyclo[6.6.2]hexadecane (Compound 40b)



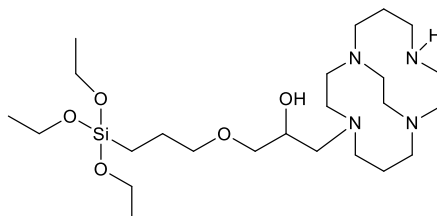
A solution of 4,11-dibenzyl-1,4,8,11-tetraazabicyclo [6.6.2] hexadecane (4.54g, 11.17 mmol, compound 39) in acetic acid (50 ml) was added to a suspension of palladium on carbon 10% in acetic acid in a Parr hydrogenation flask. The glass apparatus was filled with hydrogen and evacuated for four times and the mixture was shaken in the hydrogenator for 21 hours under H₂. The flask contents were filtered through super hydro flow powder and the powder was washed with glacial acetic acid (5 x 30 ml). The filtrate was concentrated *in vacuo* to produce light yellow oil. Water (50 ml) was added to the oil, the solution pH was raised to 14 by KOH pellets under cooled reaction and the mixture was extracted with benzene (6x 25ml). The organic phases were combined, dried and evaporated to provide a colourless oil (1.2g, compound 40).

¹H NMR: (C₆D₆) 1.16 (dtt, 2H), 1.53 (dtt, 2H), 2.07-2.26 (overlapping, 4H and m, 2H), 2.31 (ddd, 2H), 2.42-2.64 (m, 6H), 2.74-2.86 (m, 4H), 3.21 (ddd, 2H), 3.59 (br s, 2H).

¹³C NMR (C₆D₆) δ 24.9, 47.4, 50.7, 52.4, 56.1, 59.0.

MS: (ESI) m/z [M-I]. LRMS: calculated for C₁₂H₂₆N₄: 226.2157 observed 226.334.

6.3.36. Synthesis of siloxane ligand on cross-bridged cyclam (Compound 41)



A solution of cross-bridged cyclam (0.4g, 1.3mmol, compound 41) in chloroform (40 ml) was added to a solution of GPTES (0.37g, 1.3 mmol) in chloroform (40ml). The mixture was stirred for one hour at RT before being refluxed for 72 hours. The solvent was removed to yield a dark reddish oil. This product was redissolved in chloroform, washed with de-ionised water, dried and evaporated to produce a red oil product (8.07g, compound 41).

¹H NMR ((CDCl₃): δ 1.30 (m), 1.705 (m), 2.08 (td), 2.20-2.30 (m), 2.35-2.8 (m), 2.98-3.02 (m), 3.22-3.32 (m), 3.65(s).

¹³C NMR (CDCl₃): δ 23.00, 26.2, 48.1, 50.5, 51.1, 54.9, 55.1, 55.4, 56.8, 56.9, 76.6, 77.0, 77.3.

MS: (ESI) m/z [M-I]. LRMS: calculated for C₂₄H₅₂N₄O₅Si: 504.78 observed 504.78(100%) and 783.6 (45%)..

6.3.37. Synthesis of Transition Metal Complexes

6.3.37.A. General complexation procedure

The selected ligand (100mg) was dissolved in either dry ethanol or dry methanol (20 ml). Another metal salt solution was prepared with 1.1 molar equivalents of metal salts per macrocyclic ligand. The metal salt was dissolved in either dry ethanol or dry methanol (20 ml) and was added dropwise in the ligand solution over 15 minutes under N₂. The mixture stirred for 30 minutes and heated gradually to reflux. The refluxing process continued for a further 2 hours, it was then cooled down to R.T and stirred for 2 hours. The solvent was removed under reduced pressure with a rotary evaporator until ca. 2ml was left. This was purified via size exclusion chromatography.

6.3.37.B. Size Exclusion Chromatography

Sephadex (LH20) was soaked in methanol for at least 3 hours prior of being used. Sample purification were carried out in two steps: firstly, a small prepurification column in a Pasteur pipette fitted with glass wool was run with methanol eluent to remove the majority of excess metal salt; secondly, a column of approximately 15cm (height) by 1cm (diameter) was run with methanol eluent to remove trace metal salt. Individually coloured bands were collected and concentrated *in vacuo* to give pure metal complexes.

6.3.37.1. Synthesis of [Zn(CH₃CO₂)₂] siloxane cyclam:

Ligand siloxane cyclam (compound 22) in dry ethanol. Zn(CH₃CO₂)₂(40 mg) in dry ethanol. See procedure 6.3.37.A. The mixture was purified via size exclusion chromatography to give the yield of 133 mg (Compound23, see procedure 6.3.37.B).

¹H NMR (CDCl₃): δ 1.13 (t), 1.5-1.63 (m), 1.8 (s), 2.38-2.87 (m), 3.66 (t), 7.2 (s). ¹³C NMR (CDCl₃): δ 18.4, 25.1, 47.7, 50.01, 58.2.

Mass spectrometry, expected peak 541.1. Found 541.3 (100%) and 587.3 (75%).

Elemental analysis:

Elements	Expected value %	Found value %
C	48.83	49.1
H	8.75	8.59
N	10.35	10.28
Zn	12.08	11.95
Si	5.19	5.15

6.3.37.2 Synthesis of [Cu(CH₃CO₂)₂] for siloxane cyclam:

Siloxane cyclam, (compound 22) was dissolved in dry ethanol. (Cu(CH₃CO₂)₂) (41 mg) in dry ethanol (see procedure 6.3.37.A). The mixture was evaporated under reduced pressure via rotary evaporator and purified via size exclusion chromatography to give the yield of 128 mg (Compound 25, see procedure 6.3.37.B).

Mass spectrometry, expected peak 540.4. Found 540.4 (100%) and 757.8 (25%).

Elemental analysis:

Elements	Expected value %	Found value %
C	49.00	49.1
H	8.87	8.77
N	10.39	10.40
Cu	11.7	11.54
Si	5.21	5.20

6.3.37.3 Synthesis of [Ni(CH₃CO₂)₂] for siloxane cyclam:

Siloxane cyclam (compound 22) in dry ethanol. (Ni(CH₃CO₂)₂) (40 mg) in dry ethanol (see procedure 6.3.37.A). The mixture was evaporated under reduced pressure via a rotary evaporator, purified via size exclusion chromatography to give the yield (150 mg compound 24, see procedure 6.3.37.B).

¹H NMR ((CDCl₃): δ 1.06 (t), 1.5-1.63 (m), 1.8 (s), 2.38-2.87 (m), 3.20 (t), 4.7 (s).

¹³C NMR (CDCl₃): δ 18.4, 25.1, 47.7, 50.01, 58.2.

Mass spectrometry, expected peak 535.4. Found 535.4 (100%) and 581.3 (60%).

Elemental analysis:

Elements	Expected value %	Found value %
C	49.44	49.20
H	8.68	8.72
N	10.48	10.45
Ni	10.98	10.90
Si	5.26	5.22

6.3.37.4 Synthesis of [Cu(CH₃CO₂)₂] for cross-bridged siloxane cyclam

Cross bridged siloxane cyclam (compound 41) was dissolved in dry ethanol (15ml). Cu (CH₃CO₂)₂ (59.4 mg) in dry ethanol (see procedure 6.3.37.A). The mixture then was evaporated under reduced pressure via rotary evaporator and purified via size exclusion chromatography to give the yield of 149 mg (Compound44, see procedure 6.3.37.B).

Mass spectrometry, expected peak 568.1. Found 378.2 (100%) and 770.4 (80%).

Elemental analysis:

Elements	Expected value %	Found value %
C	50.81	50.77
H	9.06	9.02
N	9.88	9.86
Cu	11.20	11.13
Si	4.95	4.93

6.3.37.5 Synthesis of [Zn(CH₃CO₂)₂] cross-bridged siloxane cyclam:

Cross-bridged siloxane cyclam (compound 41, 150 mg) was dissolved in dry ethanol. (Zn (CH₃CO₂)₂) (58.6 mg) was dissolved in dry ethanol, see procedure 6.3.37.A. The mixture then was evaporated under reduced pressure via rotary evaporator and purified via size exclusion chromatography to give the yield of 188 mg (Compound 42, see procedure 6.3.37.B).

Mass spectrometry, expected peak 567.2. Found 567.2 (67%) and 657.4 (100%) and 771.5 (60%).

Elemental analysis:

Elements	Expected value %	Found value %
C	50.65	50.50
H	9.03	9.01
N	9.84	9.81
Zn	11.49	11.52
Si	4.93	4.93

6.3.37.6 Synthesis of [Ni(CH₃CO₂)₂] for cross-bridged siloxane cyclam:

Cross-bridged siloxane cyclam (compound 41) was dissolved in dry ethanol. (Ni (CH₃CO₂)₂) (63.6 mg) was dissolved in dry ethanol, see procedure 6.3.37.A. The mixture was filtered, washed with ethanol (2 x 20ml) and the precipitate was collected and the ethanol washing solvent was evaporated under reduced pressure. The mixture then was evaporated under reduced pressure via rotary evaporator and purified via size exclusion chromatography to give the yield of 201 mg (Compound 43, see procedure 6.3.37.B).

Mass spectrometry, expected peak 561.3. Found 561.3 (100%) and 651.4 (80%) and 765.5 (60%).

Elemental analysis:

Elements	Expected value %	Found value %
C	51.25	51.15
H	9.14	9.05
N	9.96	9.88
Ni	10.44	10.42
Si	4.99	4.96

6.3.38. Reacting NPs with siloxane macrocycles

6.3.38.1. NPs siloxane cyclam

NPs were suspended in toluene (300 mg/75 ml, compound 8). Si-Cyclam (0.3g, Compound 22), triethylamine (10ml) and deionised water (4ml) were added successively in a dropwise manner to the NPs suspension. The mixture was stirred for 48 hours under Ar. Pentane (10 ml) was added and the precipitated NPs were isolated via an external magnet for washing. The pentane washing procedure was repeated three times, and the final NPs were dried and stored under Ar (0.288 g, compound 45).

NTA: Mode 27 nm, mean 44 nm. See Figure B14.

Elemental analysis (CHN)	
C	21.15%
H	3.65%
N	4.46%

6.3.38.2. NPs cross-bridged siloxane cyclam

NPs were suspended in toluene (300 mg/ 75ml, compound 8). Si-CB-Cyclam (0.3g, Compound 41), triethylamine (10ml) and deionised water (4ml) were added successively in a dropwise manner to the NPs suspension. The mixture stirred for 48 hours under Ar. Pentane, (10 ml) was added and the precipitated NPs were isolated using external magnet for washing. The pentane washing procedure was repeated three times, and the final NPs yields were dried and stored under Ar (0.314 g, compound 46).

NTA: Mode 25 nm, mean 47 nm. See Figure B15.

Elemental analysis (CHN)	
C	21.66%
H	5.26%
N	3.45%

6.3.39. Metals Complexation NPs

6.3.39.A. General procedure for metals complexation to NPs-siloxane macrocycles

NPs with the attached siloxane macrocycle ligands (50 mg, compounds 45 and 46) were suspended in dry ethanol (30ml) with sonication for 20 minutes and shaken for a further 20 minutes. A solution of metal salts $\text{Zn}(\text{CH}_3\text{CO}_2)_2$, $\text{Cu}(\text{CH}_3\text{CO}_2)_2$ and $\text{Ni}(\text{CH}_3\text{CO}_2)_2$ (0.05 mmol) in dry ethanol (10 ml) were added to the prepared NPs suspension and shaken for 24 hours at R.T. The solids were isolated with a magnet and washed with absolute ethanol (x2) and de-ionised water (x2). The final powder was characterised by NTA, CHN and Optical emission ICP-OES (see section 2.2.4.2).

6.3.39.1 Complexing $\text{Ni}(\text{CH}_3\text{CO}_2)_2$ to NPs siloxane cyclam:

NPs with the attached siloxane cyclam (compound 45) were suspended in dry ethanol. ($\text{Ni}(\text{CH}_3\text{CO}_2)_2$ (9 mg) in dry ethanol (10 ml) was added to the NPs suspension, see procedure 6.3.39.A. A black powder was isolated (42 mg, compound 48).

NTA: Mode 75 nm, mean 101 nm, SD ± 40 nm. See Figure B16

Elemental analysis (ICP-OES and CHN)	
Fe	6.21%
Si	3.18%
Cu	0.00%
Ni	0.48%
Zn	0.00%
C	20.11%
H	3.45%
N	4.19%

6.3.39.2 Complexing Cu (CH₃CO₂)₂ with NPs-cross-bridged cyclam-siloxane

NPs with attached CB-cyclam (compound 46) were suspended in dry ethanol and mixed with a solution of (Cu(CH₃CO₂)₂) (9 mg) in dry ethanol, see procedure 6.3.39.A. The compound is a black powder (49 mg, compound 50).

NTA: Mode 102 nm, mean 160 nm, SD ±81 nm. See Figure B17

Elemental analysis (ICP-OES and CHN)	
Fe	5.56%
Si	2.033%
Cu	0.523%
Ni	0.00%
Zn	0.00%
C	20.98%
H	4.85%
N	3.01%

6.3.39.3 Complexing Cu(CH₃CO₂)₂ with NPs-siloxane cyclam

NPs with attached cyclam (compound 45) was suspended in dry ethanol and mixed a solution of Cu(CH₃CO₂)₂ (9 mg) in dry ethanol, see procedure 6.3.39.A. A final yield of a black powder (40 mg, compound 47).

NTA: Mode 95 nm, mean 121 nm, SD ±79 nm. See Figure B18

Elemental analysis (ICP-OES)	
Fe	6.67%
Si	4.17%
Cu	0.418%
Ni	0.00%
Zn	0.00%
C	20.88%
H	3.48%
N	4.21%

6.3.39.4 Complexing Zn(CH₃CO₂)₂ with NPs-cross-bridged cyclam-siloxane:

NPs with attached CB-cyclam (compound 46) were suspended in dry ethanol (30ml) and mixed with a solution of Zn(CH₃CO₂)₂ (9 mg) in dry ethanol, see procedure 6.3.39.A. A black powder was isolated (47mg, compound 52).

NTA: Mode 85 nm, mean 156 nm, SD ±94 nm. See Figure B19

Elemental analysis (ICP-OES)	
Fe	1.189%
Si	1.87%
Cu	0.00%
Ni	0.00%
Zn	7.084%
C	20.9%
H	4.91%
N	3.11%

6.3.39.5 Complexing Ni(CH₃CO₂)₂ with NPs-cross-bridged cyclam-siloxane:

NPs with attached CB-cyclam, (compound 46) were suspended in dry ethanol (30ml) and mixed with a solution of Ni(CH₃CO₂)₂ (9 mg) in dry ethanol, see procedure 6.3.39.A1. A black powder was isolated (47mg, compound 51).

NTA: Mode 72 nm, mean 92 nm, SD ±40 nm. See Figure B20

Elemental analysis (ICP-OES)	
Fe	5.58%
Si	3.41%
Cu	0.00%
Ni	0.613%
Zn	0.00%
C	20.99%
H	5.02%
N	3.13%

6.3.39.6 Complexing Zn(CH₃CO₂)₂ with NPs-cyclam-siloxane:

NPs attached cyclam (compound 45) were suspended in dry ethanol (30ml) and mixed with a solution of Zn(CH₃CO₂)₂ (9 mg) in dry ethanol, see procedure 6.3.39.A. A black powder was isolated (45 mg, compound 49).

NTA: Mode 108 nm, mean 161 nm, SD ±106 nm. See Figure B21

Elemental analysis (ICP-OES)	
Fe	0.98%
Si	3.83%
Cu	0.00%
Ni	0.00%
Zn	9.39%
C	20.88%
H	3.50%
N	4.20%

6.3.39.7 Bare nanoparticles complexed with (Cu (CH₃CO₂)):

Bare NPs (compound 8) were suspended in dry ethanol and mixed with a solution of Cu(CH₃CO₂)₂ (9 mg) in dry ethanol, see procedure 6.3.39A. A black powder was isolated (45 mg, compound 53).

Elemental analysis (ICP-OES)	
Fe	62.1%
Si	0.00%
Cu	0.146%
Ni	0.00%
Zn	0.00%
C	0.6%
H	1.02%
N	0.31%

6.3.39.8 Bare nanoparticles complexed with Ni(CH₃CO₂)₂

Bare NPs (compound 8) were suspended in dry ethanol and mixed with a solution of Ni(CH₃CO₂)₂ (9mg) in dry ethanol, see procedure 6.3.39.A. A black powder was isolated (43 mg, compound 54).

Elemental analysis (ICP-OES)	
Fe	65.7%
Si	0.00%
Cu	0.00%
Ni	0.13%
Zn	0.00%
C	0.6%
H	1.01%
N	0.28%

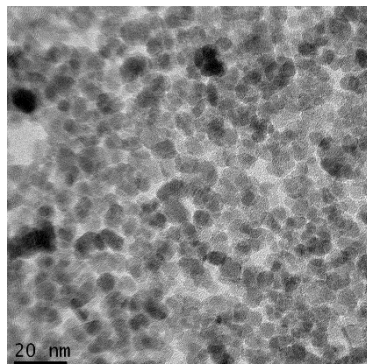
6.3.39.9 Bare nanoparticles complexed with (Zn (CH₃CO₂)₂

Bare NPs (compound 8) were suspended in dry ethanol (30ml) and mixed with a solution of Zn(CH₃CO₂)₂ (9 mg) in dry ethanol, see procedure 6.3.39.A. A black powder was isolated (40 mg, compound 55).

Elemental analysis (ICP-OES)	
Fe	59.9%
Si	0.00%
Cu	0.00%
Ni	0.13%
Zn	0.36%
C	0.6%
H	1.00%
N	0.25%

Appendix:

Figure A1 TEM for compound 1



Figures A2 TEM for compounds 2, 3 and 4

A2a (compound 2)

A2b (Compound 3)

A2c (Compound 4)

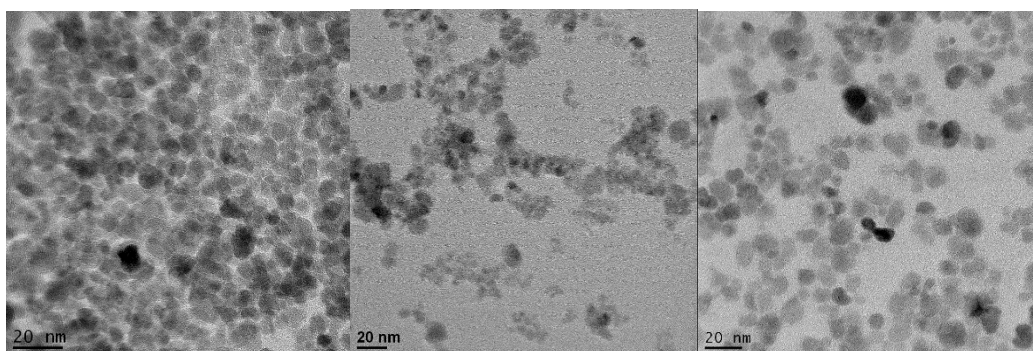


Figure A3 TEM for compound 5

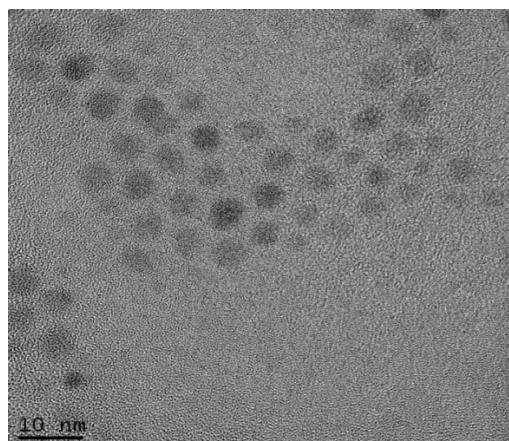


Figure A4 TEM for compound 6

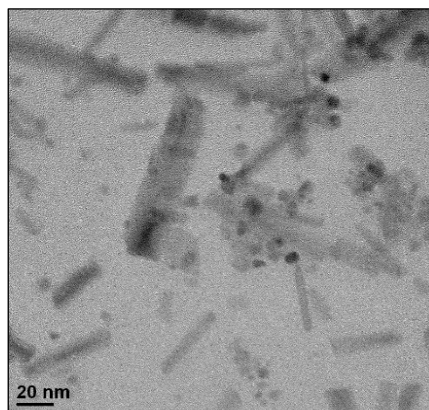


Figure A5 TEM for compound 7

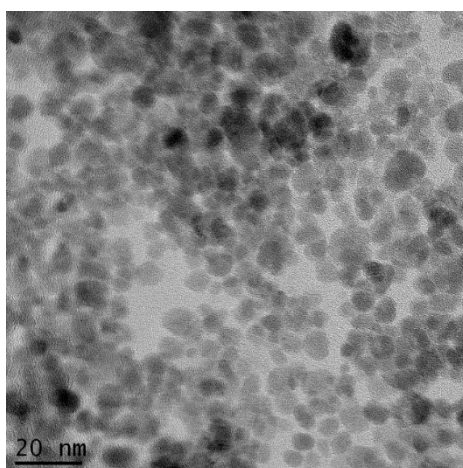


Figure A6 TEM for compound 8

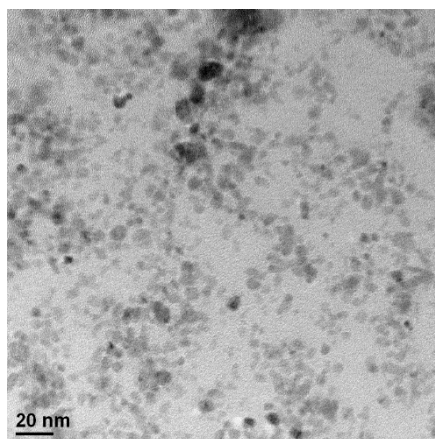


Figure A7 TEM for compound 12

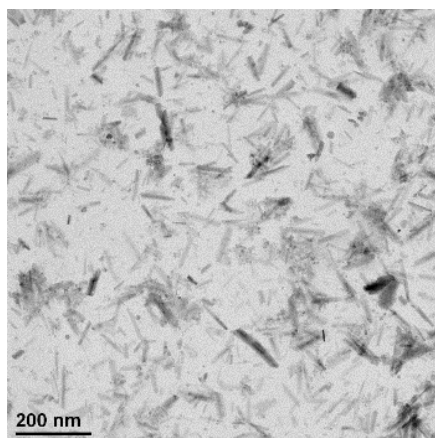


Figure A8 TEM for compound 14

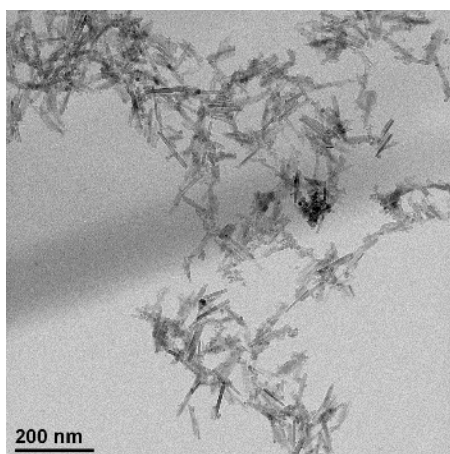


Figure A9 TEM for compound 15

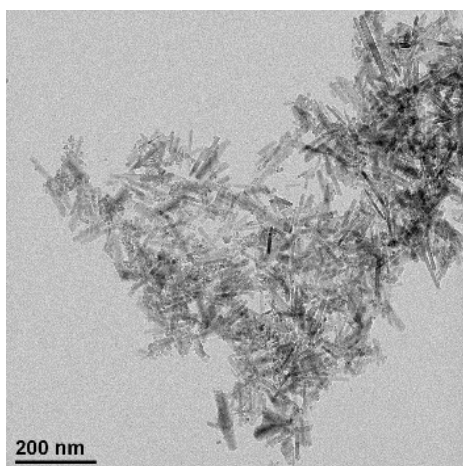


Figure A10 TEM for compound 16

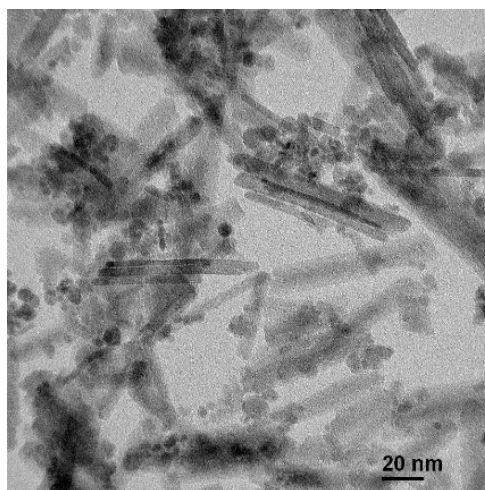


Figure B1 NTA for compound 1

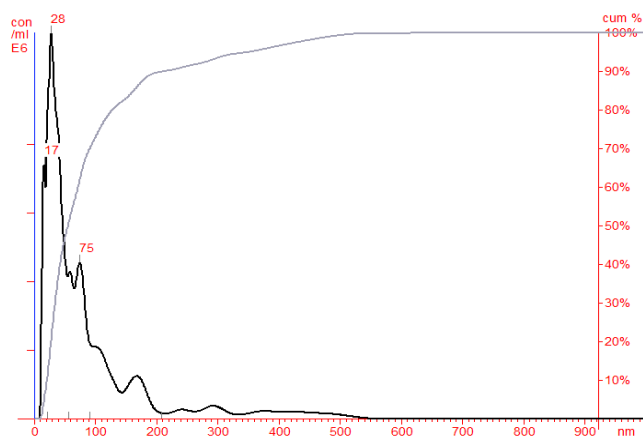


Figure B2 NTA for compound 2

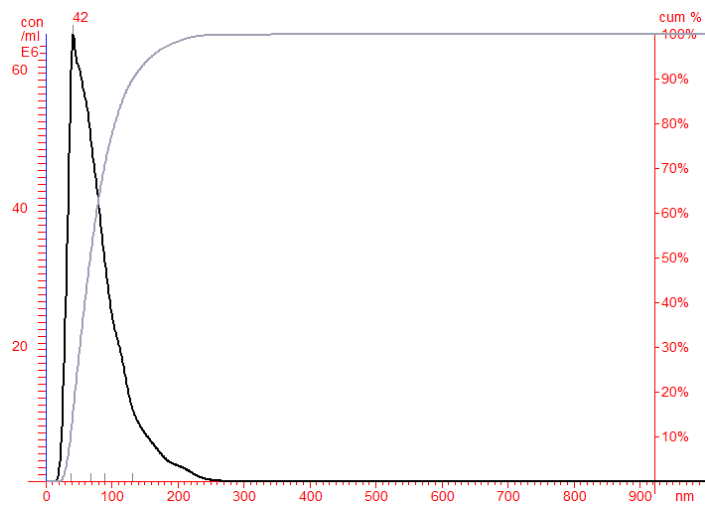


Figure B3 NTA for compound 3

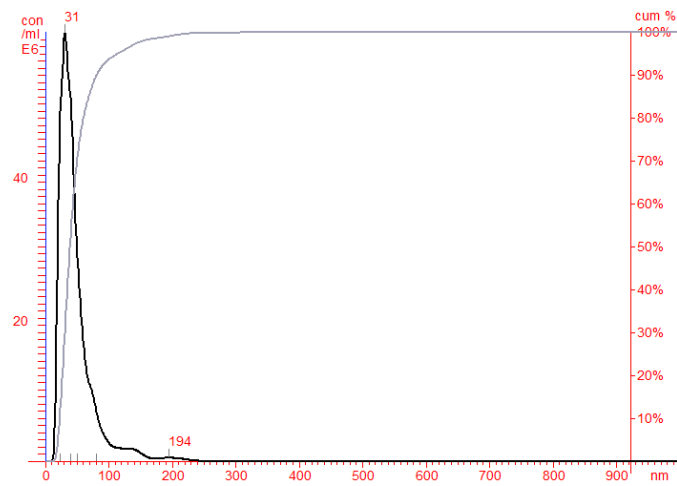


Figure B4 NTA for compound 4

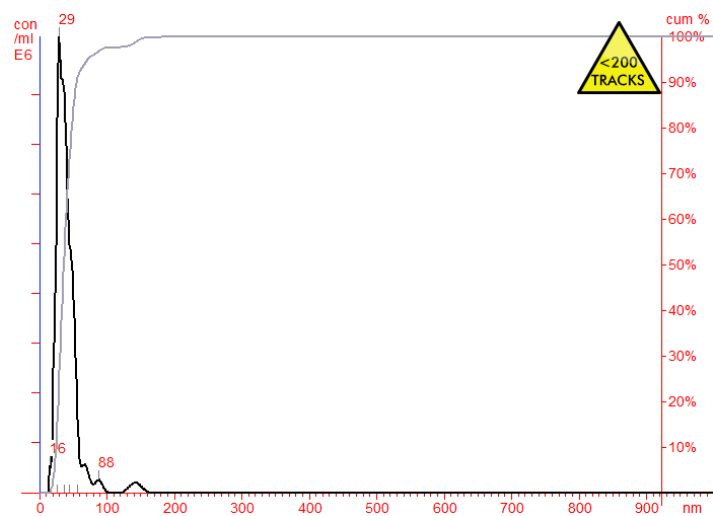


Figure B5 NTA for compound 5



Figure B6 NTA for compound 6

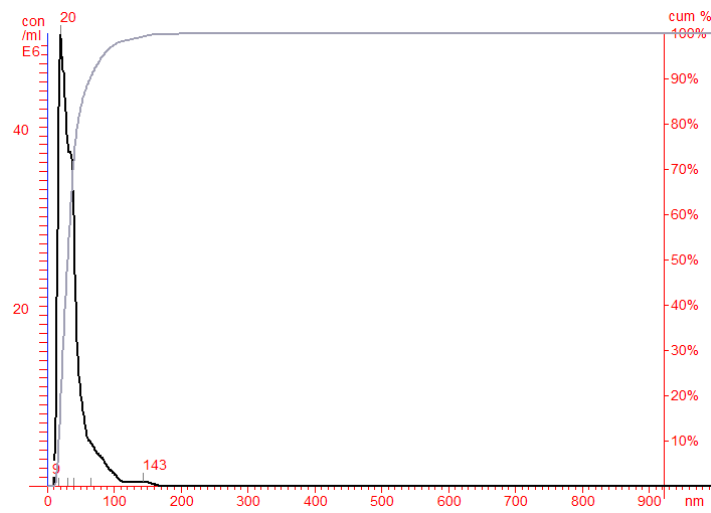


Figure B7 NTA for compound 7

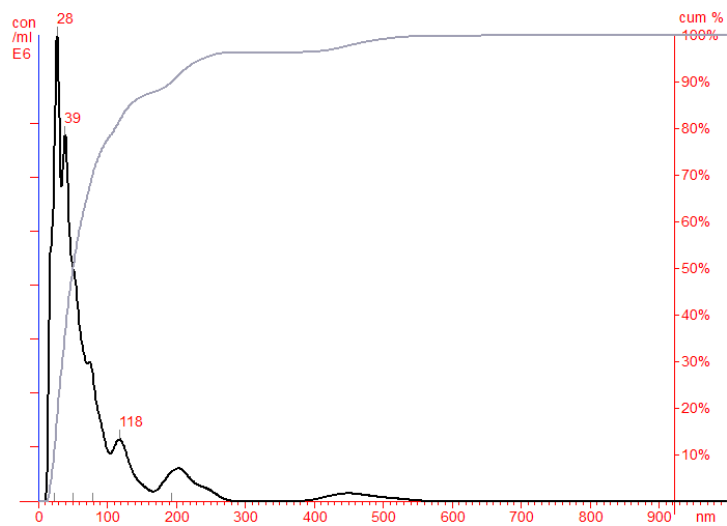


Figure B8 NTA for compound 8

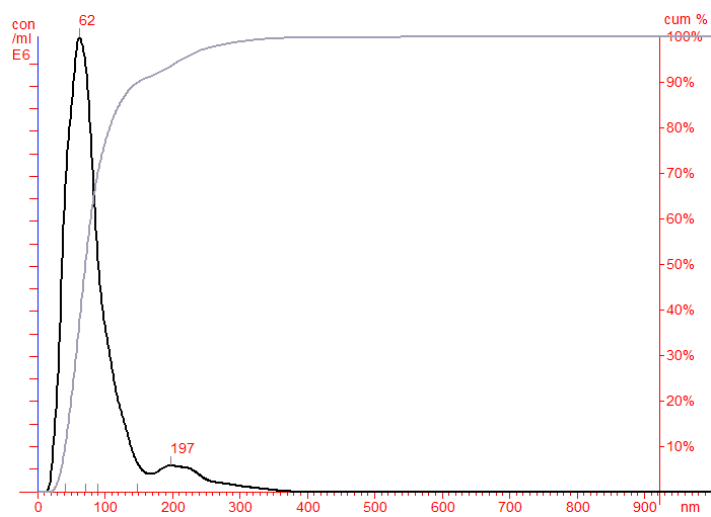


Figure B9 NTA for compound 12

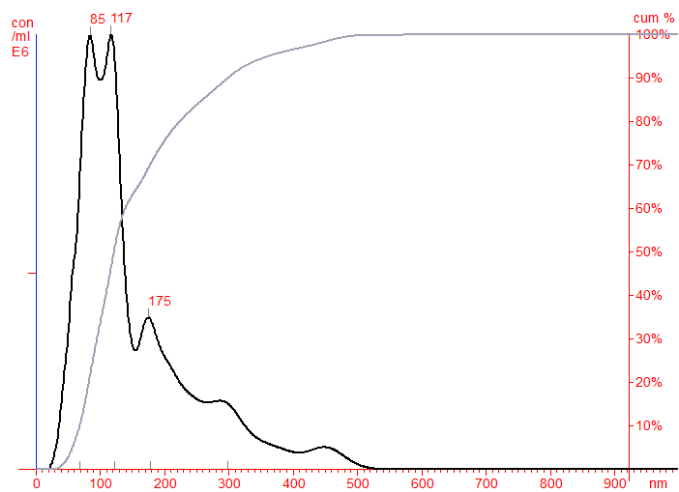


Figure B10 NTA for compound 14

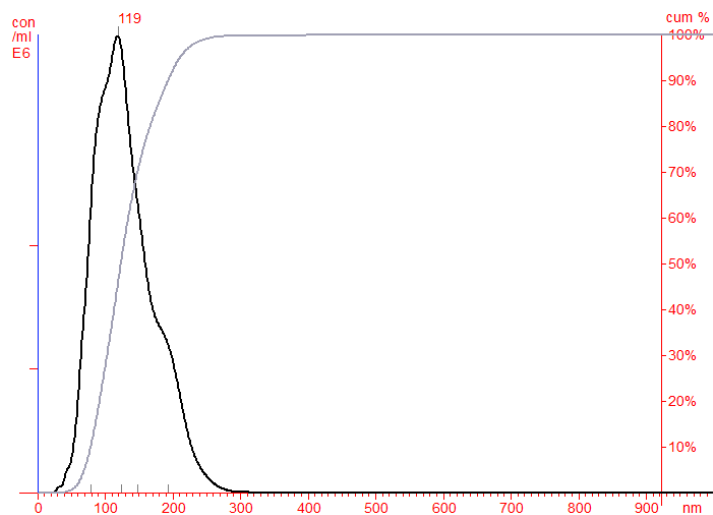


Figure B11 NTA for compound 15

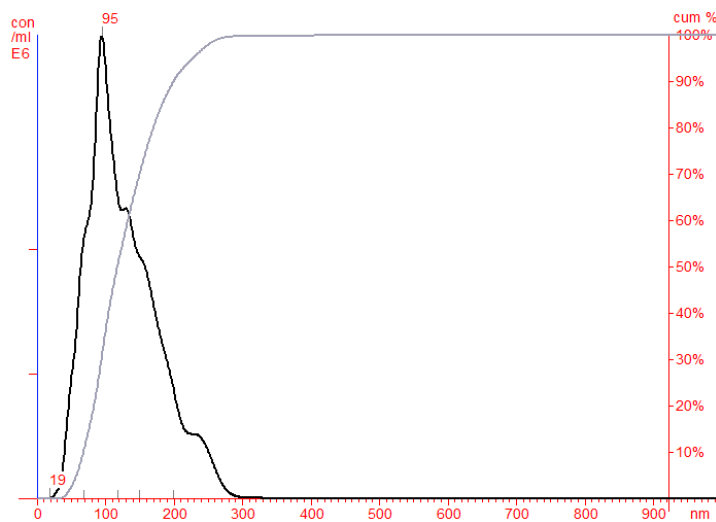


Figure B12 NTA for compound 16

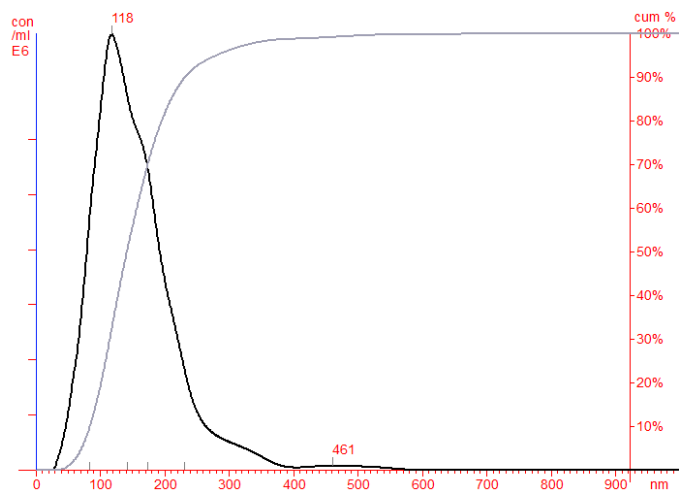


Figure B13 NTA for compound 17

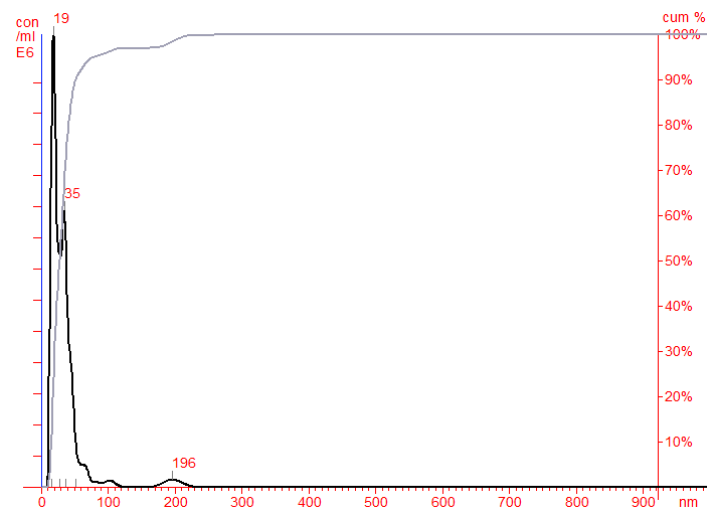


Figure B14 NTA for compound 45

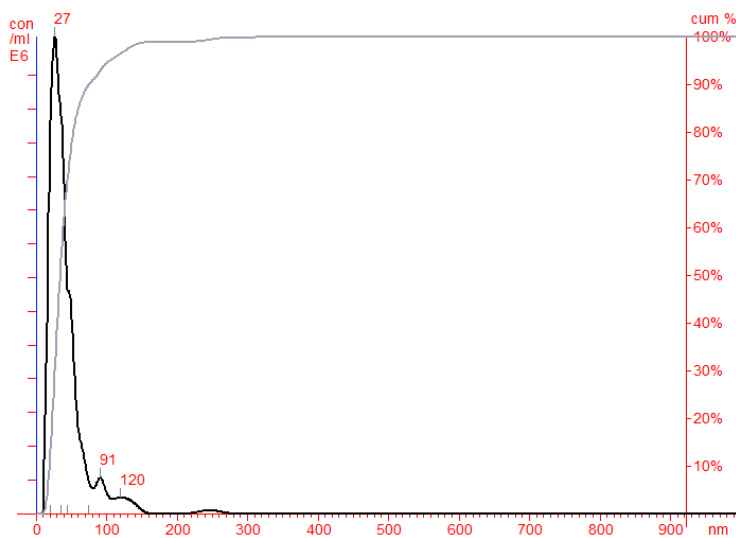


Figure B15 NTA for compound 46

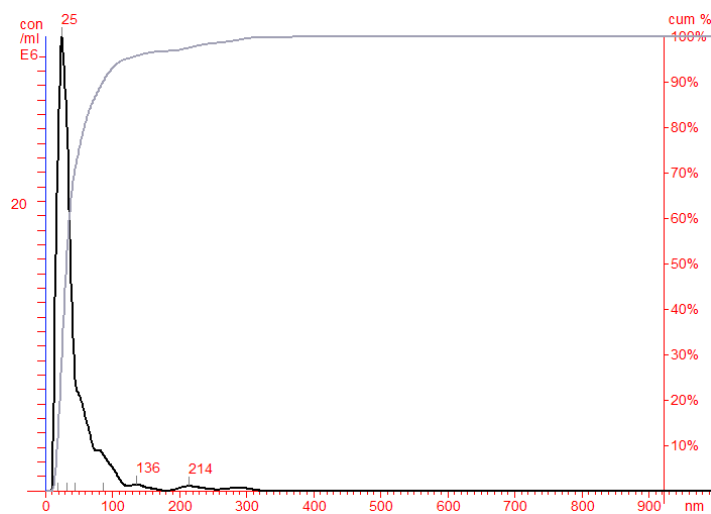
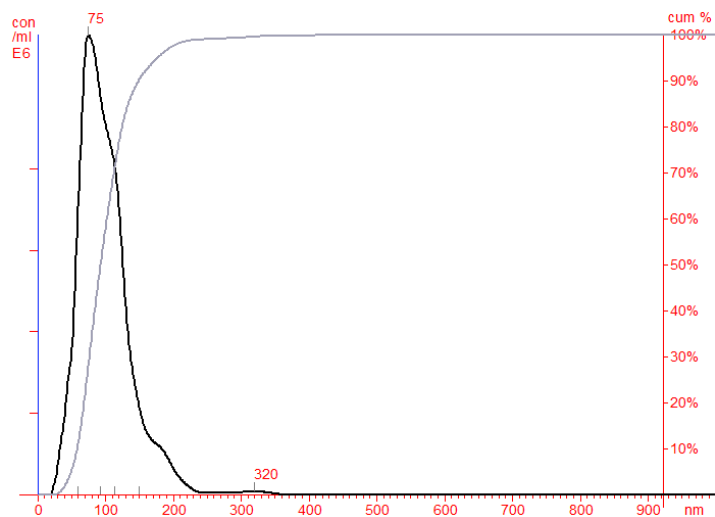
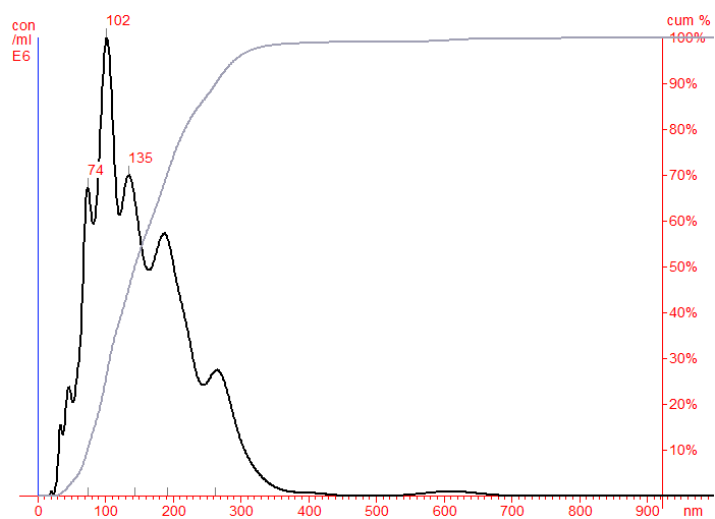


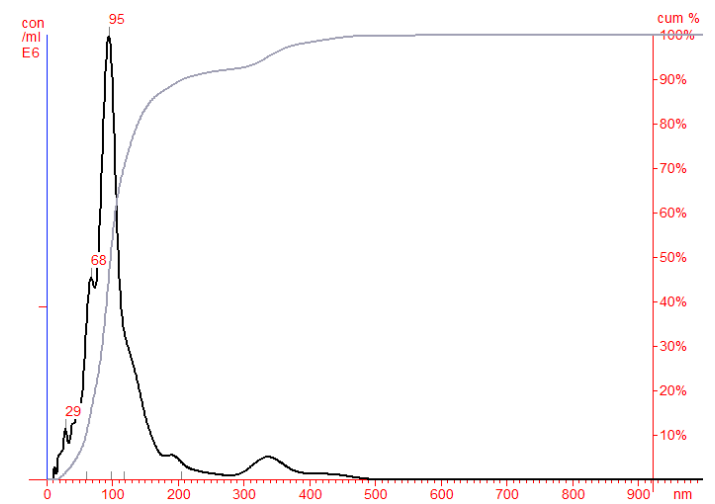
Figure B16 NTA for compound 48



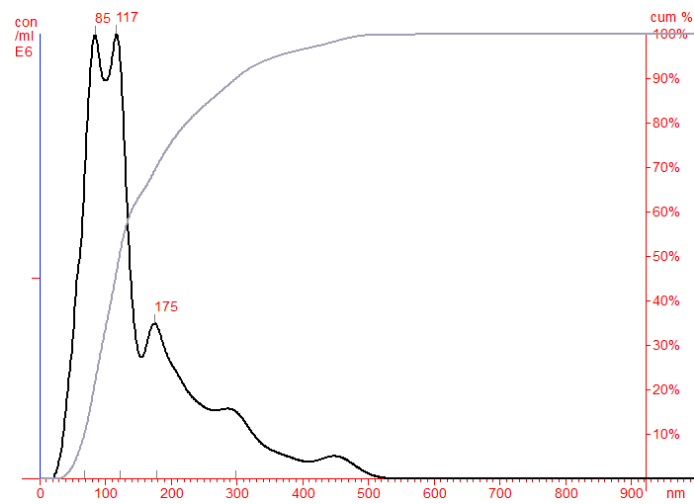
FigureB17 NTA for compound 50



FigureB18 NTA for compound 47



FigureB19 NTA for compound 52



FigureB20 NTA for compound 51

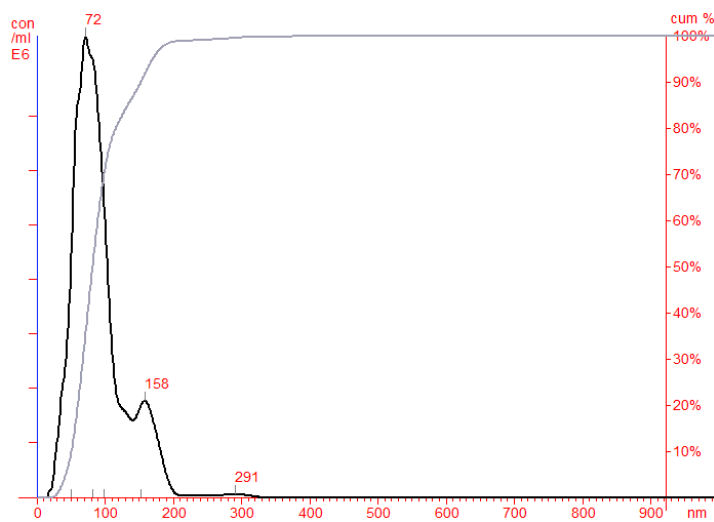
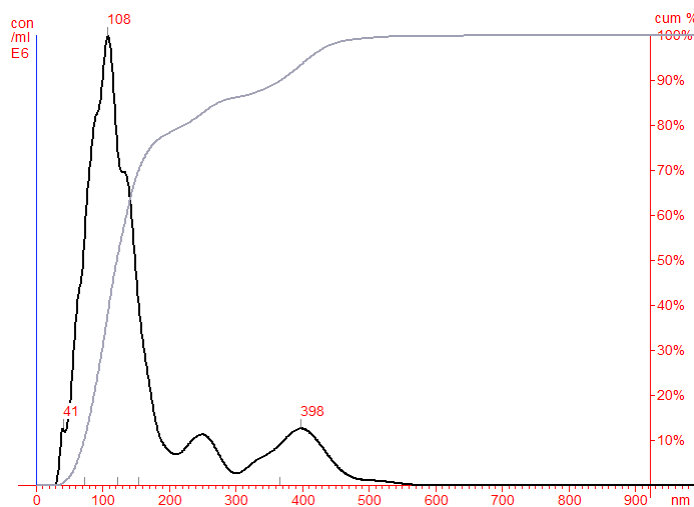


Figure B21 NTA for compound 49



References

1. Padmanabhan, P.; Kumar, A.; Kumar, S.; Chaudhary, R. K.; Gulyas, B., *Acta Biomaterialia* **2016**, 41, 1-16.
2. Kim, E. E., *Korean Journal of Radiology* **2003**, 4, 201-210.
3. Massoud, T. F.; Gambhir, S. S., *Genes Dev.* **2003**, 17, 545-580.
4. Weinstein, J. S.; Varallyay, C. G.; Dosa, E.; Gahramanov, S.; Hamilton, B.; Rooney, W. D.; Muldoon, L. L.; Neuwelt, E. A., *J. Cereb. Blood Flow Metab.* **2010**, 30, 15-35.
5. Chertok, B.; Moffat, B. A.; David, A. E.; Yu, F. Q.; Bergemann, C.; Ross, B. D.; Yang, V. C., *Biomaterials* **2008**, 29, 487-496.
6. Thiesen, B.; Jordan, A., *Int. J. Hyperthermia* **2008**, 24, 467-474.
7. Cromer Berman, S. M.; Walczak, P.; Bulte, J. W. M., *Wiley Interdisciplinary Reviews: Nanomedicine and Nanobiotechnology* **2011**, 3, 343-55.
8. Li, K. C. P.; Pandit, S. D.; Guccione, S.; Bednarski, M. D., *Biomedical Microdevices* **2004**, 6, 113-116.
9. Torchilin, V. P., *Adv. Drug Del. Rev.* **2006**, 58, 1532-1555.
10. Alivisatos, A. P., *Abstracts of Papers of the American Chemical Society* **1997**, 213, 454-PHYS.
11. Kraitchman, D. L.; Heldman, A. W.; Atalar, E.; Amado, L. C.; Martin, B. J.; Pittenger, M. F.; Hare, J. M.; Bulte, J. W. M., *Circulation* **2003**, 107, 2290-2293.
12. Walczak, P.; Ruiz-Cabello, J.; Kedziorek, D. A.; Gilad, A. A.; Lin, S.; Barnett, B.; Qin, L.; Levitsky, H.; Bulte, J. W. M., *Nanomedicine-Nanotechnology Biology and Medicine* **2006**, 2, 89-94.
13. Sun, C.; Lee, J. S. H.; Zhang, M., *Adv. Drug Del. Rev.* **2008**, 60, 1252-1265.
14. Laurent, S.; Forge, D.; Port, M.; Roch, A.; Robic, C.; Elst, L. V.; Muller, R. N., *Chem. Rev.* **2008**, 108, 2064-2110.
15. Gurzau, E. S.; Neagu, C.; Gurzau, A. E., *Ecotoxicol. Environ. Saf.* **2003**, 56, 190-200.
16. Caravan, P., *Chem. Soc. Rev.* **2006**, 35, 512-523.
17. Deichmann, R., Principles of MRI and Functional MRI. In *fMRI Techniques and Protocols*, Filippi, M., Ed. Humana Press Inc, Totowa, NJ, USA 2009; Vol. 41, pp 3-29.
18. Chavhan, G. B., *Pediatric Radiology* **2016**, 46, 740-747.
19. Helm, L., *Chimia* **2011**, 65, 696-698.
20. Na, H. B.; Song, I. C.; Hyeon, T., *Adv. Mater.* **2009**, 21, 2133-2148.
21. Truffault, L.; Choquet, B.; Konstantinov, K.; Devers, T.; Couteau, C.; Coiffard, L. J. M., *Journal of Nanoscience and Nanotechnology* **2011**, 11, 2413-2420.
22. Sun, G.; Hagooly, A.; Xu, J.; Nystrom, A. M.; Li, Z. C.; Rossin, R.; Moore, D. A.; Wooley, K. L.; Welch, M. J., *Biomacromolecules* **2008**, 9, 1997-2006.
23. Rossin, R.; Pan, D. P. J.; Qi, K.; Turner, J. L.; Sun, X. K.; Wooley, K. L.; Welch, M. J., *J. Nucl. Med.* **2005**, 46, 1210-1218.
24. Blower, P., *Dalton Trans.* **2006**, 1705-1711.
25. Hudson, H. M.; Larkin, R. S., *IEEE Trans. Med. Imaging* **1994**, 13, 601-609.
26. Miller, P. W.; Long, N. J.; Vilar, R.; Gee, A. D., *Angew. Chemie Int. Ed.* **2008**, 47, 8998-9033.
27. Sun, X.; Cai, W.; Chen, X., *Acc. Chem. Res.* **2015**, 48, 286-294.
28. Wadas, T. J.; Wong, E. H.; Weisman, G. R.; Anderson, C. J., *Chem. Rev.* **2010**, 110, 2858-2902.
29. Burke, B. P.; Clemente, G. S.; Archibald, S. J., *J. Labelled Comp. Radiopharm.* **2014**, 57, 239-243.
30. Fani, M.; Andre, J. P.; Maecke, H. R., *Contrast Media Mol. Imag.* **2008**, 3, 67-77.
31. Bhattacharyya, S.; Dixit, M., *Dalton Trans.* **2011**, 40, 6112-6128.
32. Bartholoma, M. D., *Inorg. Chim. Acta* **2012**, 389, 36-51.
33. Ramogida, C. F.; Orvig, C., *Chem. Commun.* **2013**, 49, 4720-4739.
34. Hofmann, M.; Maecke, H.; Borner, A. R.; Weckesser, E.; Schoffski, P.; Oei, M. L.; Schumacher, J.; Henze, M.; Heppeler, A.; Meyer, G. J.; Knapp, W. H., *Eur. J. Nucl. Med.* **2001**, 28, 1751-1757.
35. Henze, M.; Schuhmacher, J.; Hipp, P.; Kowalski, J.; Becker, D. W.; Doll, J.; Macke, H. R.; Hofmann, M.; Debus, J.; Haberkorn, U., *J. Nucl. Med.* **2001**, 42, 1053-1056.

36. Sainz-Esteban, A.; Prasad, V.; Schuchardt, C.; Zachert, C.; Carril, J. M.; Baum, R. P., *Eur. J. Nucl. Med. Mol. Imag.* **2012**, 39, 501-511.
37. Prasad, V.; Ambrosini, V.; Hommann, M.; Hoersch, D.; Fanti, S.; Baum, R. P., *Eur. J. Nucl. Med. Mol. Imag.* **2010**, 37, 67-77.
38. Blom, E.; Langstrom, B.; Velikyan, I., *Bioconjugate Chem.* **2009**, 20, 1146-1151.
39. Knetsch, P. A.; Petrik, M.; Rangger, C.; Seidel, G.; Pietzsch, H. J.; Virgolini, I.; Decristoforo, C.; Haubner, R., *Nucl. Med. Biol.* **2013**, 40, 65-72.
40. Al-Nahhas, A.; Win, Z.; Szyszko, T.; Singh, A.; Khan, S.; Rubello, D., *Eur. J. Nucl. Med. Mol. Imag.* **2007**, 34, 1897-1901.
41. Velikyan, I.; Maecke, H.; Langstrom, B., *Bioconjugate Chem.* **2008**, 19, 569-573.
42. Notni, J.; Hermann, P.; Havlickova, J.; Kotek, J.; Kubicek, V.; Plutnar, J.; Loktionova, N.; Riss, P. J.; Rosch, F.; Lukes, I., *Chem. Eur. J.* **2010**, 16, 7174-7185.
43. Simecek, J.; Schulz, M.; Notni, J.; Plutnar, J.; Kubicek, V.; Havlickova, J.; Hermann, P., *Inorg. Chem.* **2012**, 51, 577-590.
44. Arrowsmith, R. L.; Waghorn, P. A.; Jones, M. W.; Bauman, A.; Brayshaw, S. K.; Hu, Z. Y.; Kociok-Kohn, G.; Mindt, T. L.; Tyrrell, R. M.; Botchway, S. W.; Dilworth, J. R.; Pascu, S. I., *Dalton Trans.* **2011**, 40, 6238-6252.
45. Paterson, B. M.; Karas, J. A.; Scanlon, D. B.; White, J. M.; Donnelly, P. S., *Inorg. Chem.* **2010**, 49, 1884-1893.
46. Berry, D. J.; Ma, Y. M.; Ballinger, J. R.; Tavare, R.; Koers, A.; Sunassee, K.; Zhou, T.; Nawaz, S.; Mullen, G. E. D.; Hider, R. C.; Blower, P. J., *Chem. Commun.* **2011**, 47, 7068-7070.
47. Boros, E.; Ferreira, C. L.; Cawthray, J. F.; Price, E. W.; Patrick, B. O.; Wester, D. W.; Adam, M. J.; Orvig, C., *J. Am. Chem. Soc.* **2010**, 132, 15726-15733.
48. Czernin, J.; Allen-Auerbach, M.; Schelbert, H. R., *J. Nucl. Med.* **2007**, 48, 78S-88S.
49. Boone, J. M.; Velazquez, O.; Cherry, S. R., *Mol. Imaging* **2004**, 3, 149-58.
50. Catana, C.; Wu, Y. B.; Judenhofer, M. S.; Qi, J. Y.; Pichler, B. J.; Cherry, S. R., *J. Nucl. Med.* **2006**, 47, 1968-1976.
51. Pichler, B. J.; Judenhofer, M. S.; Catana, C.; Walton, J. H.; Kneilling, M.; Nutt, R. E.; Siegel, S. B.; Claussen, C. D.; Cherry, S. R., *J. Nucl. Med.* **2006**, 47, 639-647.
52. Cherry, S. R., *J. Nucl. Med.* **2006**, 47, 1735-1745.
53. Seemann, M. D., *Technol. Cancer Res. Treat.* **2005**, 4, 577-582.
54. Yang, X. Q.; Hong, H.; Grailer, J. J.; Rowland, I. J.; Javadi, A.; Hurley, S. A.; Xiao, Y. L.; Yang, Y. A.; Zhang, Y.; Nickles, R.; Cai, W. B.; Steeber, D. A.; Gong, S. Q., *Biomaterials* **2011**, 32, 4151-4160.
55. Chouly, C.; Pouliquen, D.; Lucet, I.; Jeune, J. J.; Jallet, P., *J. Microencapsul.* **1996**, 13, 245-255.
56. Nie, S. M.; Xing, Y.; Kim, G. J.; Simons, J. W., Nanotechnology applications in cancer. In *Annu. Rev. Biomed. Eng.*, Palo Alto, 2007; Vol. 9, pp 257-288.
57. Parak, W. J., *Eur. Biophys. J.* **2003**, 32, 176-176.
58. Parak, W. J.; Gerion, D.; Pellegrino, T.; Zanchet, D.; Micheel, C.; Williams, S. C.; Boudreau, R.; Le Gros, M. A.; Larabell, C. A.; Alivisatos, A. P., *Nanotechnology* **2003**, 14, R15-R27.
59. Lu, A.-H.; Salabas, E. L.; Schueth, F., *Angew. Chem. Int. Ed.* **2007**, 46, 1222-1244.
60. Yang, C.; Wu, J.; Hou, Y., *Chem. Commun.* **2011**, 47, 5130-5141.
61. Qiao, R.; Yang, C.; Gao, M., *J. Mater. Chem.* **2009**, 19, 6274-6293.
62. Jun, Y. W.; Huh, Y. M.; Choi, J. S.; Lee, J. H.; Song, H. T.; Kim, S.; Yoon, S.; Kim, K. S.; Shin, J. S.; Suh, J. S.; Cheon, J., *J. Am. Chem. Soc.* **2005**, 127, 5732-5733.
63. Gonzales-Weimuller, M.; Zeisberger, M.; Krishnan, K. M., *J. Magn. Magn. Mater.* **2009**, 321, 1947-1950.
64. Issa, B.; Obaidat, I. M.; Albiss, B. A.; Haik, Y., *Int. J. Mol. Sci.* **2013**, 14, 21266-21305.
65. Massart, R.; Cabuil, V., *J. Chim. Phys. Phys.- Chim. Biol.* **1987**, 84, 967-973.
66. Sun, S. H.; Zeng, H., *J. Am. Chem. Soc.* **2002**, 124, 8204-8205.
67. Cai, W.; Wan, J., *J. Colloid Interface Sci.* **2007**, 305, 366-370.
68. Chin, A. B.; Yaacob, I. I., *J. Mater. Process. Technol.* **2007**, 191, 235-237.
69. Ennas, G.; Musinu, A.; Piccaluga, G.; Zedda, D.; Gatteschi, D.; Sangregorio, C.; Stanger, J. L.; Concas, G.; Spano, G., *Chem. Mater.* **1998**, 10, 495-502.

70. Pascal, C.; Pascal, J. L.; Favier, F.; Moubtassim, M. L. E.; Payen, C., *Chem. Mater.* **1999**, 11, 141-147.
71. Abu Mukh-Qasem, R.; Gedanken, A., *J. Colloid Interface Sci.* **2005**, 284, 489-494.
72. Salazar-Alvarez, G.; Muhammed, M.; Zagorodni, A. A., *Chem. Eng. Sci.* **2006**, 61, 4625-4633.
73. Wang, Z. M.; Liu, Y.; Zeng, X. Y., *Powder Technol.* **2006**, 161, 65-68.
74. Pecharroman, C.; Gonzalezcarreno, T.; Iglesias, J. E., *Phys. Chem. Miner.* **1995**, 22, 21-29.
75. Murray, C. B.; Kagan, C. R.; Bawendi, M. G., *Annu. Rev. Mater. Sci.* **2000**, 30, 545-610.
76. Schladt, T. D.; Schneider, K.; Schild, H.; Tremel, W., *Dalton Trans.* **2011**, 40, 6315-6343.
77. Santra, S.; Tapecc, R.; Theodoropoulou, N.; Dobson, J.; Hebard, A.; Tan, W. H., *Langmuir* **2001**, 17, 2900-2906.
78. Chen, M.; Yamamuro, S.; Farrell, D.; Majetich, S. A., *J. Appl. Phys.* **2003**, 93, 7551-7553.
79. Wagner, S.; Schnorr, J.; Pilgrimm, H.; Hamm, B.; Taupitz, M., *Invest. Radiol.* **2002**, 37, 167-177.
80. Bumb, A.; Brechbiel, M. W.; Choyke, P. L.; Fugger, L.; Eggeman, A.; Prabhakaran, D.; Hutchinson, J.; Dobson, P. J., *Nanotechnology* **2008**, 19, 6.
81. Lim, J. K.; Majetich, S. A.; Tilton, R. D., *Langmuir* **2009**, 25, 13384-13393.
82. Bee, A.; Massart, R.; Neveu, S., *J. Magn. Magn. Mater.* **1995**, 149, 6-9.
83. Fauconnier, N.; Bee, A.; Roger, J.; Pons, J. N., *J. Mol. Liq.* **1999**, 83, 233-242.
84. Bautista, M. C.; Bomati-Miguel, O.; Morales, M. D.; Serna, C. J.; Veintemillas-Verdaguer, S., *J. Magn. Magn. Mater.* **2005**, 293, 20-27.
85. Barrera, C.; Herrera, A. P.; Rinaldi, C., *J. Colloid Interface Sci.* **2009**, 329, 107-113.
86. Petri-Fink, A.; Steitz, B.; Finka, A.; Salaklang, J.; Hofmann, H., *Eur. J. Pharm. Biopharm.* **2008**, 68, 129-137.
87. Lee, H. Y.; Lee, S. H.; Xu, C. J.; Xie, J.; Lee, J. H.; Wu, B.; Koh, A. L.; Wang, X. Y.; Sinclair, R.; Xwang, S.; Nishimura, D. G.; Biswal, S.; Sun, S. H.; Cho, S. H.; Chen, X. Y., *Nanotechnology* **2008**, 19, 6.
88. Welo, L. A.; Baudisch, O., *Science* **1925**, 62, 311-2.
89. Buchi, J.; Zoppi-Hug, R., *Pharm. Acta Helv.* **1956**, 31, 477-contd.
90. Kang, Y. S.; Risbud, S.; Rabolt, J. F.; Stroeve, P., *Chem. Mater.* **1996**, 8, 2209-&.
91. Tartaj, P.; Morales, M. D.; Veintemillas-Verdaguer, S.; Gonzalez-Carreno, T.; Serna, C. J., *J. Phys. D* **2003**, 36, R182-R197.
92. Rockenberger, J.; Scher, E. C.; Alivisatos, A. P., *J. Am. Chem. Soc.* **1999**, 121, 11595-11596.
93. Hyeon, T.; Lee, S. S.; Park, J.; Chung, Y.; Bin Na, H., *J. Am. Chem. Soc.* **2001**, 123, 12798-12801.
94. Hyeon, T., *Chem. Commun.* **2003**, 927-934.
95. Woo, K.; Hong, J.; Choi, S.; Lee, H. W.; Ahn, J. P.; Kim, C. S.; Lee, S. W., *Chem. Mater.* **2004**, 16, 2814-2818.
96. Boal, A. K.; Das, K.; Gray, M.; Rotello, V. M., *Chem. Mater.* **2002**, 14, 2628-2636.
97. Lee, N.; Kim, H.; Choi, S. H.; Park, M.; Kim, D.; Kim, H.-C.; Choi, Y.; Lin, S.; Kim, B. H.; Jung, H. S.; Kim, H.; Park, K. S.; Moon, W. K.; Hyeon, T., *Proc. Natl. Acad. Sci. U. S. A.* **2011**, 108, 2662-2667.
98. Jang, J.-t.; Nah, H.; Lee, J.-H.; Moon, S. H.; Kim, M. G.; Cheon, J., *Angew. Chem. Int. Ed.* **2009**, 48, 1234-1238.
99. Li, Z.; Yi, P. W.; Sun, Q.; Lei, H.; Zhao, H. L.; Zhu, Z. H.; Smith, S. C.; Lan, M. B.; Lu, G. Q., *Adv. Funct. Mater.* **2012**, 22, 2387-2393.
100. Rikken, R. S. M.; Nolte, R. J. M.; Maan, J. C.; van Hest, J. C. M.; Wilson, D. A.; Christianen, P. C. M., *Soft Matter* **2014**, 10, 1295-1308.
101. Wang, W.-W.; Yao, J.-L., *Mater. Lett.* **2010**, 64, 840-842.
102. Lesnikovich, A. I.; Shunkevich, T. M.; Naumenko, V. N.; Vorobyova, S. A.; Baykov, M. V., *J. Magn. Magn. Mater.* **1990**, 85, 14-16.
103. Sun, Y. K.; Duan, L.; Guo, Z. R.; Yun, D. M.; Ma, M.; Xu, L.; Zhang, Y.; Gu, N., *J. Magn. Magn. Mater.* **2005**, 285, 65-70.
104. Philipse, A. P.; Vanbruggen, M. P. B.; Pathmamanoharan, C., *Langmuir* **1994**, 10, 92-99.
105. Lu, Y.; Yin, Y. D.; Mayers, B. T.; Xia, Y. N., *Nano Lett.* **2002**, 2, 183-186.

106. Butterworth, M. D.; Bell, S. A.; Armes, S. P.; Simpson, A. W., *J. Colloid Interface Sci.* **1996**, 183, 91-99.
107. Tartaj, P.; Serna, C. J., *J. Am. Chem. Soc.* **2003**, 125, 15754-15755.
108. Tartaj, P.; Serna, C. J., *Chem. Mater.* **2002**, 14, 4396-4402.
109. Yu, C. H.; Tam, K. Y.; Lo, C. C. H.; Tsang, S. C., *IEEE Trans. Magn.* **2007**, 43, 2436-2438.
110. Jana, N. R.; Earhart, C.; Ying, J. Y., *Chem. Mater.* **2007**, 19, 5074-5082.
111. Barreto, J. A.; Matterna, M.; Graham, B.; Stephan, H.; Spiccia, L., *New J. Chem.* **2011**, 35, 2705-2712.
112. Sun, Y. B.; Ding, X. B.; Zheng, Z. H.; Cheng, X.; Hu, X. H.; Peng, Y. X., *Chem. Commun.* **2006**, 2765-2767.
113. Larsen, E. K. U.; Nielsen, T.; Wittenborn, T.; Birkedal, H.; Vorup-Jensen, T.; Jakobsen, M. H.; Ostergaard, L.; Horsman, M. R.; Besenbacher, F.; Howard, K. A.; Kjems, J., *Acs Nano* **2009**, 3, 1947-1951.
114. Wang, Y.; Xu, C.; Ow, H., *Theranostics* **2013**, 3, 544-560.
115. Cai, W.; Chen, K.; Li, Z.-B.; Gambhir, S. S.; Chen, X., *J. Nucl. Med.* **2007**, 48, 1862-1870.
116. Lee, H.-Y.; Li, Z.; Chen, K.; Hsu, A. R.; Xu, C.; Xie, J.; Sun, S.; Chen, X., *J. Nucl. Med.* **2008**, 49, 1371-1379.
117. Mankoff, D. A., *J. Nucl. Med.* **2007**, 48, 18N-+.
118. Choyke, P. L., *Sci. Transl. Med.* **2014**, 6.
119. Gibson, N.; Holzwarth, U.; Abbas, K.; Simonelli, F.; Kozempel, J.; Cydzik, I.; Cotogno, G.; Bulgheroni, A.; Gilliland, D.; Ponti, J.; Franchini, F.; Marmorato, P.; Stamm, H.; Kreyling, W.; Wenk, A.; Semmler-Behnke, M.; Buono, S.; Maciocco, L.; Burgio, N., *Arch. Toxicol.* **2011**, 85, 751-773.
120. Bartholoma, M. D.; Louie, A. S.; Valliant, J. F.; Zubieta, J., *Chem. Rev.* **2010**, 110, 2903-2920.
121. Ma, R.; Welch, M. J.; Reibenspies, J.; Martell, A. E., *Inorg. Chim. Acta* **1995**, 236, 75-82.
122. Clarke, E. T.; Martell, A. E., *Inorg. Chim. Acta* **1991**, 190, 37-46.
123. Heppeler, A.; Froidevaux, S.; Macke, H. R.; Jermann, E.; Behe, M.; Powell, P.; Hennig, M., *Chem. Eur. J.* **1999**, 5, 1974-1981.
124. Al-Nahhas, A.; Win, Z.; Szyszko, T.; Singh, A.; Nanni, C.; Fanti, S.; Rubello, D., *Anticancer Research* **2007**, 27, 4087-4094.
125. Andre, J. P.; Macke, H.; Kaspar, A.; Kunnecke, B.; Zehnder, M.; Macko, L., *J. Inorg. Biochem.* **2002**, 88, 1-6.
126. Jarrett, B. R.; Gustafsson, B.; Kukis, D. L.; Louie, A. Y., *Bioconjugate Chem.* **2008**, 19, 1496-1504.
127. Tu, C. Q.; Ma, X. C.; House, A.; Kauzlarich, S. M.; Louie, A. Y., *ACS Med. Chem. Lett.* **2011**, 2, 285-288.
128. Stelter, L.; Pinkernelle, J. G.; Michel, R.; Schwartlander, R.; Raschzok, N.; Morgul, M. H.; Koch, M.; Denecke, T.; Ruf, J.; Baumler, H.; Jordan, A.; Hamm, B.; Sauer, I. M.; Teichgraber, U., *Mol. Imaging Biol.* **2010**, 12, 25-34.
129. Nikolic, M. S.; Krack, M.; Aleksandrovic, V.; Kornowski, A.; Forster, S.; Weller, H., *Angew. Chem. Int. Ed.* **2006**, 45, 6577-6580.
130. Longmire, M.; Choyke, P. L.; Kobayashi, H., *Nanomedicine* **2008**, 3, 703-717.
131. Stasiuk, G. J.; Smith, H.; Wylezinska-Arridge, M.; Tremoleda, J. L.; Trigg, W.; Luthra, S. K.; Iveson, V. M.; Gavins, F. N. E.; Long, N. J., *Chem. Commun.* **2013**, 49, 564-566.
132. Kallay, N.; Zalac, S., *J. Colloid Interface Sci.* **2002**, 253, 70-76.
133. Min, Y. J.; Akbulut, M.; Kristiansen, K.; Golan, Y.; Israelachvili, J., *Nature Materials* **2008**, 7, 527-538.
134. Miles, W. C.; Goff, J. D.; Huffstetler, P. P.; Reinholz, C. M.; Pothayee, N.; Caba, B. L.; Boyd, J. S.; Davis, R. A.; Riffle, J. S., *Langmuir* **2009**, 25, 803-813.
135. Eberbeck, D.; Wieckhorst, F.; Steinhoff, U.; Trahms, L., *J. Phys. Cond. Matt.* **2006**, 18, S2829-S2846.
136. Zhang, Y.; Kohler, N.; Zhang, M. Q., *Biomaterials* **2002**, 23, 1553-1561.
137. Colombo, M.; Carregal-Romero, S.; Casula, M. F.; Gutierrez, L.; Morales, M. P.; Bohm, I. B.; Heverhagen, J. T.; Prospero, D.; Parak, W. J., *Chem. Soc. Rev.* **2012**, 41, 4306-4334.

138. Bouziotis, P.; Psimadas, D.; Tsotakos, T.; Stamopoulos, D.; Tsoukalas, C., *Curr. Topics Med. Chem.* **2012**, 12, 2694-2702.
139. Nikam, D. S.; Jadhav, S. V.; Khot, V. M.; Ningthoujam, R. S.; Hong, C. K.; Mali, S. S.; Pawar, S. H., *RSC Advances* **2014**, 4, 12662-12671.
140. Molina-Bolivar, J. A.; Ortega-Vinuesa, J. L., *Langmuir* **1999**, 15, 2644-2653.
141. Zhang, Y.; Chen, Y. S.; Westerhoff, P.; Hristovski, K.; Crittenden, J. C., *Water Res.* **2008**, 42, 2204-2212.
142. Lozsán, A.; Garcia-Sucre, M.; Urbina-Villalba, G., *Physical Review E* **2005**, 72, 13.
143. Kalow, J. A.; Doyle, A. G., *J. Am. Chem. Soc.* **2011**, 133, 16001-16012.
144. Surendra, K.; Krishnaveni, N. S.; Nageswar, Y. V. D.; Rao, K. R., *Synth. Commun.* **2005**, 35, 2195-2201.
145. Hong, S.; Rhee, I.; Chang, Y. M., *Journal of the Korean Physical Society* **2007**, 51, 1453-1456.
146. Ye, F.; Laurent, S.; Fornara, A.; Astolfi, L.; Qin, J.; Roch, A.; Martini, A.; Toprak, M. S.; Muller, R. N.; Muhammed, M., *Contrast Media Mol. Imaging* **2012**, 7, 460-468.
147. Ahmad, T.; Bae, H.; Rhee, I.; Chang, Y.; Lee, J.; Hong, S., *Current Applied Physics* **2012**, 12, 969-974.
148. Wang, C. G.; Chen, J.; Talavage, T.; Irudayaraj, J., *Angew. Chem. Int. Ed.* **2009**, 48, 2759-2763.
149. LaConte, L. E. W.; Nitin, N.; Zurkiya, O.; Caruntu, D.; O'Connor, C. J.; Hu, X. P.; Bao, G., *J. Magn. Reson. Imaging* **2007**, 26, 1634-1641.
150. Wang, Y. X. J.; Hussain, S. M.; Krestin, G. P., *Eur. Radiol.* **2001**, 11, 2319-2331.
151. Mohapatra, J.; Mitra, A.; Tyagi, H.; Bahadur, D.; Aslam, M., *Nanoscale* **2015**, 7, 9174-9184.
152. Choi, H. S.; Liu, W.; Misra, P.; Tanaka, E.; Zimmer, J. P.; Ipe, B. I.; Bawendi, M. G.; Frangioni, J. V., *Nat. Biotechnol.* **2007**, 25, 1165-1170.
153. Ehrhardt, G. J.; Welch, M. J., *J. Nucl. Med.* **1978**, 19, 925-929.
154. Harris, W. R.; Pecoraro, V. L., *Biochemistry* **1983**, 22, 292-299.
155. de Rosales, R. T. M.; Tavaré, R.; Paul, R. L.; Jauregui-Osoro, M.; Protti, A.; Galaria, A.; Varma, G.; Szanda, I.; Blower, P. J., *Angew. Chem. Int. Ed.* **2011**, 50, 5509-5513.
156. de Rosales, R. T. M.; Tavaré, R.; Galaria, A.; Varma, G.; Protti, A.; Blower, P. J., *Bioconjugate Chem.* **2011**, 22, 455-465.
157. Qiao, R. R.; Yang, C. H.; Gao, M. Y., *J. Mater. Chem.* **2009**, 19, 6274-6293.
158. Locatelli, E.; Gil, L.; Israel, L. L.; Passoni, L.; Naddaka, M.; Pucci, A.; Reese, T.; Gomez-Vallejo, V.; Milani, P.; Matteoli, M.; Llop, J.; Lellouche, J. P.; Franchini, M. C., *International Journal of Nanomedicine* **2012**, 7, 6021-6033.
159. Welch, M. J.; Hawker, C. J.; Wooley, K. L., *J. Nucl. Med.* **2009**, 50, 1743-1746.
160. Elsabahy, M.; Wooley, K. L., *Chem. Soc. Rev.* **2012**, 41, 2545-2561.
161. Jokerst, J. V.; Gambhir, S. S., *Acc. Chem. Res.* **2011**, 44, 1050-1060.
162. Torres Martin de Rosales, R.; Tavaré, R.; Paul, R. L.; Jauregui-Osoro, M.; Protti, A.; Galaria, A.; Varma, G.; Szanda, I.; Blower, P. J., *Angew. Chem. Int. Ed.* **2011**, 50, 5509-13.
163. Tonik, S. E.; Shindelman, J. E.; Sussman, H. H., *Breast Cancer Res. Treat.* **1986**, 7, 71-76.
164. Choi, H.; Choi, S. R.; Zhou, R.; Kung, H. F.; Chen, I. W., *Acad. Radiol.* **2004**, 11, 996-1004.
165. Kiessling, F.; Heilmann, M.; Vosseler, S.; Lichy, M.; Krix, M.; Fink, C.; Kiessling, I.; Steinbauer, H.; Schad, L.; Fusenig, N. E.; Delorme, S., *Int. J. Cancer* **2003**, 104, 113-120.
166. Broxmeyer, H. E., *Curr. Opin. Hematol.* **2008**, 15, 49-58.
167. Horuk, R., *Cytokine Growth Factor Rev.* **2001**, 12, 313-335.
168. Baggiolini, M.; Dewald, B.; Moser, B., *Annu. Rev. Immunol.* **1997**, 15, 675-705.
169. Abroun, S., *Yakhteh* **2008**, 10, 155-166.
170. Holgate, S. T., *Clin. Exp. Allergy* **2008**, 38, 872-897.
171. Luker, K. E.; Luker, G. D., *Cancer Lett.* **2006**, 238, 30-41.
172. Burger, J. A.; Kipps, T. J., *Blood* **2006**, 107, 1761-1767.
173. Odendaal, A. Y.; Fiamengo, A. L.; Ferdani, R.; Wadas, T. J.; Hill, D. C.; Peng, Y. J.; Heroux, K. J.; Golen, J. A.; Rheingold, A. L.; Anderson, C. J.; Weisman, G. R.; Wongs, E. H., *Inorg. Chem.* **2011**, 50, 3078-3086.

174. Este, J. A.; Cabrera, C.; De Clercq, E.; Struyf, S.; Van Damme, J.; Bridger, G.; Skerlj, R. T.; Abrams, M. J.; Henson, G.; Gutierrez, A.; Clotet, B.; Schols, D., *Mol. Pharmacol.* **1999**, *55*, 67-73.
175. Liang, X. Y.; Sadler, P. J., *Chem. Soc. Rev.* **2004**, *33*, 246-266.
176. Barefield, E. K.; Wagner, F.; Hodges, K. D., *Inorg. Chem.* **1976**, *15*, 1370-1377.
177. Kolinski, R. A., *Pol. J. Chem.* **1995**, *69*, 1039-1045.
178. Le Baccon, M.; Chuburu, F.; Toupet, L.; Handel, H.; Soibinet, M.; Dechamps-Olivier, I.; Barbieri, J. P.; Aplincourt, M., *New J. Chem.* **2001**, *25*, 1168-1174.
179. Wong, E. H.; Weisman, G. R.; Hill, D. C.; Reed, D. P.; Rogers, M. E.; Condon, J. S.; Fagan, M. A.; Calabrese, J. C.; Lam, K. C.; Guzei, I. A.; Rheingold, A. L., *J. Am. Chem. Soc.* **2000**, *122*, 10561-10572.